UNIVERSITI TEKNOLOGI MARA

INTEGRATED MACHINE LEARNING AND 3D RESERVOIR MODELLING FOR CO_2 ADSORPTION CAPACITY PREDICTION BASED ON MINERALOGICAL COMPOSITION

MUQRI SYAHMI BIN ANAS

MSc

July 2026

UNIVERSITI TEKNOLOGI MARA

INTEGRATED MACHINE LEARNING AND 3D RESERVOIR MODELLING FOR CO_2 ADSORPTION CAPACITY PREDICTION BASED ON MINERALOGICAL COMPOSITION

MUQRI SYAHMI BIN ANAS

Thesis submitted in fullfillment
of the requirements for the degree of
Master of Science
(Chemical Engineering)

Faculty of Chemical Engineering

July 2026

CONFIRMATION BY PANEL OF EXAMINERS

I certify that a Panel of Examiners has met on 7th May 2026 to conduct the final examination of Muqri Syahmi bin Anas on his Master of Science thesis entitled "Integrated Machine Learning and 3D Reservoir Modelling for CO_2 Adsorption Capacity Prediction Based on Mineralogical Composition" in accordance with Universiti Teknologi MARA Act 1976 (Akta 173). The Panel of Examiner recommends that the student be awarded the relevant degree. The Panel of Examiners was as follows:

Nik Raikhan Nik Him, PhD
Associate Professor
Faculty of Chemical Engineering
Universiti Teknologi MARA
(Chairman)

Nurul Aimi Ghazali, PhD
Senior Lecturer
Faculty of Chemical Engineering
Universiti Teknologi MARA
(Internal Examiner)

Mohd Akhmal Muhamad Sidek, Phd
Associate Professor
Faculty of Chemical and Energy Engineering
University Teknologi Malaysia
(External Examiner)

PROF DR HJH ZURAEDA IBRAHIM
Dean
Institute of Postgraduates Studies
Universiti Teknologi MARA

Date: 9 July 2026

AUTHOR'S DECLARATION

I declare that the work in this dissertation was carried out in accordance with the regulations of Universiti Teknologi MARA. It is original and is the results of my own work, unless otherwise indicated or acknowledged as referenced work. This thesis has not been submitted to any other academic institution or non-academic institution for any degree or qualification.

I, hereby, acknowledge that I have been supplied with the Academic Rules and Regulations for Postgraduate, Universiti Teknologi MARA, regulating the conduct of my study and research.

Name of Student	:	Muqri Syahmi bin Anas
Student I.D No.	:	2024577831
Programme	:	Master of Science (Chemical Engineering)
Faculty	:	Chemical Engineering
Dissertation Title	:	Development of a 3D Reservoir Model for Adsorption Capacity on Different Minerals
Signature of Student	:	…….
Date	:	July 2026

ABSTRACT

Over the last five decades, carbon capture and storage (CCS) has been a popular technology to mitigate carbon emissions. The most critical component for early-stage exploration in CCS applications is identifying, assessing, and selecting suitable sites to capture, transport, and store CO_2. The CO_2 storage mechanism, adsorption, has gained a lot of attention in CO_2 storage capacity estimation. The CO_2 molecules generated from the industrial activities are transported to geological storage sites, where it migrates, adsorb onto mineral surfaces, react geochemically, and are stored permanently within the solid mineral surface. Common minerals, such as kaolinite, montmorillonite, illite, and chlorite, exhibit a unique physicochemical structure that offers distinct adsorption capacities. Despite these mineral-specific interactions, conventional CO_2 storage capacity estimation methods primarily rely on bulk reservoir properties, such as porosity and permeability, thereby neglecting mineralogical controls on adsorption. In response to this limitation, this research aimed to characterise and utilise mineralogical composition information to estimate the CO_2 adsorption capacity. For a petrophysicist, the main challenge lies in the limited well log data available, such as the spectral gamma ray log (SGR) and photoelectric factor (PEF). To address this constraint, the proposed methodology framework intends to apply an advanced machine learning (ML) technique, which is the Extreme Gradient Boosting technique (XGBoost), to develop a mineralogy predictive model using the conventional well logs, including bulk density (RHOB), neutron-porosity (NPHI), and compressional slowness (DTC) logs. The prediction results indicate that the XGBoost-trained model achieves the RMSE, MAE, and R_2 score of 0.009,0.021, and 0.884, respectively, on the blind dataset. Notably, the study found that increasing the number of input logs does not necessarily improve accuracy, suggesting that optimized three-log inputs provide a more efficient predictive framework than traditional six-log methods. Analysis of the X Field reveals a lithology dominated by clay minerals (65.29%), particularly illite (59.80%), which was found to have a significantly higher CO_2 adsorption potential and stronger reactivity compared to quartz and carbonate minerals. A critical finding of this work is that neglecting mineral-specific interactions can lead to a significant underestimation of the reactive surface area and total CO_2 storage capacity. Furthermore, 3D static modeling and simulations show that while CO_2 adsorption increases with pressure and temperature under supercritical conditions, the rate of increase diminishes at higher pressures. By integrating mineral-specific adsorption data into a 3D reservoir framework, this approach provides a more accurate assessment of spatial heterogeneity, identifies favorable storage zones, and reduces the risks of overpressure and leakage compared to standard estimation methods. These findings underscore the necessity of mineral-based modeling to enhance long-term storage security and trapping efficiency in geological reservoirs.

ACKNOWLEDGEMENTS

Alhamdulillah, all praises to Allah for giving me the strength and blessings to complete the thesis. I am grateful for this unforgettable journey that has given me the experience of the beauty of learning and sharing in conducting research.

I owe my deepest gratitude to my supervisor, Dr Wan Zairani binti Wan Bakar, who has supported, guided, encouraged and moulded me to be a better student and a better person. I want to thank you for encouraging my research. I would also like to thank my co-supervisors, Dr Azlinda bin Azizi and Madam Nur Shuhada Japperi, for their guidance and support in helping me become a successful student.

A special thanks to my family for their constant moral support and prayers during the difficult moments. I would also like to thank all of my friends who supported me with their encouragement to strive towards my goal. To those who indirectly contributed to this research, I really appreciate it. Thank you so much.

TABLE OF CONTENTS

LIST OF TABLES

LIST OF FIGURES

LIST OF ABBREVIATION

Abbreviations

CCS	Carbon Capture and Storage
R2	Coefficient of Determination
DTC	Compressional Sonic Log
RHOB	Density Log
D-A	Dubinin-Astakhov
D-R	Dubinin-Radushkecivh
XGBoost	Extreme Gradient Boosting
FTIR	Fourier Transform Infrared Spectroscopy
GR	Gamma Ray Log
GRFS	Gaussian Random Function Simulation
GBDT	Gradient Boosting Decision Tree
IQR	Interquartile Range
ML	Machine Learning
MAE	Mean Absolute Error
MSE	Mean Squared Error
NPHI	Neutron Porosity Log
PEF	Photoelectric Log
RMSE	Root Mean Squared Error
SGS	Sequential Gaussian Simulation
SSA	Specific Surface Area
TGS	Truncated Gaussian Simulation
XRD	X-ray Diffraction

CHAPTER 1
INTRODUCTION

1.1 Research Background

The extensive combustion of hydrocarbon fuels has led to elevated emissions of greenhouse gases, particularly carbon dioxide, which in turn has intensified the severity of climate change. Carbon capture and storage (CCS) is recognised as a cost-effective and technologically viable long-term mitigation pathway, owing to its capacity to significantly reduce anthropogenic CO_2 emissions (Kazemifar, 2022; Saxena et al., 2024). The process entails three primary stages: capture, transport and geological sequestration. Among these stages, the assessment of storage capacity and integrity remains the most technically challenging aspect of CCS implementation. Such assessments are critical to ensuring the secure, long-term containment of CO_2 within geological formations, thereby minimising the risk of leakage (Mortezaei et al., 2021).

Several geological storage options have been scrutinised, with project economics serving as a critical element in identifying the most feasible solution. Deep saline aquifers and depleted hydrocarbon reservoirs are among the most widely reviewed. Depleted reservoirs, in particular, offer distinct advantages, including well-documented subsurface data and pre-existing infrastructure, which collectively reduce capital expenditure (CapEx) and shorten project timelines.

Long-term storage of CO_2 in geological formations is governed by multiple trapping mechanisms, including structural trapping (Y. Wang et al., 2022), residual trapping (Baban et al., 2023), solubility trapping (Punnam et al., 2022), mineral trapping (Zhang et al., 2024), and adsorption trapping (Jia et al., 2024). Mineral and adsorption trapping are the interactions of CO_2 and solid minerals, which depend on temperature, pressure, and salinity of the brine. The geochemical interactions, which result in the formation of stable carbonate minerals, offer a permanent form of CO_2 immobilisation in the subsurface.

The mineralogical composition of the possible storage locations is very diverse and comprises actinolite, amphibole, biotite, garnet, quartz, pyrite, muscovite, phengite, olivine, plagioclase, and pyroxene. These minerals occur across different geological settings, such as magmatic (C. Chen et al., 2024), sedimentary (X. Yang, Yin, et al.,

2024), hydrothermal (X. Liu et al., 2025), and metamorphic systems (UZUN et al., 2024). Additionally, the development of advanced argillaceous minerals, such as alunite, kaolinite, dickite, pyrophyllite and diaspore, is usually done through alteration processes which include vapour condensation, boiling of hydrothermal fluids, and supergene weathering (Hedenquist & Arribas, 2022). Over geological timescales, natural interactions within these environments have revolutionised mineral distributions and properties, thereby influencing their suitability for CO_2 storage (Medina-Rodriguez et al., 2021).

In this regard, the current study suggests a new strategy to increase CO_2 storage capacity and, at the same time, minimise project costs and time. In particular, it highlights the significance of taking into account the behaviour of CO_2 adsorption with respect to mineralogical characteristics to enhance storage measurements. Moreover, the research offers a three-dimensional (3D) visualisation of the important properties, thus enabling better-informed decision-making in the site selection of CO_2 storage. Ultimately, this research is part of the global strategy in reducing carbon emissions and promoting sustainable development objectives by innovating the CCS applications.

1.2 Problem Statement

Conducting on-site CO_2 storage assessments requires significant time and financial resources, since each location demands expert evaluation due to its distinct geological formations, site-specific engineering considerations, and associated risk factors. Such assessments should be an integral element of the core processes, such as site selection, site characterisation, storage capacity estimation, injection and flow simulation, monitoring, and remediation if necessary. The characterisation of geological and reservoir properties primarily relies on well log and seismic data, whereas X-ray diffraction (XRD) analysis provides higher accuracy for direct measurement of mineralogy (D. Kim et al., 2020). However, XRD acquisition is costly (Ali et al., 2022) and is not always accessible in depleted fields (Raza et al., 2017). The initial high investment, such as, physical core or cutting samples, specialised laboratory equipment, and expert interpretation, have encouraged researchers to develop alternative approaches that utilise readily available data. Consequently, the industry often relies solely on well log data, which is then used to infer the mineralogical composition of the formation (Yan et al., 2021).

Among the various mechanisms involved, adsorption plays a particularly crucial role in CO_2 trapping, as it enables CO_2 molecules to adhere to the mineral surfaces within the reservoir. Based on the adsorption isotherm coefficient, the adsorption capacity is fundamentally governed by the mineralogical properties of the formation, which dictate the degree to which CO_2 can be trapped and immobilised (Zardari & Mohshim, 2025). Understanding these interactions is therefore essential for accurately evaluating storage performance. Despite its importance, current assessment methods often underestimate or neglect the influence of mineralogical composition on CO_2 adsorption capacity (Kumari et al., 2024). Such oversight can lead to uncertainties in estimating storage capacity, predicting CO_2 migration behaviour, and conducting associated risk evaluations (J. Wang, Samara, et al., 2025). To address this limitation, a comprehensive investigation of the initial geological setting is essential to improve the reliability and accuracy of long-term CO_2 storage assessments.

To improve the accuracy and efficiency of CO_2 storage evaluation, recent research trends highlight the integration of machine learning (ML) techniques into storage assessment workflows. By combining well log and X-ray diffraction (XRD) data, ML algorithms can be trained to recognise patterns and predict mineral compositions with high precision. Previous studies have demonstrated that ML-based models can reliably estimate mineralogical properties from well log data, yielding results that closely align with those obtained from XRD analyses (T. Kumar et al., 2022; Rangel Gavidia et al., 2023). Nevertheless, further refinement is needed to adapt these models for data-limited environments, particularly in cases where core or XRD datasets are sparse.

Numerous three-dimensional (3D) reservoir models have been developed to support the evaluation of CO_2 storage potential, with most focusing on bulk reservoir properties such as porosity and permeability (H. Feng et al., 2025; Mahdi & Farman, 2023; Proietti et al., 2022). Despite their utility in site selection, these models inadequately represent CO_2 storage capacity from a geophysical perspective. It is noteworthy that more than 90% of the permanent CO_2 storage potential is attributed to adsorption processes (S. Han et al., 2023). However, most existing studies have not successfully simulated or visualised adsorption capacity due to methodological limitations. This study aims to bridge that gap through 3D modelling of adsorption processes, providing a more robust framework for evaluating storage performance and ensuring long-term sequestration reliability.

1.3 Research Questions

Based on the problem statement that has been identified, the following research questions will be addressed:

i. What alternative methods can be employed to determine mineral composition where well log data are limited, and core data are unavailable?
ii. Was the ML model able to accurately predict the mineral composition from the conventional well logs?
iii. How does the mineralogical composition affect the CO_2 adsorption capacity?
iv. What is the impact of mineral-specific CO_2 adsorption capacities on the performance of geological CO_2 storage?

1.4 Research Objectives

This research aims to construct a three-dimensional (3D) reservoir adsorption capacity model for the depleted oil and gas reservoir. To achieve this goal, the objectives of this research are:

i. To develop a machine learning model for predicting mineralogical composition logs from conventional well log data.
ii. To develop a 3D geological reservoir model that integrating the spatial distribution of predicted minerals relevant to carbon adsorption capacity.
iii. To simulate and evaluate the impact of mineral-specific carbon adsorption capacities on CO_2 storage performance within the 3D model under varying pressure and temperature conditions.

1.5 Scope and Limitations of the Research

The datasets utilised in this study were derived from open-source lithological analysis data comprising well log measurements from selected locations within the South and North Viking Graben and the Malay Basin. Consequently, the predictive performance of the developed model may vary under different geological conditions and should be interpreted within the context of basin-specific characteristics.

This study is limited to the interpretation of mineralogical composition based on selected conventional well logs and does not incorporate advanced logging tools, core-

scale laboratory measurements, or seismic data. Therefore, the interpretation of the mineralogical composition with respect to CO_2 adsorption capacity was conducted using conventional well logs, including bulk density (RHOB), neutron–density (NPHI), and compressional sonic (DTC) logs. The mineralogical composition study focused on key mineral groups, namely quartz, carbonates, and clay minerals such as kaolinite, montmorillonite, illite, and chlorite. The mineral composition was quantified using the standard mathematical formulation developed by Schlumberger (1989), which is also implemented in the mineral solver module of the Techlog software.

In developing the machine learning (ML) model for predicting mineralogical composition, Python programming was employed to perform data processing, analysis, training, and testing. The Extreme Gradient Boosting (XGBoost) algorithm was selected due to its effectiveness in handling large and complex well log datasets and its strong capability to capture non-linear relationships.

Ultimately, a three-dimensional (3D) static reservoir model was constructed by integrating structural, mineralogical, and CO_2 adsorption capacity models using Petrel software. For CO_2 adsorption capacity estimation, the Dubinin–Astakhov (D-A) isotherm model was selected due to its superior capability in representing adsorption behaviour under the current reservoir conditions. This integrated model enabled the evaluation of the relationship between mineralogical variability and CO_2 adsorption capacity. The simulations were then conducted at pressures of 10, 15, and 20 MPa and temperatures of 303.15, 353.15, and 393.15 K, respectively, to evaluate the influence on CO_2 storage performance under varying pressure and temperature conditions.

However, several limitations and assumptions were considered in this study. The reservoir properties such as porosity and permeability, were not explicitly incorporated into the simulation framework. These parameters directly influence the available storage volume and the ability of CO_2 to migrate through interconnected pore networks.

The subsequent parameter that was not considered in the simulation framework is CO_2 injection flow rate. The CO_2 injection flow rate is a critical operational parameter that affects pressure distribution and storage performance within the reservoir. A low injection rate may result in inefficient utilisation of the available storage capacity and prolonged injection periods, whereas an excessively high injection rate may cause rapid pressure build-up around the injection zone, potentially reducing injectivity and increasing the risk of caprock integrity issues or fracture initiation.

As a result, the exclusion of porosity, permeability, and dynamic flow-related parameters limits the ability of the developed model to fully represent reservoir-scale CO_2 transport, pressure evolution, and operational injection behaviour. The findings of this study should therefore be interpreted within the context of static reservoir characterisation and adsorption-based storage assessment rather than comprehensive dynamic reservoir simulation.

1.6 Significance of the Research

This study presents a novel approach for evaluating the influence of mineralogical variability on CO_2 adsorption capacity through the development of an integrated three-dimensional (3D) reservoir model. The workflow incorporates machine learning (ML)-based mineral prediction, adsorption isotherm modelling, and reservoir characterisation to provide a comprehensive assessment of adsorption-based CO_2 storage potential. By complementing conventional laboratory and petrophysical interpretation methods, the proposed approach facilitates a more efficient identification of favourable storage zones for carbon capture and storage (CCS) applications.

Currently, Extreme Gradient Boosting (XGBoost) has attracted considerable attention due to its superior predictive performance compared with many conventional machine learning (ML) algorithms, particularly in modelling complex non-linear relationships and handling high-dimensional structured datasets effectively. Previous studies have demonstrated the strong potential of XGBoost for advanced mineralogical identification using well-log, X-ray diffraction (XRD), and geochemical datasets. However, most existing studies primarily focus on mineral identification and classification, with limited emphasis on linking mineralogical variability to CO_2 adsorption capacity and storage performance. Furthermore, the spatial distribution of adsorption capacity within a reservoir is rarely evaluated using an integrated modelling framework.

To address this gap, this research extends the application of XGBoost by simultaneously predicting multiple minerals, including quartz, calcite, dolomite, kaolinite, montmorillonite, illite, and chlorite, and subsequently integrating the results into a 3D reservoir model. The predicted mineralogical composition is combined with adsorption isotherm modelling to estimate CO_2 adsorption capacity throughout the reservoir. This enables the visualisation and quantification of adsorption potential at the

grid-cell scale, thereby providing a more detailed understanding of how mineralogical heterogeneity influences CO_2 storage behaviour.

The significance of this study lies in its ability to bridge the gap between mineral prediction and CO_2 storage assessment. Unlike conventional approaches that provide only localised or laboratory-scale adsorption measurements, the proposed workflow offers a reservoir-scale representation of adsorption capacity distribution. The resulting model can serve as a preliminary screening tool for identifying favourable CO_2 storage locations, optimising storage capacity estimation, and supporting risk-informed decision-making for future CCS projects. Ultimately, the study contributes to the advancement of data-driven reservoir characterisation and demonstrates the potential of integrating machine learning with reservoir modelling for geological CO_2 sequestration applications.

CHAPTER 2
LITERATURE REVIEW

2.1 Carbon Capture and Storage (CCS) Principle

Carbon dioxide (CO_2) and other greenhouse gases are the primary causes of climate change and global warming. Atmospheric CO_2 levels have been increasing drastically over the past several centuries, reaching about 420 ppm in 2023, and the levels are expected to keep rising annually (Boetcher et al., 2023). This increase has been largely caused by the burning of fossil fuels in major industries like electricity production, industrial production, and transportation. Carbon capture and storage (CCS) has, in turn, become one of the most popular technologies in the last 50 years to counteract CO_2 emissions. The international community is actively pursuing efforts to reduce global emissions to approximately 32,864 Mt by 2100 (Long et al., 2023), which contribute to the sustainable environmental management.

To establish the foundation of this study, it is essential to understand the fundamental principles of carbon capture and storage (CCS). The primary processes involved are illustrated in Figure 2.1 and they are capturing, compressing, transporting, and injecting CO_2 into secure geological formations. In the first stage, the CO_2 emissions produced from the combustion of fossil fuels are captured directly at their source. The gas is then subjected to high-pressure conditions, compressing it into a supercritical fluid state. The resulting compressed CO_2 is then transported, either through pipelines or special cargo ships, to the storage site.

In the final phase, the gas is injected into deep underground reservoirs for permanent storage, with stringent monitoring and safety measures implemented to prevent any leakage into the atmosphere. There are also other possible CO_2 reduction pathways, such as ocean injection, ex-situ mineralisation in manufactured products, and ex-situ use in enhanced oil or gas recovery (EOR/EGR) (Nwali et al., 2024). Among the available options, geological storage is the most widely adopted, as it offers long-term effectiveness in mitigating environmental risks.

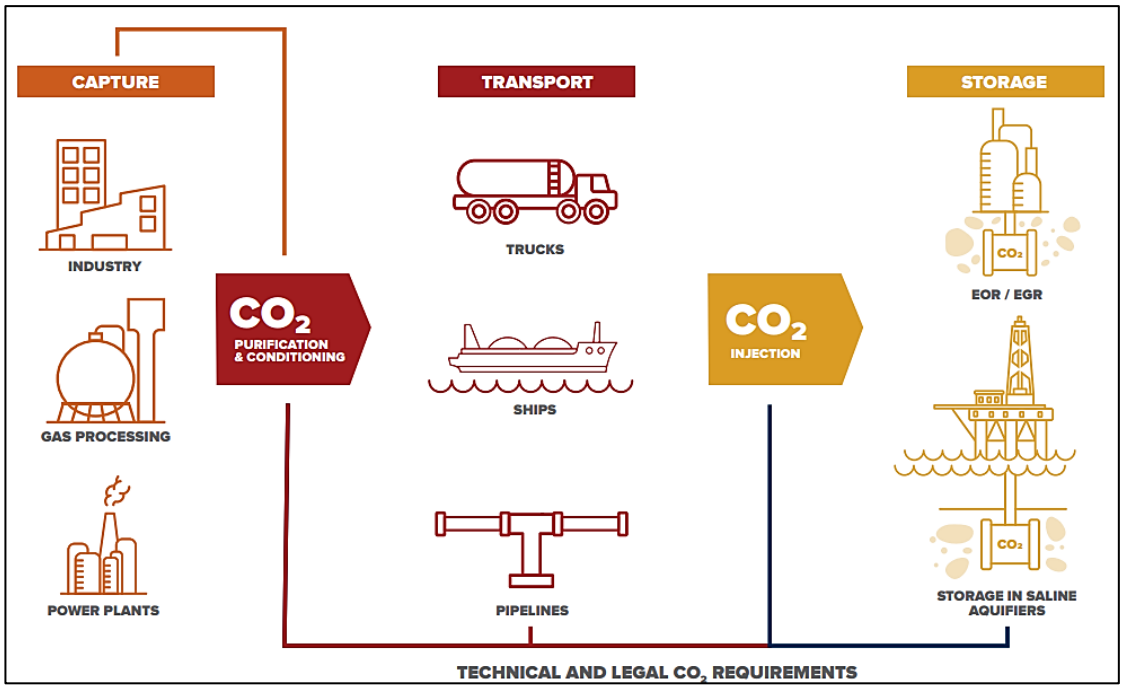

Figure 2.1 Carbon Capture and Storage - A Conceptual Diagram

Source : Kearns et al. (2021)

2.2 Geological Storage for CO_2

2.2.1 Fundamentals of the Geological Storage

CO_2 storage technologies have been in the development phase over the last few decades, and the current progress is focused on maximising the storage capacity, enhancing long-term security, and reducing environmental risks (Andrew Emuobosa Esiri et al., 2024). Recent technologies were developed to effectively trap CO_2 and then inject it permanently into the geological formations. Appropriate geological formations are required to fit certain criteria: they must be found below 850 metres and be covered by one or more layers of impermeable caprock to avoid upwards migration (Newell & Ilgen, 2019). Moreover, the formations must be highly porous and permeable to facilitate substantial amounts of CO_2 (Y. Feng et al., 2023).

Geological storage can be implemented across various subsurface environments, including deep saline aquifers, coal seams, unconventional reservoirs, and depleted hydrocarbon reservoirs, as illustrated in Figure 2.2 (C. Cao et al., 2020). Among these options, deep saline aquifers have the highest storage capacity (A. Luo et al., 2022). The highly recommended storage options are also found in depleted reservoirs because of large pore volumes, long-term hydrocarbon retention, availability of existing

infrastructure, and well-characterised subsurface conditions. Additionally, CO_2 injection in these reservoirs has other advantages in terms of increasing the recovery of the remaining natural gas (Z. Chen, 2025; Hamza, Hussein, Al-Marri, Mahmoud, Shawabkeh, et al., 2021). These benefits render mature onshore fields especially appealing in the deployment of CCS since they permit the re-use of the wells and facilities. However, the threat of CO_2 leakage still exists, especially in situations where the infrastructure is worn out or geological conditions are undermined.

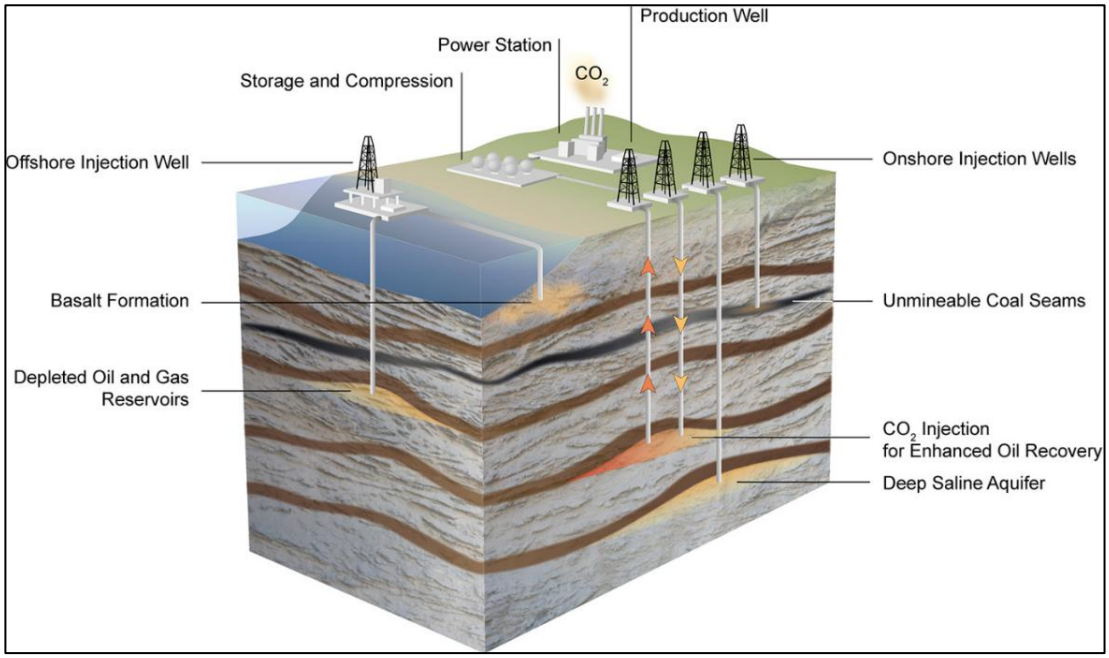

Figure 2.2 A 3D Diagram of CO_2 Geological Storage Location.

Source : Ali et al. (2022)

2.2.2 CO_2 Storage in Depleted Reservoir

Previous studies on CO_2 geological storage have primarily focused on developing methods that are efficient, reliable, and economically viable. Among these options, depleted reservoirs have received considerable attention due to their cost-effectiveness and relatively low implementation risk (Harati et al., 2024). A depleted reservoir is an underground geological formation that was previously exploited for oil or gas production, from which nearly all hydrocarbons have already been extracted. These formations are normally covered by non-permeable caprock systems which had entrap hydrocarbons over millions of years through structural mechanisms, hence

providing good conditions to store CO_2 over a long period of time. Figure 2.3 shows the mechanism of CO_2 storage in depleted reservoirs.

There are various benefits of depleted reservoirs to CCS. They will tend to offer sufficient storage capacity, well-defined reservoir characteristics (including rock type, porosity and permeability), and demonstrated caprock integrity. Furthermore, they have an underground geology, fault systems, and already developed industrial infrastructure that can be repurposed to inject CO_2 (Bashir et al., 2024; Paluszny et al., 2020). Their hydrocarbon storage history shows long-term stability and increases the safety of CO_2 storage. In addition, the presence of historical field and production data eases the process of assessing the performance of the reservoirs to store CO_2.

However, several challenges remain. The long-term stability of storage sites can be compromised by geochemical and geomechanical processes such as mineral reactions, reservoir compaction, and formation expansion (Hamza, Hussein, Al-Marri, Mahmoud, Shawabkeh, et al., 2021). Leakage is still a major issue of concern, and this requires constant monitoring and risk evaluation as a way of maintaining the integrity of storage and the environment.

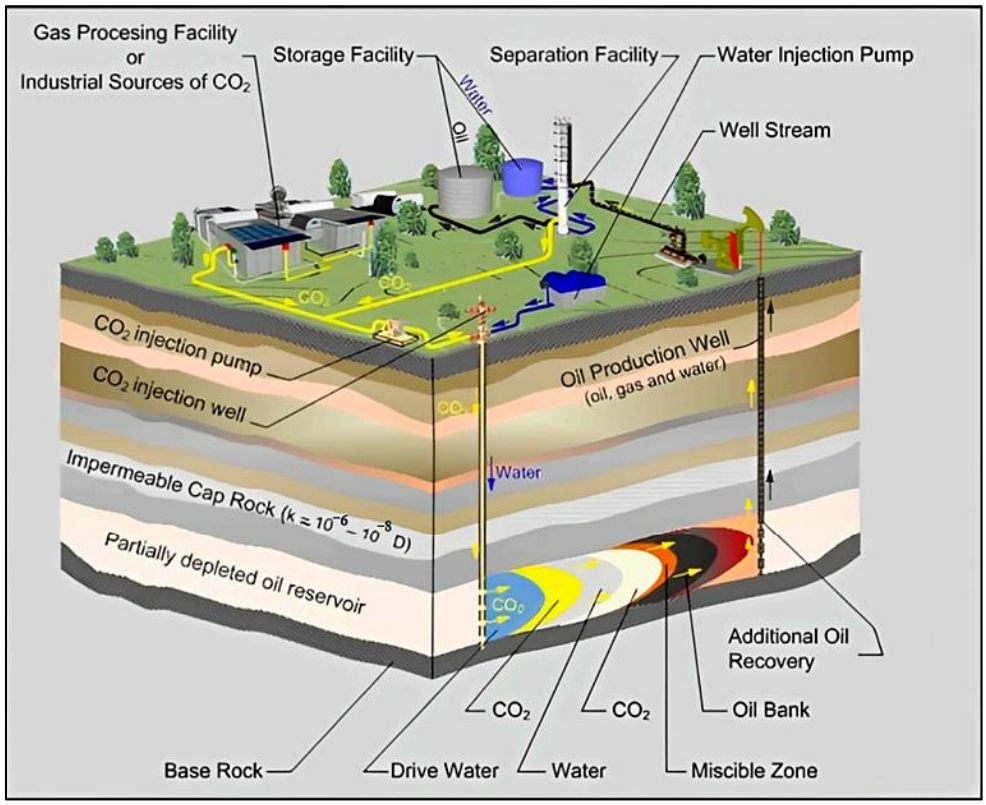

Figure 2.3 CO_2 Storage Mechanism in Depleted Reservoirs.

Source : Gaurina-Međimurec & Novak Mavar (2020)

2.3 Assessment of CO_2 Storage Mechanism

The success of geological storage is often incorporated with the various CO_2 storage mechanisms. The main storage mechanisms that are commonly found in geological storage are structural trapping (Y. Wang et al., 2022), residual trapping (Baban et al., 2023), solubility trapping (Punnam et al., 2022), mineral trapping (Zhang et al., 2024), and adsorption trapping (Jia et al., 2024), as illustrated in Figure 2.4. Structural trapping occurs due to buoyancy forces, where supercritical CO_2 remains trapped beneath a caprock. Residual trapping, also known as capillary trapping, occurs when supercritical CO_2 is trapped within the rock formation due to capillary forces. Solubility trapping refers to the dissolution of CO_2 into a liquid within rock formation. Mineral trapping involves the geochemical interaction between CO_2 and minerals, forming a new stable mineral through the mineralisation process. Lastly, adsorption trapping is where CO_2 molecules attach to the surface of the solid medium, such as minerals.

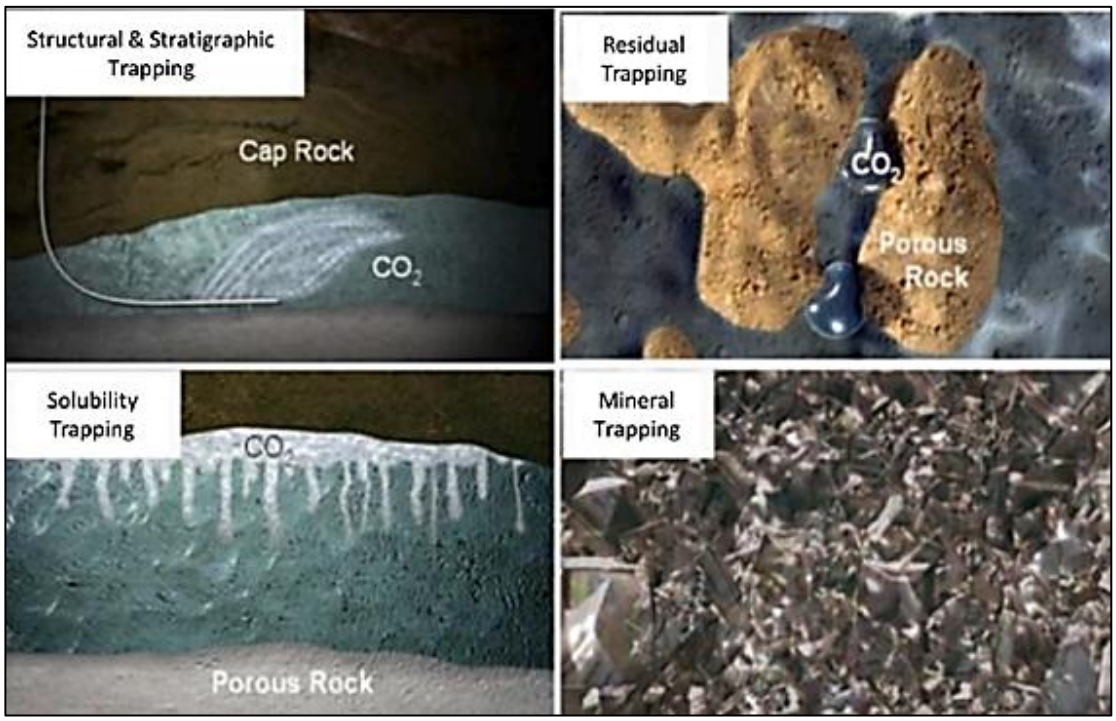

Figure 2.4 CO_2 Trapping Mechanism Involved in the Geological Storage.

Source : Leng et al. (2024)

These mechanisms are affected by temperature, pressure, and the salinity of the water (Leng et al., 2024). Although mineral and adsorption trapping might seem to be

similar, the two methods are differentiated by their underlying mechanisms: mineral trapping is controlled by geochemical reactions driven by CO_2 reactivity that create new mineral phases after a thousand years (Pearce et al., 2022), and adsorption trapping is a process of physical and chemical bonding of CO_2 molecules to mineral surfaces, which occurs before the mineralisation (Bashir et al., 2024). Among these processes, adsorption trapping deserves more attention because of its peculiarities of physical and chemical processes, which are discussed in the following section.

2.3.1 Adsorption Mechanism

The adsorption mechanism offers a route to long-term immobilisation in the CO_2 geological storage. Competitive adsorption processes have been explored in several studies, and the correlation between various CO_2 adsorbents and the adsorption capacities of these adsorbents has been considered (Mechnou et al., 2024; Qiao & Fu, 2025; Y. Zhang et al., 2025). Mineral-based adsorbents exhibit significant potential for CO_2 capture, governed by both internal and external factors. Internal controls on adsorption include mineral surface properties and pore structure, whereas external factors comprise temperature, pressure, and fluid composition. The following section provides a detailed explanation of the fundamental principles governing the adsorption mechanism and the factors that influence it.

2.3.2 Types of Adsorption Mechanisms

Adsorption is a surface process in the form of gases or liquids, which are multi-component, and stick to the surface of a solid medium (Nema et al., 2025). It is broadly divided into two types, namely, physical adsorption (physisorption) and chemical adsorption (chemisorption), and the criteria used to distinguish between them are summarised in Table 2.1.

Physisorption refers to a weak intermolecular interaction between fluid molecules and a solid surface, primarily governed by London van der Waals forces. Conversely, chemisorption is motivated by the stronger forces of chemical bonding between adsorbate molecules and the solid medium (Xu et al., 2024). The two mechanisms are critical in the selectivity and affinity of CO_2 molecules to mineral surfaces or other adsorbents.

Table 2.1
Difference between Physical Adsorption and Chemical Adsorption.

Criteria	Physical Adsorption	Chemical Adsorption
Attraction Force	Van der Waals forces	Ionic or covalent bond
Specificity	Unspecific	Very specific
Nature of adsorption	Depending on the nature of the geological formation.	Depending on the nature of the geological formation.
Reversibility	Reversible or Partially Reversible process.	Mainly irreversible
Temperature	Not conducive to high temperatures.	Conducive under high temperatures.
Enthalpy	Low	Higher than physical adsorption.
Activation energy	Does not require high activation energy.	Require high activation energy.
Layer of adsorption of the interfacial region (saturation)	Multi layers	Mono layer

Source: Alaqarbeh (2021)

2.4 Fundamentals of Adsorption on Minerals

The interaction between CO_2 molecules and mineral surfaces occurs in adsorption processes in geological formations. The minerals commonly found in nature and relevant to these processes include olivine, pyroxene, amphibole, biotite, plagioclase, andalusite, staurolite, garnet, actinolite, and oolite (Romaine, 2020). These minerals fall under various mineralogical categories: silicates, carbonates, sulphates, oxides, sulfides, halides, native elements, phosphates, and energetic minerals, which are determined by their chemical composition (Irannajad et al., 2019).

The evolution of minerals over geologic time is associated with element substitution, fluid-rock interactions, and biologically mediated changes, which result in mineral assemblage diversification (Hazen et al., 2023; Hazen & Morrison, 2022). The resulting evolutionary effect is the variation in mineralogical properties, such as chemical composition, crystal structure, and physical properties such as hardness, colour, and density (Ali et al., 2022; Peretomode et al., 2022). These characteristics greatly affect the ability and selectivity of minerals to adsorb CO_2 molecules, and hence their suitability for long-term storage.

2.5 Factors Affecting Adsorption in Natural Minerals

The adsorption capacity of a mineral is the maximum amount of CO_2 that can be adsorbed onto its surface, that determine using the isotherm models (T. Wang et al., 2023). This adsorption capacity is influenced by the internal and external factors. Internal factors are the characteristics of the pore (specific surface area and pore volume), mineralogical (mineral type and content of clay), and organic matter (content, type, and maturity) (X. Li et al., 2024). The external factors are primarily associated with operating conditions such as temperature, pressure, moisture content, and CO_2 concentration (Gunawardene et al., 2022). These factors are discussed in greater detail in the following subsections.

2.5.1 Surface Area and Pore Size Distribution

Adsorption takes place on the surface of minerals, and therefore, the more the surface area, the higher the adsorption capacity (Hacıosmanoğlu et al., 2022). Particle size and pore size are the primary factors that determine the surface area. There are usually four categories of pores: micropores (<10 nm), transition pores (10 - 100 nm), mesopores (100 - 1000 nm), and macropores (1000 nm and above) (H. Li et al., 2024). Geological and environmental factors that influence the development and variation of particle size and pore size include temperature, pressure, and fluid interactions. Micropores and transitional pores are the most effective adsorption sites, as they contribute substantially to the total available surface area. The greater the number of these pores, the greater the possibility of adsorbing CO_2 molecules and thus increasing the total storage capacity.

2.5.2 Chemical Structure

Determining the chemical structures of minerals is critical to the selectivity of CO_2 molecules in CO_2-mineral reactions. These structures are usually characterised using Fourier-transform infrared spectroscopy (FTIR) and grouped into a few functional groups. The most effective groups to adsorb CO_2 are oxygen-containing groups, i.e., hydroxyl (-OH) and carboxyl (– COOH) (He et al., 2023; Yin, Dong, et al., 2025), metal carbonate (CO_3^{2-}) (B. Jin et al., 2024; J. Wang, Chen, et al., 2025), and metal oxygen

(M-O) groups (Le et al., 2023; J. Luo et al., 2024; R. Sun et al., 2025). The hydroxyl and carboxyl groups have a high adsorption affinity to weakly polar CO_2 molecules because of the hydrogen bonding and electrostatic interactions (C. Chen et al., 2022; Guang et al., 2025). Likewise, metal carbonate and metal-oxygen groups react with CO_2 by chemical bonding to form stable mineral phases that trap CO_2 over long durations, often termed as mineralisation. The functional group's role is thus a key consideration in the increase in CO_2 adsorption capacity.

2.5.3 Mineral Composition

Geological storage sites commonly consist of clay, siltstone, and small quantities of endogenic carbonates, biological silica minerals, and phosphates (Lyu et al., 2019). Each mineral possesses distinctive characteristics that cannot be easily described in words. They display considerable variability in pore characteristics and mineralogical properties (L. Liu et al., 2024), with the chemical structure of the minerals exerts a dominant control on adsorption mechanisms (Guang et al., 2025).

Mineral compositions are generally used to determine the source rocks (igneous, sedimentary, or metamorphic) and how much of each mineral they contain in the stratum. The mineral composition must be examined accordingly to assess the high-adsorption minerals. Consequently, the abundance of high-adsorption minerals at a specific stratum significantly contributes to the potential geological sites for CO_2 molecule adsorption.

2.5.4 Operating Condition

As the internal factors play a significant role in adsorption, external factors, such as temperature, pressure, and gas flow rate, also have a different impact on adsorption efficiency. In most scenarios, adsorption efficiency is very poor at high temperatures because of the aggressive kinetic movement of CO_2 molecules, which leads to weak interaction with the adsorbent (Aquino et al., 2020; Ghazali et al., 2020; Gheytanzadeh et al., 2021; Y. Liu & Hou, 2020; Mohammad et al., 2019; Mukherjee et al., 2019).

On the other hand, the pressure obeys the Langmuir monolayer adsorption theory (L. Li et al., 2023; Lin et al., 2023). As the pressure increased, the adsorption capacity started to increase rapidly. When the pressure exceeds a certain threshold, the

adsorption capacity continues to increase, albeit at a slower rate. Eventually, the pressure stabilises, and the system reaches an equilibrium adsorption state.

Gas flow rate also contributes to the adsorption process. Adequate gas flow rate is essential for effective adsorption. A moderate flow rate is recommended to provide an optimum contact time or interaction between CO_2 molecules and the solid surface (Biswas et al., 2020).

2.6 Assessment of the Clay Mineral Adsorption Potential

The stability of mineral-based CO_2 storage is determined by the interaction of CO_2 with alkaline oxides and silicate minerals that change into stable carbonate phases (Z. Song et al., 2024). When mineralised, CO_2 is practically fixed in the solid matrix, and there is a low probability of re-emission into the atmosphere. However, the process of dissolution of metal oxides before the formation of carbonates is usually slow, which restricts the overall efficiency of long-term storage (Yin, Zhang, et al., 2025). Such reactive components are commonly found in clay minerals, which are common in most geological reservoirs. Clay minerals, nevertheless, are still in the centre of scientific discussions because of their dual properties of increasing CO_2 storage capacity through adsorption while also impacting the integrity of the geological reservoirs (El-Masry et al., 2025).

Several types of clay minerals and their corresponding characteristics are presented in Table 2.2. These minerals are increasingly recognised as promising candidates for CO_2 storage due to their abundance, non-toxicity, and distinctive physicochemical properties. The important properties like pore size, surface area and chemical structure differ depending on mineral composition and distribution in the formation (X. Yang, Zhou, et al., 2024). Specifically, minerals with larger surface areas and well-defined chemical structures exhibit a stronger affinity for CO_2, making clay minerals particularly significant in storage studies.

Kaolinite, montmorillonite, illite and chlorite are the most common clay minerals found in geological storage systems (Q. Zhang et al., 2024). These minerals also have metal ions like Ca^{2+}, K^{+}, Mg^{2+}, Na^{+}, Al^{3+}, and Si^{4+}, which are involved in mineralisation via dissolution-precipitation reactions. The exchange of ions between minerals and formation fluids involves reactive ions such as Ca^{2+}, Mg^{2+}, Al^{3+}, and Si^{4+} as key participants (Z. Wang et al., 2024). These reactions lead to the formation of stable

carbonate minerals under high temperature and pressure conditions, ensuring the long-term immobilisation of CO_2. Nevertheless, mineralisation is a comparatively slow process, and therefore, to prevent leakage, precautionary steps are necessary during the short-term storage period to maintain the integrity of the site until full stabilisation is achieved.

Regarding the pore size distribution, most clay minerals have micropores and mesopores in the overall pore volume (Murugesu et al., 2023). Smaller pores offer a higher number of adsorption sites through the increased surface area. Above all, the CO_2 adsorption capacity of montmorillonite is high because of the large volumes of interlayer pores and the high density of adsorption sites (Bø Hunvik et al., 2021). It is remarkable swelling capacity, resulting from the isomorphic substitution of Al^{3+} for Si^{4+} or Mg^{2+} for Al^{3+}, expands the interlayer spacing and surface area, thereby enhancing the CO_2 adsorption capacity (Niu et al., 2024).

Table 2.2
Basic Information on Clay Minerals.

Ratio	Clay Mineral	Chemical Formula	CEC (meq/100 g)	Surface Area (m^2/g)
1:1 type layer	Kaolinite	$Al_4Si_4O_{10}(OH)_8$	1-5	8-15
1:1 type tube	Halloysite	$Al_4[SiO_{10}](OH)_8 \cdot nH_2O$	13	45-75
2:1 type layer	Montmorillonite	$(Na, Ca)_{0.33}(Al, Mg)_2(Si_4O_{10})_2(OH)_2 \cdot nH_2O$	80-120	600-800
	Vermiculite	$Mg_5(H_2O)_4[SI_4O_{10}]_2(OH)_2$	100-150	5-400
	Illite	$K_{1-1.5}Al_4[Si_{6.5-7}Al_{1-1.5}O_{20}](OH)_4$	10-40	10-100
2:1 type layer-chain	Sepiolite	$Mg_8Si_{12}O_{30}(OH)_4(H_2O)_4 \cdot 8H_2O$	20-30	170-370
	Palygorskite	$Mg_5(H_2O)_4[Si_4O_{10}]_2(OH)_2$	30-40	120-200

Source: X. Yang, Zhou, et al. (2024)

2.7 Review of the Mineralogical Identification Technique

Mineralogical composition information is necessary to evaluate the mineral trapping mechanism in large-scale CO_2 geological storage studies and is considered to be the safest and most stable CO_2 geological storage (L. Sun et al., 2023). However, to gain information on mineralogical composition is challenging and costly. The techniques for mineralogical identification are widely conducted in both laboratory-scale and field-scale measurements, particularly in mineral exploration. However, for

petrophysicists, mineralogical interpretation primarily relies on the utilisation of well log data.

2.7.1 Laboratory-Scale and Field-Scale Measurement Techniques

Direct measurement techniques of mineralogical identification, like Raman spectroscopy (Das & Agrawal, 2011), X-ray diffraction (XRD) (Warren, 2012), and hyperspectral imaging (C. I. Chang, 2003), are mainly used for mineral exploration. Raman spectroscopy detects unique characteristics from each mineral through molecular vibrations and crystal lattice structure. XRD also measures the mineralogy through the crystal lattice structure, where it works on simple identification. Hyperspectral imaging is a method that involves reflectance spectra to detect several mineral groups. However, the online usage of these techniques is very limited. Therefore, there are significant changes in traditional techniques that provide real-time mineralogical analysis for geologists.

Laser-induced breakdown spectroscopy (LIBS) (Cremers & Radziemski, 2013) and X-ray Fluorescence (XRF) (Beckhoff et al., 2007) measurement techniques both perform better than the conventional techniques. LIBS uses a high-powered laser to create a plasma, then analyses the light emitted from the plasma to determine the elemental composition. Besides, XRF bombards a sample with X-rays, causing the atoms to emit characteristic fluorescent X-rays and, hence, determining the elemental composition. Despite such advances, there are significant drawbacks, including financial crisis due to expensive lab equipment, specialised personnel, and extensive fieldwork, limited size of exploration coverage, and intricate mineral identification (Radulescu et al., 2024).

2.7.2 Lithology Classification

In petroleum engineering, the mineralogical identification is based on human or algorithmic interpretation. Lithology classification is a geological interpretation method, which is a core part of reservoir modelling, drilling, and wellbore management (G. Chen et al., 2020; Shuvo & Joy, 2024). It is the basis of sedimentary reservoir studies, including the study of the sedimentary facies, rock colour, composition, texture and structure (Cui et al., 2022). However, lithofacies analysis provides limited visualisation,

as it does not reveal the complete mineral composition of the stratum. In comparison, mineralogical data provide a better understanding of stratigraphy and hence enhance accuracy and continuity in characterising the subsurface. This has made mineral identification a crucial focus in addressing the otherwise hidden heterogeneity of geological formations. Well logs have become a standard component of most log analysis systems for identifying mineral compositions. As an example, W. Hussain et al. (2024) examined the correlation between spectral gamma ray logs and mineral composition through cross-plot analysis (Figure 2.5). This method is useful in determining clay content and gives credible results for clay-rich formations. However, it is less effective for identifying other mineral types and typically requires expert geological interpretation. Furthermore, acquiring spectral gamma ray data in field applications can be prohibitively expensive. Consequently, mathematically derived minerals are often employed as a practical compromise, either as an approximation of otherwise unmeasurable mineralogical compositions or as a hypothetical normative assemblage useful for modelling applications (Daya Sagar et al., 2018).

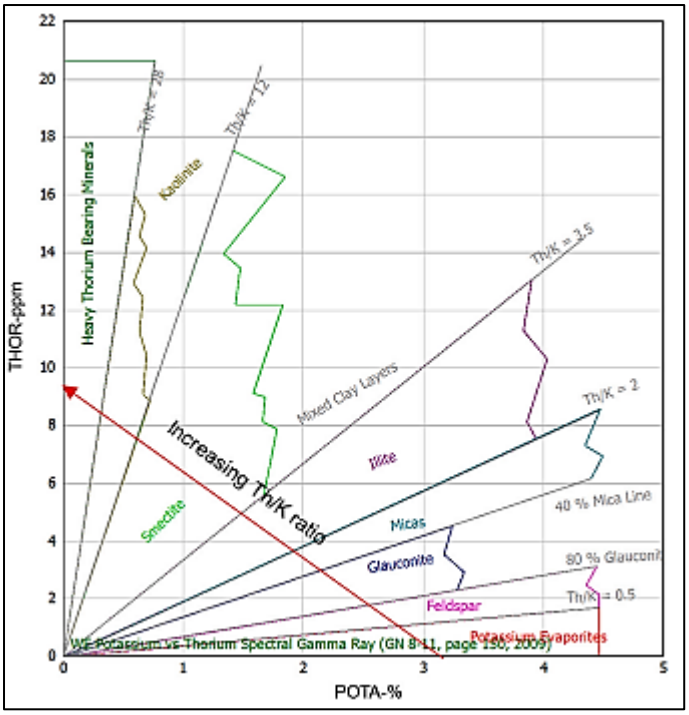

Figure 2.5 Th/K Cross-plot Technique.

Source : W. Hussain et al. (2024)

2.7.3 Numerical Technique

The conventional well logs are an effective instrument to establish mineralogical composition at continuous depths within geological formations (Kim et al., 2020). For example, the spectral gamma ray log is commonly employed to determine mineral clay content (Hussain et al., 2024), while the photoelectric factor (PEF) log provides valuable information about mineralogical information based on the average atomic number (Z) of the rock matrix properties (Ogiesoba & Palacios, 2024). Although useful, such deterministic methods are typically restricted to identifying individual minerals within a stratum rather than the complete mineral assemblage, which requires a probabilistic or mathematical method.

To address this limitation, Schlumberger (1989) proposed a mathematical approach for determining mineral composition using well log data. The technique employs a system of simultaneous equations to estimate mineral fractions, where each fraction is multiplied by the theoretical response of a specific log until the computed values match the actual log measurements. A similar implementation, known as the mineral solver, is available in the Techlog software, which typically integrates density (RHOB), neutron porosity (NPHI), and compressional sonic (DTC) logs to solve the equations (El-Bagoury, 2020). The overall concurrent equation of mineral composition estimation is formulated as follows:

$$\rho_b = \phi \cdot \rho_f + (1 - \phi)(Q \cdot \rho_Q + C \cdot \rho_C + D \cdot \rho_D) \tag{2.1}$$

$$\phi_N = \phi \cdot \phi_f + (1 - \phi)(Q \cdot \phi_Q + C \cdot \phi_C + D \cdot \phi_D) \tag{2.2}$$

$$t = \phi \cdot t_f + (1 - \phi)(Q \cdot t_Q + C \cdot t_C + D \cdot t_D) \tag{2.3}$$

$$1 = Q + C + D \tag{2.4}$$

Where ρ_b, ϕ_N, and t are bulk density, neutron-porosity, and interval transit time by the density, neutron, and sonic log, respectively; ρ_f, ϕ_f, and, t_f are density, hydrogen index of the fluid, and pore fluid transit time, respectively; ϕ is the porosity; ρ_Q, ρ_C, and ρ_D are the density of quartz, calcite, and dolomite, respectively; ϕ_Q, ϕ_C, and ϕ_D are the neutron porosity of quartz, calcite, and dolomite, respectively; t_Q, t_C,

and t_D are the interval transit time of quartz, calcite, and dolomite, respectively; and Q, C, and D are the fractions of quartz, calcite, and dolomite in the rock matrix mixture. The limitation is that the simultaneous equation specifically solves for four unknown variables (Q, C, D, and ϕ). Increasing variables is more complex because additional log measurements must respond to the same thing.

2.8 Techniques for Predicting Mineralogical Composition in Subsurface Formations

The mineral identification was accomplished through the manual interpretation of well log data using lithology classification (M-N cross-plot, neutron-density cross-plot, sonic-neutron cross-plot, MID cross-plot, and Th/K cross-plot) (Abudeif et al., 2025; Mohamed et al., 2024). However, these techniques are both labour-intensive and time-consuming. In recent years, artificial intelligence (AI) has increasingly been adopted in petroleum engineering to automate workflows across multiple domains, including geophysical/petrophysical interpretation (Isah et al., 2025), drilling and well engineering (Chuka Anthony Arinze et al., 2024), production technology (Hanif, 2024), and reservoir management (Q. Feng et al., 2025). Consequently, the implementation of AI-based approaches offers significant potential to replace manual interpretation methods and to enable more efficient and consistent identification of mineral groups.

2.8.1 Comparative Analysis of the Machine Learning Model

As the technology evolved, machine learning (ML) algorithms have been actively utilised in oil and gas exploration to develop a reliable and efficient model for multiple prediction tasks. It explains the non-linear relationship by detecting the factors among multiple features (D. Kim et al., 2020). Table 2.3 briefly lists a few latest start-of-the-art techniques using ML from years 2020 to 2026 to identify the mineralogical properties that are significantly revolutionising the oil and gas exploration.

Among the earlier studies, D. Kim et al. (2020) demonstrated that deep neural networks (DNNs) could effectively address geophysical problems involving complex non-linear equations. Their trained model successfully predicted the mineralogical composition of quartz, K-feldspar, calcite, dolomite, pyrite, and clay using conventional well logs and X-ray diffraction (XRD) data obtained from core plugs.

Table 2.3
Start-of-the-Art Techniques Using ML for Mineral Composition Identification.

Literature	State-of-the-art techniques	Dataset/Location	ML algorithms
D. Kim et al. (2020)	Predicting Mineralogy by Integrating Core and Well Log Data	Conventional well logs and 81 samples of XRD from Canning Basin, Australia	Deep neural network (DNN)
Asante-Okyere et al. (2021)	TOC Estimation using Mineralogy and Geophysical Well Log Data	91 samples of TOC values, mineralogy logs and conventional well logs from Sichuan Basin, China	Convolutional neural network (CNN)
de Oliveira et al. (2021)	Stepped Machine Learning for the Development of Mineral Models	1376 rock samples of XRF and XRD analysis located at Santos Basin, Brazil	Multilayer Perceptron (MLP), Generative Adversarial Networks (GAN), Random Forest, and XGBoost
C. Li et al. (2021)	Mineral Classification using Scanning Electron Microscopy - Energy Dispersive X-Ray Spectroscopy (SEM-EDS) Images	2 shale samples of SEM-EDS images data	Logistic Regression (LR), Linear Support Vector Machine (SVM), k-Nearest Neighbor (k-NN), Random Forest (RF), and Artificial Neuron Networks (ANN), and a deep learning CNN U-Net model
Cui et al. (2022)	Identification of Lithofacies and Prediction of Mineral Composition in Shales	152 samples of XRD data from Bohai Bay Basin, China	Back Propagation (BP) neural network coupled with Atomic Search Optimisation (ASO) algorithm
Park et al. (2022)	Quantification of Mineral Composition on Gas Hydrate-Bearing Sediments	94 samples of XRD data from Ulleung Basin, Korea	Convolutional neural network (CNN), recurrent neural network (RNN), multi-layer perceptron (MLP), and random forest (RF)
Rangel Gavidia et al. (2023)	Characterization of Mineralogy and Facies in a Pre-Salt Carbonate Reservoir	Cores, wireline logs, and multi-mineral petrophysical evaluation from 47 wells from the Santos Basin, Brazil	Unsupervised self-organising map (SOM), random forest (RF), and XGBoost

K. Hu et al. (2023)	Mineralogical Characterisation from Geophysical Well Logs	Core samples, borehole geochemical logging tool (GLT), and conventional geophysical logs from multiple wells from the Horn River Basin, Canada	A combination of a convolutional neural network (CNN) with XGBoost
H. Jin et al. (2024)	Prediction Of The Mineral Composition on Gas Hydrate Sediments	488 sediment samples from Ulleung Basin, East Sea	Long short-term memory (LSTM), multilayer perceptron (MLP), random forest (RF), and , Convolutional neural network (CNN)
H. Wang et al. (2024)	Mineralogy Interpretation and CO_2 Saturation Estimation in Geological Carbon Storage	11,700 data points of conventional well logs and 1600 data points of neutron logging (PNL) from the Illinois Basin, USA	Ridge regression (RR), random forest (RF), gradient boosting regression (GBR), support vector regression (SVR), and artificial neural network (ANN)
Guo et al. (2026)	A Shale-Oil Reservoir Multi-Mineral Inversion Method Based On Well-Logging Data	Elemental logging Conventional well logs, and core measurement located at Ordos Basin, China	Random Forest (RF) model – Sparrow–Bald Eagle Optimisation Algorithm (SBOA), back-propagation neural networks (BPNN), XGBoost, and multivariate regression.

Subsequently, Asante-Okyere et al. (2021) investigated total organic carbon (TOC) estimation using convolutional neural networks (CNNs) by integrating shale mineral composition and well log data. As ML applications in mineralogical prediction gained increasing attention, de Oliveira et al. (2021) employed several ML algorithms, including Multilayer Perceptron (MLP), Generative Adversarial Networks (GAN), Random Forest (RF), and Extreme Gradient Boosting (XGBoost), to improve mineral prediction models derived from X-ray fluorescence (XRF) and XRD datasets. Furthermore, C. Li et al. (2021) applied Logistic Regression (LR), Linear Support Vector Machine (SVM), k-Nearest Neighbour (k-NN), Random Forest (RF), Artificial Neural Networks (ANN), and a CNN U-Net deep learning model for the classification

of thirteen mineral phases from Scanning Electron Microscopy–Energy Dispersive X-ray Spectroscopy (SEM–EDS) images. Their findings indicated that RF achieved superior classification performance compared to the other models.

In 2022, Cui et al. (2022) proposed a Backpropagation (BP) neural network integrated with Atomic Search Optimisation (ASO) for mineral content prediction and lithofacies identification using well logging and XRD data. The proposed model demonstrated strong capability in identifying lithofacies in uncored wells. Similarly, Park et al. (2022) evaluated four ML algorithms, namely CNN, Recurrent Neural Network (RNN), multi-layer perceptron (MLP), and random forest (RF), to predict the mineral composition of twelve minerals using XRD data. Among the evaluated models, RF achieved the highest prediction accuracy.

In the following year, Rangel Gavidia et al. (2023) combined XRD, multimineral petrophysical evaluation, and well log data to train ML models for accurate mineral composition prediction. The study employed Self-Organising Maps (SOM), RF, and XGBoost, with RF and XGBoost demonstrating superior predictive performance. In addition, K. Hu et al. (2023) highlighted the importance of ML-based mineralogical analysis for reservoir evaluation by integrating CNN and XGBoost models with XRD, Geochemical Logging Tool (GLT), and conventional geophysical log data to achieve accurate mineralogical characterisation.

More recent studies have further expanded the application of ML in mineral prediction. H. Jin et al. (2024) introduced a novel preprocessing framework incorporating Long Short-Term Memory (LSTM), MLP, RF, and CNN models to develop a robust deep learning approach for predicting the composition of twelve minerals from XRD data. In the same year, Wang et al. (2024) extended the application of ML to large-scale CO_2 geological storage projects by predicting mineralogical composition from conventional well logs. Their study evaluated Ridge Regression (RR), RF, Gradient Boosting Regression (GBR), Support Vector Regression (SVR), and ANN models, where GBR and RF achieved the best prediction performance for mineral fraction estimation.

More recently, Guo et al. (2026) proposed an improved RF model optimised using the Sparrow–Bald Eagle Optimisation Algorithm (SBOA), alongside Backpropagation Neural Networks (BPNN), Gradient Boosting Decision Trees (GBDT), and multivariate regression models, to predict five mineral groups and

kerogen content. The proposed optimisation framework significantly reduced prediction errors, particularly for clay mineral groups.

Overall, previous studies demonstrate the growing significance of ML techniques in mineralogical prediction and reservoir characterisation. Among the various algorithms investigated, ensemble learning approaches such as RF and XGBoost consistently exhibit superior predictive performance due to their ability to model complex non-linear relationships and handle high-dimensional structured datasets effectively. In particular, Extreme Gradient Boosting (XGBoost) has emerged as one of the most robust and reliable ML algorithms for regression and classification tasks, often outperforming conventional ML approaches in capturing intricate relationships between mineralogical properties and petrophysical parameters derived from well logs, XRD, and geochemical datasets. Therefore, XGBoost offers substantial potential for further research and development, particularly in improving automated mineral prediction, reducing uncertainty in subsurface modelling, and supporting more reliable reservoir management and carbon storage strategies in the oil and gas industry.

2.8.2 Extreme Gradient Boosting (XGBoost)

XGBoost is a supervised machine learning algorithm that is grounded on the gradient boosting framework (T. Kumar et al., 2022). Its high performance in processing large data sets, which provides speed, efficiency and predictive accuracy, has made it a popular algorithm in model development. The gradient boosting algorithm operates on the principle of sequentially constructing an ensemble of decision trees, where each subsequent tree is designed to minimise the residual errors left by the preceding ones (Gonçalves & De Carvalho, 2025). Unlike algorithms such as bagging, which average the outputs of weak independent learners, gradient boosting strengthens the final model through iterative refinement of predictions. One of the main strengths of XGBoost is that it includes regularisation measures that restrict the complexity of the model, minimise overfitting, and improve the ability to predict new data (P. Zhang et al., 2022). The regularised objective function may be stated as follows:

$$L(\varphi) = \sum_{i} l(y_i - \hat{y}_i) + \sum_{k} \Omega f(k) \tag{2.5}$$

Where L represents the loss function, which is the difference between the predicted ($\hat{y}_i$) and actual value (y_i), and Ω is the regularisation term that depends on the complexity of the problem, and it is expressed as:

$$\Omega(f_k) = \gamma T + \frac{1}{2}\lambda \|w\|^2 \tag{2.6}$$

In the above equation, the regularisation parameters for γ and λ represent the degree of complexity. Larger values make the structure of the tree more complex. While T and *w* represent the number of leaf and leaf nodes, respectively. The function of *f* is added to minimise the loss objective function to improve the model.

2.9 Adsorption Isotherm Models: Principles and Interpretations

Several authors have suggested adsorption isotherm models as a valid approach to forecasting CO_2 storage capacity (AL-khulaidi et al., 2024; S. Han et al., 2023, 2024). Various models have been created, such as the Langmuir, Freundlich, Toth, Sips, Dubinin-Radushkevich, Ono-Kondo, Temkin, and Brunauer-Emmett-Teller (BET) models. The most used of these are the Langmuir and the Freundlich isotherms, which give consistent results for the amount of gas adsorption. Overall, the adsorption isotherm models define the correlation between the uptake of the gas and a porous solid medium at different pressures in an isothermal environment (Hamza, Hussein, Al-Marri, Mahmoud, Shawabkeh, et al., 2021). Each model possesses specific advantages and limitations that are crucial in selecting the most appropriate model for CO_2 adsorption under varying temperature and pressure conditions. Table 2.4 summarises the adsorption isotherm models with their non-linear expressions.

Table 2.4
List of Adsorption Isotherm Models.

Adsorption Isotherm Model		Non-linear Expression	Literature
Two-parameter model	Langmuir	$q_e = q_m \frac{K_L C_e}{1+K_L C_e}$	(Vitek & Masini, 2023)
	Freundlich	$q_e = K_F C_e^{1/n_F}$	(Mabuza et al., 2022)
	BET	$q_e = \frac{q_m C \left(\frac{P}{P_0}\right)}{\left(1-\frac{P}{P_0}\right)\left[1+(C-1)\left(\frac{P}{P_0}\right)\right]}$	(Piccin et al., 2017)
	D-R	$q_e = q_m e^{-K_{DR}\varepsilon^2}$	(Q. Hu & Zhang, 2019)
Three-parameter model	D-A	$q_e = q_m e^{-\left(\frac{\varepsilon}{E_0}\right)^{n_{DA}}}$	(Y. Sun et al., 2020)
	Toth	$q_e = \frac{q_m K_T C_e}{\left(1+K_T C_e^{n_T}\right)^{\frac{1}{n_T}}}$	(Al-Ghouti & Da'ana, 2020)
	Sips	$q_e = \frac{q_m K_S C_e^{n_S}}{1+K_S C_e^{n_S}}$	Abunowara et al. (2023)

2.9.1 Langmuir Isotherm Model

One of the most common adsorption isotherms, the Langmuir model, is used to describe both physisorption and chemisorption, and has been commonly used to model CO_2 adsorption on shale rocks (J. Zhou et al., 2019). This model presupposes a uniform adsorption surface with the same energy sites and monolayer coverage (Alafnan et al., 2021; Ragadhita & Nandiyanto, 2021), which simplifies the fact that porous geological formations are heterogeneous in nature (Duan et al., 2018). Nevertheless, it remains widely used because of its simplicity, ease of application, and capability to describe adsorption behaviour under subcritical pressure and temperature conditions (K. Yang et al., 2021).

However, the Langmuir model becomes unreliable at high pressures, as it tends to overestimate the volume of adsorbed gas compared to experimental observations (Shen et al., 2021; X. Song et al., 2018; Tian et al., 2016). Its applicability also diminishes under supercritical conditions. Moreover, the model lacks accuracy for multicomponent gas mixtures, as it does not account for the effects of competitive adsorption. In order to address these inadequacies, researchers tend to add empirical or semi-empirical correlations in order to improve the predictive power of adsorption isotherm models.

2.9.2 Freundlich Isotherm Model

The Freundlich model is an empirical isotherm that is usually used on heterogeneous surfaces, including silica, clays, metals, activated carbon, and polymers (Fakher & Imqam, 2020). In contrast to the Langmuir model, it does not assume homogeneity or monolayer adsorption, making it applicable for describing adsorption in complex geological formations. Nevertheless, the Freundlich model is mainly used at low pressure and fails to accurately describe the adsorption behaviour at high pressure (Fakher & Imqam, 2020)

As an example, Mabuza et al. (2022) used the Freundlich isotherm to predict CO_2 adsorption on coal surfaces and found that it was valid at low-pressure conditions but failed at high-pressure conditions. Therefore, the Freundlich isotherm is not suitable for field-scale studies since CO_2 geological storage often operates under supercritical conditions.

2.9.3 Brunauer–Emmett–Teller (BET) Isotherm Model

The Brunauer-Emmett-Teller (BET) isotherm was created to build upon the Langmuir model by considering multilayer adsorption, and it is commonly used to calculate the surface area of porous solids (Gautam et al., 2023). The BET model describes multilayer adsorption processes, unlike the Langmuir model, which only assumes monolayer adsorption, and thus is a promising alternative to complex adsorption systems. Xie et al. (2021) demonstrated the applicability of this model for CO_2 adsorption on shale surfaces, obtaining reliable results under experimental conditions.

The BET model has several limitations, even though it has its benefits. It assumes that gas molecules are first adsorbed onto a single layer, followed by the formation of additional layers, an assumption that does not always accurately represent adsorption behaviour in reservoir conditions (Fakher & Imqam, 2020). In addition, it has been tested primarily at moderate temperatures (30 and 55 °C), limiting its usefulness in geological storage, where the conditions are far more severe. The main disadvantage is that the saturation vapour pressure (Po) in the BET equation is not defined in the supercritical conditions, which requires adaptation of the initial model (S.

Zhou et al., 2019). Moreover, the BET equation is relatively complex and can be challenging to apply in practice because it requires highly precise experimental data.

2.9.4 Dubinin-Radushkevich and Dubinin-Astakhov Isotherm Model

The Dubinin-Radushkevich (D-R) and Dubinin-Astakhov (D-A) models are founded on the Dubinin-Polanyi (D-P) adsorption potential theory, which posits that adsorption occurs through the filling of micropores rather than a layer-by-layer process (Gautam et al., 2023). This makes them particularly suitable for porous solids, as the models account for the influence of pore structure on adsorption capacity. The D-R and D-A models are used both in homogeneous and heterogeneous surfaces, unlike conventional isotherms (Alberti et al., 2012; Q. Hu & Zhang, 2019).

Among these models, the D-A model has gained considerable attention due to its superior flexibility and predictive capability in describing gas adsorption behaviour in complex porous media. In general, the D-A model is usually more accurate than the D-R model, particularly in the case of highly heterogeneous adsorbents (Gautam et al., 2023). This adaptability enables the D-A model to more accurately characterise adsorption processes occurring within microporous geological materials, where pore structures are highly irregular and spatially variable.

In addition, it is also highly adaptable to different temperatures, as well as in both subcritical and supercritical conditions of CO_2 (H. Liu et al., 2019). This characteristic is particularly significant for geological CO_2 storage studies, as subsurface reservoir conditions commonly involve elevated pressures and temperatures.

Furthermore, Rani et al. (2019) investigated methane and CO_2 adsorption in shales using the Langmuir, BET, D-R, and One-Kondo isotherm models. Their findings revealed that the D-A model yielded the lowest average relative error (ARE) and sum of squared errors (SSE), thereby confirming its high precision in gas adsorption estimation. Therefore, the D-A model is considered highly significant for adsorption studies because it not only improves the accuracy of adsorption prediction but also provides a more realistic representation of adsorption mechanisms in heterogeneous porous geological systems. Its robustness, flexibility, and applicability under reservoir conditions make it a highly suitable model for advanced CO_2 adsorption and geological storage research.

2.9.5 Toth Isotherm Model

The Toth isotherm is a semi-empirical equation that is formulated as an extension of the Langmuir equation and aimed to improve the adsorption description in heterogeneous systems (K. V. Kumar et al., 2021). It introduces a third parameter to account for surface heterogeneity, assuming that adsorption energies follow a quasi-Gaussian distribution. This makes the model suitable for describing gas adsorption over a wide range of pressures. At z = 1, the Toth model reduces to the Langmuir isotherm, while increasing *z* values indicate adsorption occurring on progressively more heterogeneous surfaces.

The Toth model directly competes with the Dubinin-Astakhov (D-A) isotherm in its performance of fitting experimental data at different conditions. Although it is more flexible than Langmuir, one of the most frequent shortcomings is that it tends to overestimate the maximum CO_2 adsorption capacity, especially at high pressure (Esfandian & Rezazadeh. M., 2020; Jacobs, 2021; Noorpoor & Nazari Kudahi, 2016). However, its adaptability across different pressure ranges makes it powerful for gas adsorption estimation.

2.9.6 Sips Isotherm Model

The Sips isotherm or Langmuir-Freundlich model is a hybrid of the two methods that are used to explain adsorption in heterogeneous systems (Sips, 1948). It introduces an additional parameter to correct the unrealistic assumption of the Freundlich model, which presumes an infinite number of adsorption sites as pressure increases. The Sips model provides a more realistic representation of monolayer adsorption under high-pressure conditions by incorporating the Langmuir saturation concept.

Despite its perceived inferiority to the Dubinin-Astakhov (D-A) and Toth isotherms, the Sips model remains effective for estimating gas adsorption on both homogeneous and heterogeneous adsorbents. The Toth model has shown greater consistency with experimental CO_2 adsorption data in numerous studies than the Sips model (Abunowara et al., 2023; Serafin & Dziejarski, 2023). Nevertheless, the Sips model offers a practical balance between simplicity and accuracy, particularly in cases with limited experimental data.

2.9.7 Comparison of the Adsorption Isotherm Model

Table 2.5 summarises the assumptions and limitations of the chosen isotherm models. Key factors in evaluating the suitability of an adsorption model include its applicability, operating conditions, and underlying assumptions. Particular attention should be given to the model's ability to describe multilayer adsorption, withstand high-pressure and high-temperature conditions, represent different types of adsorbates, and capture the heterogeneity of geological formations.

Table 2.5
Comparison of Various Isotherm Models.

Isotherm model	**Assumptions**	**Limitations**
Langmuir	Gas-solid adsorption.	Does not account for multilayer adsorption.
	Chemisorption.	Assumes non-porous solids.
Freundlich	Multilayer adsorption on heterogeneous formation.	Ineffective under high-pressure conditions.
BET	Applicable for multilayer adsorption.	Limited to lower temperatures and pressures.
	Described for the surface area determination of porous solids.	Assumes uniform adsorption sites for the first layer.
D-R model	Assumes pore-filling mechanism in a solid medium.	Limited to microporous solids. Ignores electrostatic forces.
	Relies on potential theory.	
D-A model	Accounts for pore size distribution.	The equation is complex compared to the D-R model.
	Applicable at higher pressure.	
Toth	Suitable for heterogeneous formation.	More complex parameters.
	Corrects Langmuir at low and high pressure.	Requires experimental data for parameter estimation.
Sips	Multilayer adsorption on heterogeneous formation.	Limited to gas adsorption.
	Corrects Freundlich at finite adsorption sites.	Difficult to interpret parameters.

Based on this comparison, the relative suitability of the models can be ranked as follows: Dubinin–Astakhov (D-A) > Toth > Sips > Langmuir > Freundlich. The D-A model emerges as the most robust, as it effectively predicts CO_2 adsorption capacity across a wide pressure range and remains adaptable under both subcritical and supercritical conditions. Additionally, it explicitly accounts for pore size distribution, which is the key parameter influencing CO_2 adsorption, unlike most other models.

Nevertheless, the comparative analysis also highlights the fact that there is no single isotherm model that is applicable in all geological conditions to describe adsorption behaviour. Each model is based on specific assumptions that constrain its accuracy under certain conditions. Therefore, the selection of an adsorption isotherm should be guided by the research objectives and the specific geological conditions of interest, supported by a comprehensive review of existing literature.

2.10 Development of the 3D Reservoir Model for CO_2 Storage

Three-dimensional (3D) reservoir modelling is widely applied in hydrocarbon exploration to estimate reserves and optimise recovery strategies in a cost-effective manner (Ayodele et al., 2021). The process integrates geological, geophysical, petrophysical, geostatistical, and reservoir engineering data to enhance decision-making and provide a more reliable reservoir characterisation (Rahimi & Riahi, 2020). Such integration enables improved visualisation of the spatial distribution of both discrete and continuous reservoir properties (Ayodele et al., 2021). Reservoir models are typically constructed using data from well logs, core analyses, and seismic surveys.

In the context of CO_2 storage assessment, 3D reservoir modelling is essential for determining storage capacity across varying mineralogical distributions (Ricci et al., 2021). The goal is to facilitate informed decision-making on the safe and efficient storage of CO_2. A 3D model is typically built through a few stages, such as well log interpretation, structural modelling, petrophysical modelling, facies modelling, upscaling, and property modelling. A brief explanation of these models in developing the 3D reservoir model will be discussed. This serves as a fundamental framework for evaluating CO_2 storage capacity and mineralogical distribution in this study.

2.10.1 Structural Modelling

Structural modelling refers to the first process of creating a three-dimensional (3D) geological model by combining the creation of zones, faults, horizons, and pillar gridding (Khan et al., 2024). This structural framework will be integrated with other 3D models to evaluate the spatial configuration and heterogeneity of the geological formations. Figure 2.6 illustrates the creation of a 3D structural model, consisting of horizons, zones, and faults.

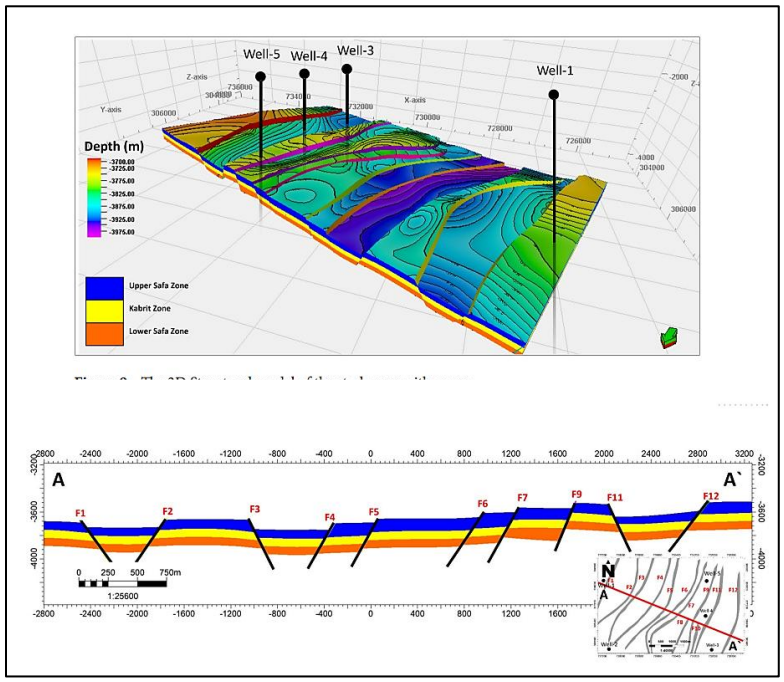

Figure 2.6 3D Structural Model.

Source : Eid et al. (2023)

2.10.2 Petrophysical Modelling

The petrophysical interpretation heavily relies on well logs, which give quantitative data on important reservoir characteristics like porosity, permeability, and water saturation (Figure 2.7). There are a variety of well logs used for the reservoir characterisation, such as gamma ray, neutron porosity, bulk density, resistivity, photoelectric, sonic, pulsed neutron capture, nuclear magnetic resonance, image logs, and elemental spectroscopy (Haagsma et al., 2021). This information is obtained from the wireline logging and is normally transformed into an electronic format.

Subsequently, the petrophysicist will utilise the well log data to conduct a reservoir characterisation across varying depths.

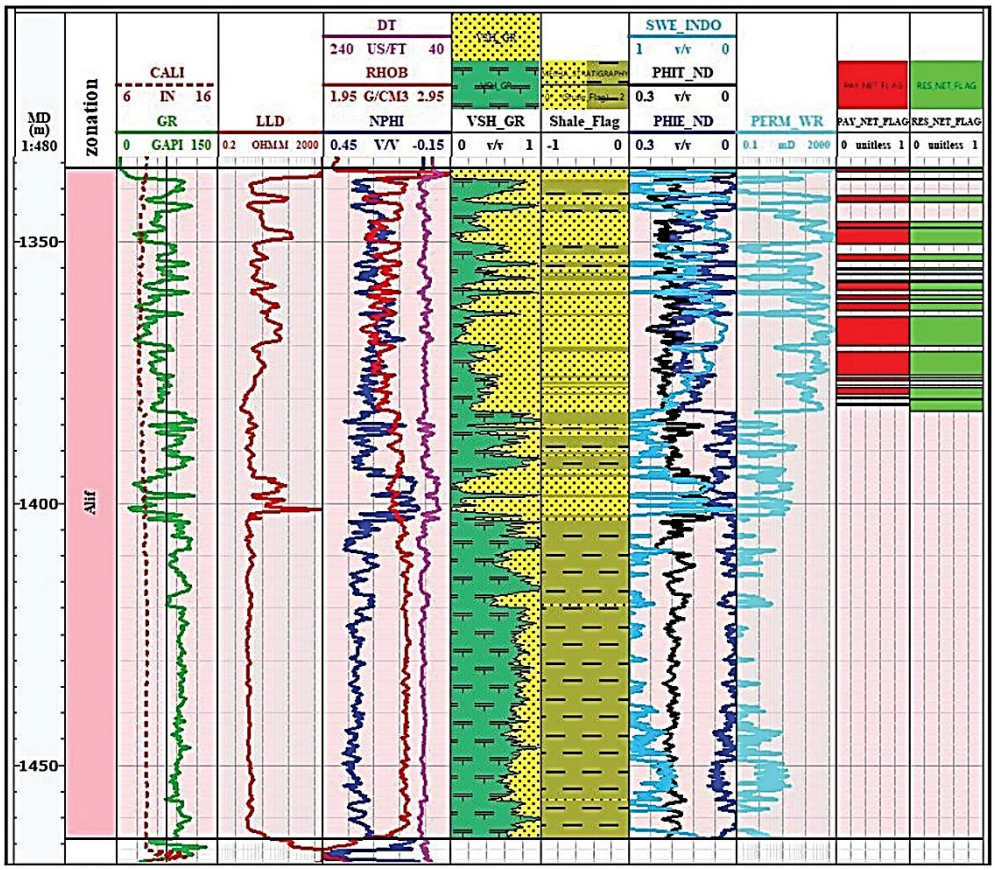

Figure 2.7 Well Log Interpretation.

Source : Kahal et al. (2024)

Table 2.6 summarises the functionalities of the different logs. As an example, the gamma ray log is commonly used to differentiate between the volume of shale and sand. Lithological data and porosity estimates are presented in sonic, neutron, and density logs. The resistivity logs are necessary to assess water saturation and permeability, and spectral gamma ray logs are used to identify the mineral composition of clay in detail (W. Hussain et al., 2024). These measurable characteristics form the basis of petrophysical modelling, where log interpretations are integrated and scaled into a three-dimensional (3D) visualisation of the reservoir.

Table 2.6
Well Log Types and Functionality.

Log types	Functionality
Gamma ray logs	Measure a radioactive element to identify shale content and lithologies.
Sonic logs	Measure sonic velocity to provide information about rock properties, such as porosity and lithology.
Density logs	Measure the bulk density of the rock to estimate porosity.
Neutron Porosity logs	Provides a hydrogen content, which is used to identify fluid types and porosity.
Resistivity logs	Measure electric resistivity to identify fluid saturation and the permeable zone.
Spectral gamma ray logs	Measures the concentrations of potassium (K), uranium (U), and thorium (Th) to identify lithologies, clay types, fractures, unconformities, and hydrocarbon potentialities.

Sources: El Sharawy & Nabawy (2018), A. K. A. Mohammed & Dhaidan (2023), Stadtműller & Jarzyna (2023)

2.10.3 Facies Modelling

The facies model is designed to introduce the heterogeneity in the distribution of rocks on a fine scale. A 2D facies log, classified using core samples, seismic data, and well logs (such as gamma ray, resistivity, and density logs), is used to generate a three-dimensional (3D) facies model through a stochastic simulation process. The popular methods for facies modelling are Sequential Indicator Simulation (SIS) and Truncated Gaussian Simulation (TGS). Figure 2.7 illustrates an example of a facies model representing a fluvial floodplain.

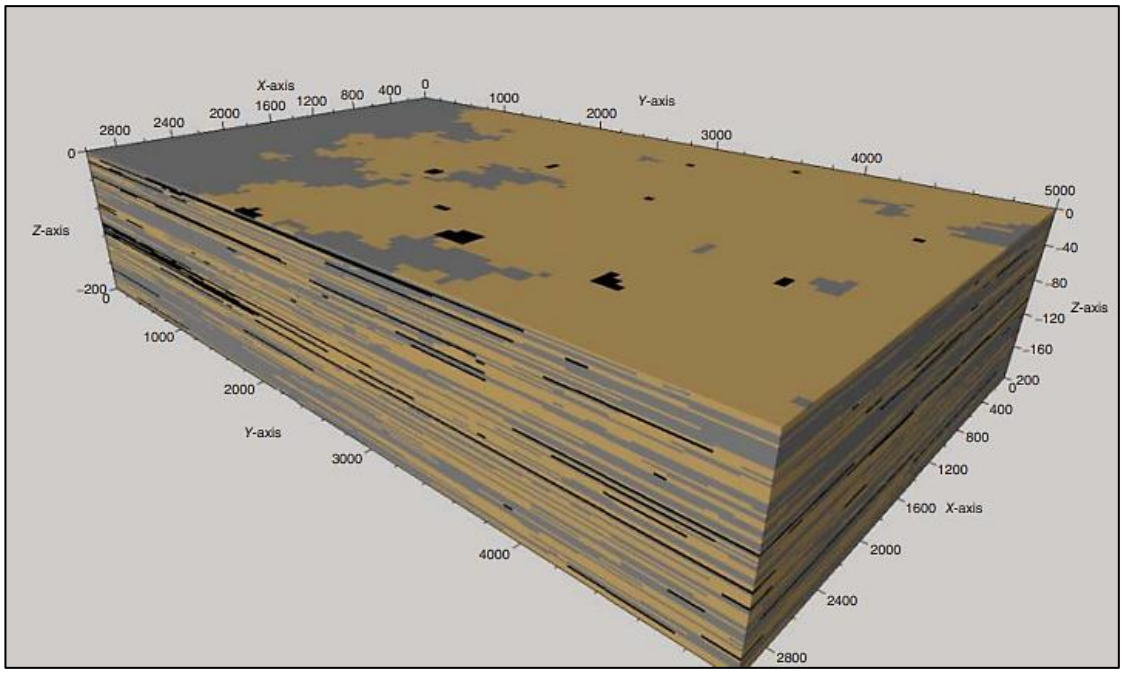

Figure 2.8 Facies Model.

Source : Cannon (2018)

2.10.4 3D Geological Modelling

Visualisation of subsurface heterogeneity, including structural frameworks such as faults, horizons, surfaces, and zonations, requires three-dimensional (3D) geological modelling. This process provides a detailed representation of reservoir architecture, which is particularly important when assessing CO_2 storage potential (Vo Thanh et al., 2019; Zapata et al., 2020). Geological modelling, with software like Petrel, combines geological and petrophysical data to allocate reservoir properties (e.g., shale volume, porosity, facies, fluid saturation, net-to-gross ratio, and permeability) throughout the model space (Khashman & Shirazi, 2023). Figure 2.9 presents the resulting porosity and permeability distributions obtained after completing the petrophysical modelling and upscaling processes.

The geostatistical method, which is stochastic in character, is central in this process. Methods that are commonly used to create continuous spatial distributions of reservoir properties include sequential Gaussian simulation (SGS), Gaussian random function simulation (GRFS), and co-kriging (Zhong & Carr, 2019). An important aspect of geostatistics is the variogram, which measures spatial correlation in the model. The

longer the variogram range, the more the continuity of the properties across distance, and the shorter the range, the weaker the spatial correlation (Madani et al., 2025).

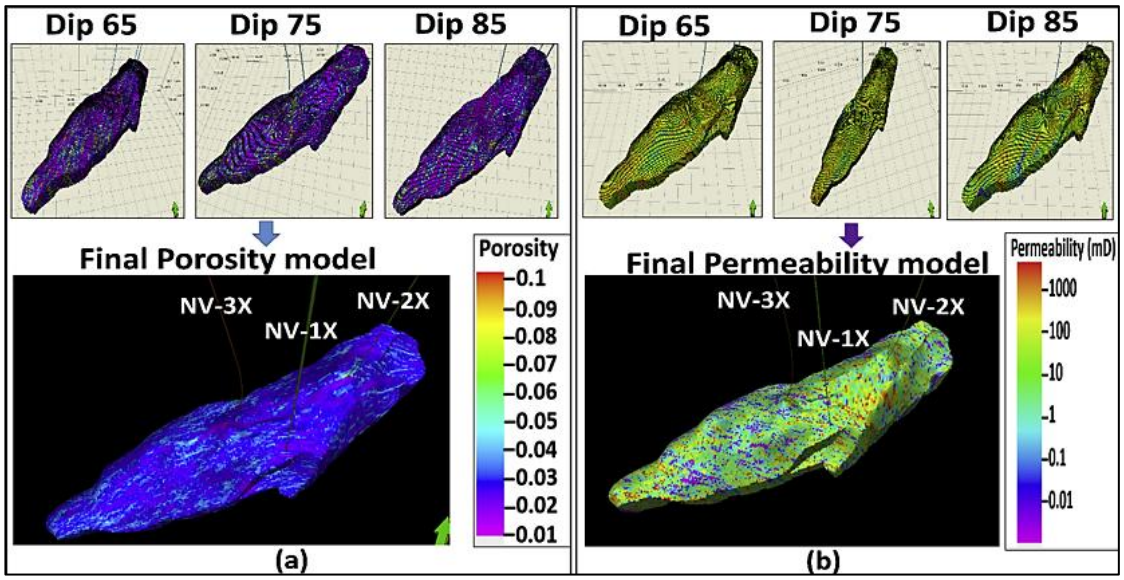

Figure 2.9 Generated Petrophysical Model. (a) Final Porosity Model and (b) Final Permeability Model.

Source : Vo Thanh et al. (2019)

2.10.5 3D Reservoir Modelling

The geological model serves as the foundation for developing a comprehensive three-dimensional (3D) reservoir model, as shown in Figure 2.10. It combines the petrophysical properties and fluid properties based on seismic interpretation, well logs, and other dynamic data, including fluid contacts, pressure-volume-temperature (PVT) analysis, and special core analysis (SCAL) (Rahimi & Riahi, 2020). Teletzke & Lu (2013) highlighted that a 3D reservoir model is essential in capturing the complexity of geological storage of CO_2 in a dynamic and predictive way. This highlights the high impact of petrophysical and geological properties on the performance of storage (Afolayan et al., 2023).

The main aim of creating a 3D reservoir model is to ensure the reliability and safety of the CO_2 storage systems in the various geological environments. This demands a combination of geochemistry, geomechanics, and engineering geology to elucidate the multiphase reactions of CO_2 with reservoir rocks and fluids. However, several key factors must be considered in identifying an optimal site for CO_2 storage (Afolayan et al., 2023):

1. A geological formation must possess adequate porosity and permeability to enable effective CO_2 injection and storage.
2. The storage formation should be located at a depth greater than 800 m below mean sea level to achieve the necessary pressure and temperature conditions (typically around 73.7 bar and 31 °C) required to maintain CO_2 in a supercritical state
3. The existence of impermeable rock in the geological formation prevents the upward migration of CO_2.

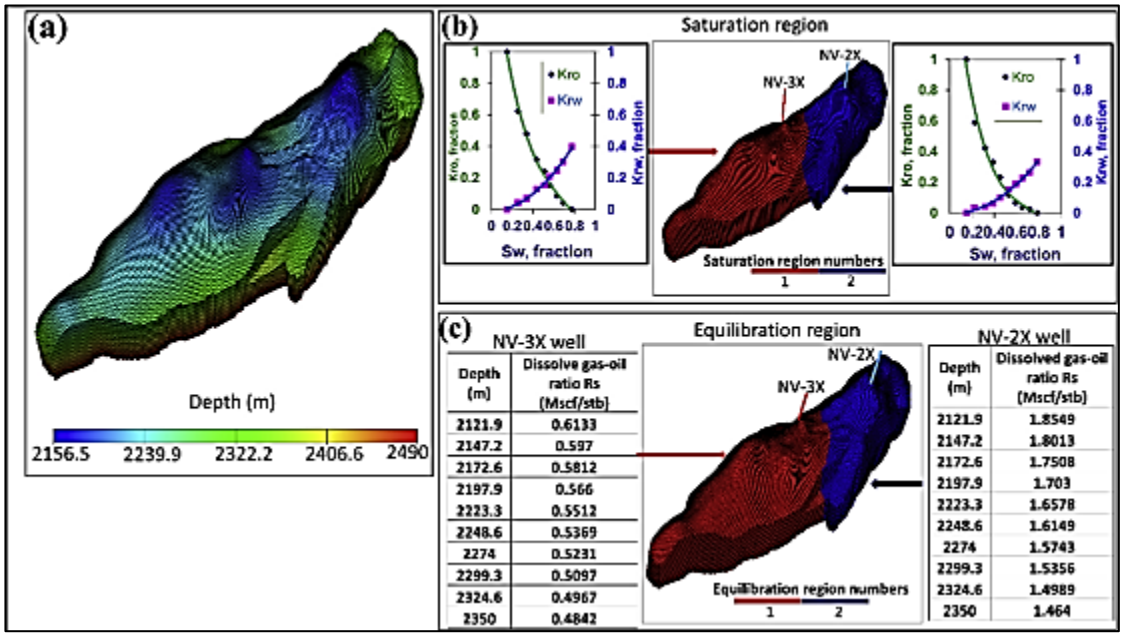

Figure 2.10 Preparation for DST Matching. (a) Reservoir Model of the Dynamic Simulation, (b) Saturation Region, and (c) Equilibration Region.

Source : Vo Thanh et al. (2019)

As the demand escalated, theoretical storage capacity was estimated using the following equation (Vo Thanh et al., 2020):

$$M_{CO2} = V_{pv} \times (1 - S_{wiir}) \times B \times \rho_{CO2} \times E \tag{2.7}$$

where M_{CO2} is the CO_2 storage mass (Mt), V_{pv} is the total pore volume (m^3), S_{wiir} is the irreducible water saturation (%), B is the formation volume factor (m^3/m^3), ρ_{CO2} is the CO_2 density (kg/m^3), and E is the capacity coefficient that integrates trap

heterogeneity. Rather than relying on area, porosity, and thickness, they proposed a new equation that incorporates pore volume. However, potential inaccuracies may arise if factors such as fluid properties, capillary pressure, relative permeability, trapping mechanisms, wellbore hydraulics, and geochemical reactions are not taken into account (Teletzke & Lu, 2013). These factors must be carefully considered to maximise CO_2 storage capacity and ensure its long-term stability.

2.11 Integration of the Mineralogical Properties in CO_2 Storage Evaluation

Conventionally, three-dimensional (3D) models were created for the estimation of facies distribution, petrophysical properties, and hydrocarbons initially in place (HCIIP) (Mahdi & Farman, 2023). Accurate identification of lithology, such as shaly sand, sandstone, and sandy shale in complex reservoirs, enhances the estimation of HCIIP and boosts oil production by targeting zones with the highest reservoir potential. A 3D modelling has developed over the last few decades to go beyond hydrocarbon use and is currently at the core of carbon capture and storage (CCS). They play a role in offering important information regarding the performance of the reservoirs, the trapping mechanisms, and the safety issues (Leng et al., 2024). This information shows a unique opportunity for effective CO_2 storage, fostering a sustainable ecosystem. Thus, an innovative solution is essential to improve the efficiency and accuracy of the CO_2 geological storage evaluation.

2.11.1 Importance of Mineralogical Properties on CO_2 Storage

Long-term storage of CO_2 in geological formations is governed by multiple trapping mechanisms, including structural trapping (Y. Wang et al., 2022), residual trapping (Baban et al., 2023), solubility trapping (Punnam et al., 2022), mineral trapping (Zhang et al., 2024), mineral trapping (Zhang et al., 2024), and adsorption trapping (Jia et al., 2024). These trapping mechanisms are working together to ensure the CO_2 is permanently absorbed by the solid minerals to form stable carbonate minerals (K. Kim et al., 2023). During this period of time, the structural trapping mechanism is the first to contribute to the CO_2 storage to ensure the carbon is free of leakage. After a thousand years, the mineral trapping mechanism is expected to begin its contribution to promise the safest CO_2 storage. Since the CO_2 mineralisation process induces the mineral

trapping mechanism, it needs to be taken into account when performing a 3D geological modelling.

During CO_2 mineralisation, the mineralogical characteristics are positively correlated with the adsorption capacity of the CO_2 geological storage (Dai et al., 2023; Jiang et al., 2023; I. Mohammed et al., 2024). Furthermore, they strongly regulate the reactive pathway (e.g. dissolution, precipitation), trapping efficiency, sealing integrity, and long-term permanence (I. Mohammed et al., 2024). CO_2 mineralisation involves the precipitation of $CaCO_3$ and dissolution of silicate by reacting injected CO_2 with these cations (Fe^{2+}, Ca^{2+}, and Mg^{2+}) that are found in minerals or formation brines. The rates are controlled by pH level, temperature, brine composition and reactive surface area (grain size, fracture density) (Postma et al., 2022).

The carbonate-rich formation may have limited CO_2 storage capacity, where dissolution of existing carbonate mineral could absorb acidity but not lead to net CO_2 locking unless new carbonate is precipitated by injected CO_2-derived carbon (Mouallem et al., 2023). On the other hand, clay-rich formations highly enhance the CO_2 storage capacity because of their unique mineralogical properties that influence caprock sealing, adsorption capacity, and reactive transport (Hamza, Hussein, Al-Marri, Mahmoud, & Shawabkeh, 2021). Varying clay mineral types also demonstrate different surface areas, and hence, varying CO_2 storage capacity. This underpins the studies to focus more on the mineralogy for CO_2 storage performance evaluation.

2.11.2 Novel Approach for CO_2 Storage Modelling Framework

To integrate mineralogy into CO_2 storage evaluation, the experts typically use various equipments: X-ray diffraction (bulk mineralogy), X-ray fluorescence/ICP (bulk chemistry), SEM/EDS (microtexture and secondary phases), BET (surface area), mercury intrusion and NMR (porosity/pore-size), micro-CT (pore network), and core flooding/autoclave kinetics tests. The increasing dependence on manual techniques for subsurface mineral characterisation and CO_2 storage site selection may not be relevant due to their cost and time-consuming nature. Therefore, the use of a machine learning predictive model in CO_2 storage evaluation may replace these techniques and determine the mineralogy efficiently. Aside from that, the current accessible mineralogical data, however, are limited to discontinuous locations only, whereas a holistic understanding of the whole subsurface formation is a prerequisite. As a result, a three-dimensional (3D)

visualisation cannot be ignored when getting a more global picture and making more informed decisions. This kind of integration will guarantee a stronger understanding of CO_2 storage potential, connecting mineralogy with field-scale reservoir performance.

Recent studies point out the modelling of the storage of CO_2 to emphasise (a) the mineralogical heterogeneity at the realistic scales of flow, (b) quantification of the uncertainties relating to the speed of the reaction, and (c) its area and correlate the geochemical and geomechanical processes to assess the potential effects of such uncertainties on the integrity of the caprock (P. Liu et al., 2019). These studies are conducted with the help of several simulators, such as PHREEQC, OpenGeoSys (OGS), HYTEC, ORCHESTRA, TOUGHREACT, eSTOMP, CrunchFlow, MIN3P, and PFLOTRAN. In 3D modelling, geological software, such as LeapFrog and Petrel, is typically used to generate accurate and comprehensive models for mineral exploration purposes (X. Cao et al., 2024). This includes capturing crucial aspects, such as topography, property distribution, structural features, and mineral deposits. Thus, the methodology might be similar to apply for visualising mineralogical composition in a 3D geological model.

Modern geological software enables the integration of multidimensional data, which includes porosity, permeability, facies, and petrophysical logs. By including the isotherm equation directly into the software, it is possible to determine the adsorption capacity of the subsurface model in every grid cell instead of only a small number of sampling points. This type of computational integration will convert mineralogical maps to continuous and three-dimensional (3D) spatial distributions of CO_2 adsorption capacity. Furthermore, these isotherm models also reliably simulate adsorption behaviour under specific pressure and temperature conditions. This is a better methodology than the traditional point-based methods that give a more accurate and more geographically informed evaluation of the CO_2 storage capacity of the subsurface. These models, in turn, enhance the strength of carbon sequestration analyses and help make more evidence-based, informed choices in CO_2 storage projects.

2.12 Summary

2.12.1 Principles of Carbon Capture and Storage (CCS)

CCS is a critical technology used to mitigate rising atmospheric CO_2 levels, which reached approximately 420 ppm in 2023. The CCS process generally involves four major stages: (i) capturing CO_2 emissions at the source, (ii) compressing the gas into a supercritical state, (iii) transporting the compressed CO_2 via pipelines or ships to designated storage locations, and (iv) injecting the CO_2 into deep geological formations for long-term and secure storage.

2.12.2 Geological Storage Criteria and Locations

Effective storage sites must be deeper than 850 metres to ensure CO_2 remains in a supercritical state and must be covered by impermeable caprock to prevent leakage. Common storage environments include deep saline aquifers (which have the highest capacity) and depleted hydrocarbon reservoirs. Depleted reservoirs are particularly appealing because their geology is well-characterized, and they offer existing infrastructure that can be repurposed.

2.12.3 CO_2 Trapping Mechanisms

Five main mechanisms facilitate the storage of CO_2 in geological formations:

1. **Structural Trapping**: CO_2 is held beneath a caprock by buoyancy forces.
2. **Residual Trapping**: CO_2 is trapped within rock pores by capillary forces.
3. **Solubility Trapping**: CO_2 dissolves into liquids within the formation.
4. **Mineral Trapping**: Geochemical reactions between CO_2 and minerals form stable new mineral phases over thousands of years.
5. **Adsorption Trapping**: CO_2 molecules bond to the surfaces of solid minerals.

2.12.4 Mineralogy and Adsorption

Adsorption is a surface-related phenomenon involving either physisorption, which is governed by weak Van der Waals interactions, or chemisorption, which involves stronger chemical bonding mechanisms. Clay minerals, particularly

montmorillonite, are highly favourable for CO_2 adsorption due to their large specific surface areas and high density of adsorption sites.

The adsorption capacity of geological formations is influenced by both internal and external factors. Internal factors include pore size distribution, surface area, and the presence of functional groups such as hydroxyl (–OH) and carboxyl (–COOH) groups. Micropores and transitional pores are generally more effective for gas adsorption due to their enhanced surface interactions. External factors primarily include temperature and pressure conditions. Elevated pressures generally increase CO_2 adsorption capacity until adsorption equilibrium is reached, whereas increasing temperature tends to reduce adsorption efficiency due to enhanced molecular mobility.

2.12.5 Identification and Modelling Techniques

Accurate characterisation of mineralogical composition is essential for evaluating CO_2 storage potential; however, conventional laboratory analyses are often time-consuming and costly. Traditional approaches include laboratory-based techniques such as X-ray diffraction (XRD) and X-ray fluorescence (XRF), as well as manual interpretation of conventional well logs including gamma ray, density, and sonic logs.

Recently, artificial intelligence (AI) and machine learning (ML) techniques have gained increasing attention for automated mineralogical prediction and reservoir characterisation. Algorithms such as Extreme Gradient Boosting (XGBoost) and Random Forest (RF) have demonstrated strong predictive capability due to their ability to model complex non-linear relationships within geological datasets and efficiently handle high-dimensional structured data.

2.12.6 Adsorption Isotherm Models

Adsorption isotherm models are widely used to estimate the CO_2 storage capacity of geological formations. Among the available models, the Dubinin–Astakhov (D-A) model is considered one of the most robust and reliable approaches because it accounts for pore size distribution and surface heterogeneity. In addition, the D-A model demonstrates strong applicability under both subcritical and supercritical CO_2 conditions, making it particularly suitable for geological storage studies conducted under reservoir conditions.

2.12.7 Integrated 3D Reservoir Modelling

Modern reservoir evaluation increasingly relies on three-dimensional (3D) reservoir modelling to visualise subsurface heterogeneity and estimate CO_2 storage capacity more accurately. A novel approach involves integrating mineralogical data and adsorption isotherm equations directly into 3D reservoir models. This integration enables the determination of adsorption capacity for each individual grid cell within the reservoir model, thereby providing a more spatially distributed and geologically representative assessment of total CO_2 storage potential.

CHAPTER 3
RESEARCH METHODOLOGY

3.1 Introduction

This chapter outlines the research methodology employed to achieve the stated research objectives. Advanced data analysis, modelling and simulation were conducted using a combination of specialised software applications, including Techlog and Petrel, together with Python programming. Figure 3.1 provides a schematic overview of the overall research workflow. This workflow starts by conducting a comprehensive literature review to synthesise existing knowledge, methodologies, and findings related to the study. Based on the review, critical research gaps are identified, highlighting aspects that remain insufficiently explored in previous studies. These gaps inform a clear problem statement and research objectives, which provide the scope of the study.

The methodology is designed to translate the research objectives into an actionable research strategy. Specifically, relevant data was acquired from available sources. The next step is to ensure that the study is underpinned by systematic data collection and rigorous analysis. This step involves data analytics, including cleaning, manipulating, analysing, and visualising the data.

Subsequently, a machine learning (ML) model was developed and trained to predict mineral composition using the conventional well log data. Meanwhile, the mineral composition used for ML model development was estimated using the simultaneous equation method. The ML model development phase encompassed data preprocessing, model training and testing, implementation, and performance evaluation. The resulting mineral composition predictions were then integrated into three-dimensional (3D) facies and mineralogical modelling, which was further extended to develop a three-dimensional (3D) adsorption capacity model. This step elucidates the relationship between mineralogical composition and CO_2 adsorption capacity.Finally, the developed models were employed to simulate CO_2 adsorption performance under varying pressure and temperature conditions. The results were subsequently analysed to draw conclusions and provide recommendations for future applications.

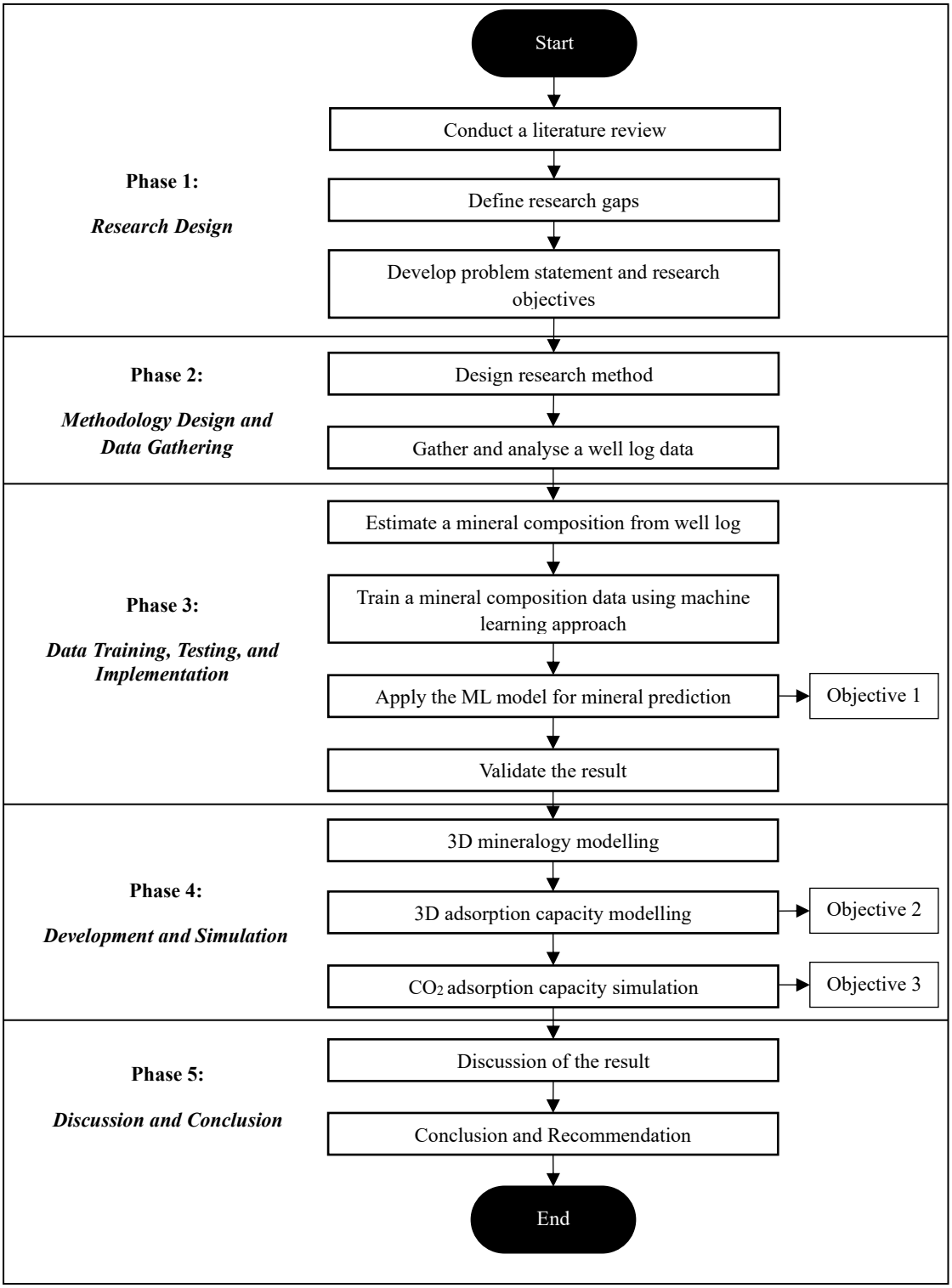

Figure 3.1 Flowchart of the Research.

3.2 Study Area

3.2.1 Geological settings of Viking Graben

The first datasets utilised in this study were obtained from the South Viking Graben and North Viking Graben, which form part of the North Sea Rift System. The Viking Graben represents one of the major rift arms of the trilete Jurassic North Sea Rift System, together with the Central Graben and Moray Firth Basin (Badejo et al., 2021). Geologically, the basin is characterised as a NNE–SSW trending aborted continental rift that was primarily initiated during the Late Jurassic period. The tectonic evolution of the Viking Graben was strongly influenced by Middle Jurassic thermal doming and regional east–west extensional tectonics, followed by Late Jurassic to Early Cretaceous rifting, which produced extensive rotated fault blocks and half-graben structures (Deng et al., 2025; Underhill & Richardson, 2022; L. Zhao et al., 2026).

The North Viking Graben is characterised by en echelon half-grabens, rotated fault blocks, and major normal fault systems formed during multiple extensional tectonic events (L. Zhao et al., 2026). The basin contains Jurassic syn-rift deposits overlain by younger Cretaceous–Cenozoic post-rift sedimentary sequences. Important geological units within the North Viking Graben include the Humber Group source rocks and the Brent Group reservoir sandstones (Da Silveira et al., 2024).

The South Viking Graben is structurally connected through regional rift-related fault systems. The basin is dominated by rotated half-grabens and fault-controlled subsidence associated with Triassic and Jurassic extensional tectonics (Sordi et al., 2025, 2026). The geological evolution of the South Viking Graben was strongly influenced by thermal doming, Late Jurassic rifting, and subsequent post-rift subsidence, resulting in complex reservoir architectures and heterogeneous lithofacies distributions (Deng et al., 2025; Sordi et al., 2025).

3.2.2 Geological settings of Malay Basin

The second dataset in this study is originated from Malay Basin. Generally, the Malay Basin is a major northwest–southeast (NW–SE) trending Cenozoic extensional basin located offshore Peninsular Malaysia (Mahmud & Sautter, 2022). The tectonic evolution of the Malay Basin can be broadly divided into three major phases. The first phase involved extensional rifting during the Late Eocene to Oligocene (Maerten et al.,

2019). This tectonic activity resulted in the development of graben–horst structures, lacustrine depocentres, and the deposition of the oldest syn-rift sedimentary sequences. The second phase was characterised by regional thermal subsidence during the Early to Middle Miocene (de Jonge-Anderson et al., 2025). This period facilitated widespread sediment accumulation within fluvial-deltaic, coastal plain, and shallow-marine depositional environments. The final phase involved compressional inversion during the Middle to Late Miocene (de Jonge-Anderson et al., 2025; Maerten et al., 2019), which was associated with regional stress reorganisation following the cessation of seafloor spreading in the South China Sea. This tectonic event resulted in the formation of inversion anticlines, structural closures, unconformities, and the reactivation of earlier extensional fault systems.

The sedimentary succession of the Malay Basin is traditionally subdivided into Groups A to M (Babikir et al., 2022), arranged from the youngest to the oldest units. Groups M and L represent syn-rift deposits dominated by fluvial and lacustrine sedimentary environments (Mahmud & Sautter, 2022). Groups K and J comprise transitional post-rift deposits characterised by lacustrine to marginal-marine settings (Morley et al., 2021). The younger Groups I to A consist predominantly of Neogene paralic, coastal plain, deltaic, and shallow-marine deposits, including tidally influenced fluvial channel systems (Manshor et al., 2022). These sedimentary sequences record the progressive evolution of the basin from continental rift environments to extensive shallow-marine depositional systems.

Structurally, the Malay Basin originated as an aulacogen developed on the Malay Dome (Tjia, 2010). The basin architecture is characterised by a series of north–south (N–S) trending en-echelon grabens and structural ridges formed during the extensional rifting phase (Mansor et al., 2014). These structures were subsequently modified by west–east (W–E) oriented compressional inversion during the Miocene, resulting in the development of inversion folds and structural closures. In certain areas, the basin is underlain by pre-Tertiary basement rocks, including Triassic limestone formations, which locally influence reservoir development and structural configuration (Fontaine et al., 1990).

3.3 Data Preparation

The purpose of the study is (a) to develop a machine learning model for predicting mineralogical composition logs from conventional well log data, (b) to construct and visualise a three-dimensional (3D) geological reservoir model that integrates the spatial distribution of predicted minerals relevant to carbon adsorption capacity, and (c) to simulate and evaluate the impact of mineral-specific carbon adsorption capacities on CO_2 storage performance within the 3D model under varying pressure and temperature conditions. Therefore, data preprocessing is required to ensure that the dataset is consistent, coherent, and valid. This process is described in the subsequent sections, specifically data acquisition and data cleaning.

3.3.1 Data Acquisition

There are two well logging datasets in this study that were retrieved from open-source and an institution. The first dataset used, namely the Force dataset, is obtained from a website (https://github.com/bolgebrygg/Force-2020-Machine-Learning-competition). This website provides the result, code, and input data used by the participants in the machine learning competition 2020. The Force dataset consists of approximately one million rows of well log data originally located at Viking Graben. It includes a variety of conventional well log measurements, such as gamma ray (GR), resistivity, bulk density (RHOB), neutron porosity (NPHI), photoelectric factor (PEF), and compressional sonic travel time (DTC) logs.

In this study, well log data from the Asgard Formation were extracted from the Force dataset and utilised as the testing dataset for the trained machine learning-based mineral predictive model. The Asgard Formation dataset was selected to evaluate the predictive performance of the developed model within the same geological setting as the training dataset, thereby allowing assessment of the model consistency and prediction reliability under similar subsurface conditions.

The second dataset consists of approximately 10,000 rows of well log data obtained from a separate basin, specifically the X Field, and was acquired from an institutional source. In general, the dataset originates from the Malay Basin. Similar to the FORCE dataset, the X Field dataset contains several conventional well log parameters, including GR, RHOB, NPHI, resistivity, PEF, and DTC logs, enabling

comparable petrophysical interpretation and mineralogical prediction analysis between the two datasets.

Apart from the Asgard Formation dataset, the X Field dataset was utilised as a blind testing dataset to evaluate the applicability, robustness, and generalisation capability of the developed predictive model under different geological settings. The utilisation of datasets from distinct basins enables the assessment of the model performance across varying lithological, depositional, and reservoir conditions. However, the dataset is provided solely for educational and research purposes and remains subject to confidentiality restrictions; therefore, it is not available for external distribution or public sharing.

3.3.2 Data Cleaning

A high-quality ML model depends on a rigorous data-cleaning process to ensure the dataset is properly interpretable by the algorithm. Two common types of errors must be addressed: (i) missing values, where entries are absent or left blank, and (ii) outliers, which include incorrect or unrealistic data and measurement errors. The interquartile range (IQR) was used to determine outliers in this study. The missing values were eliminated with the help of Python, and the outliers were eliminated manually in Excel.

Figure 3.2a shows the distribution of the data values of four different well logs from the Force dataset. After the data cleaning, there are approximately 640,000 well log data points from 56 wells out of 118 wells, which are then utilised for ML model training. The wider section indicates that more data points fall within that range. The white central line represents the median. The black box in the middle of the violin shape represents the interquartile range (IQR), with the box edges showing the first and third quartiles. The shape of the violin demonstrates the distribution of the data.

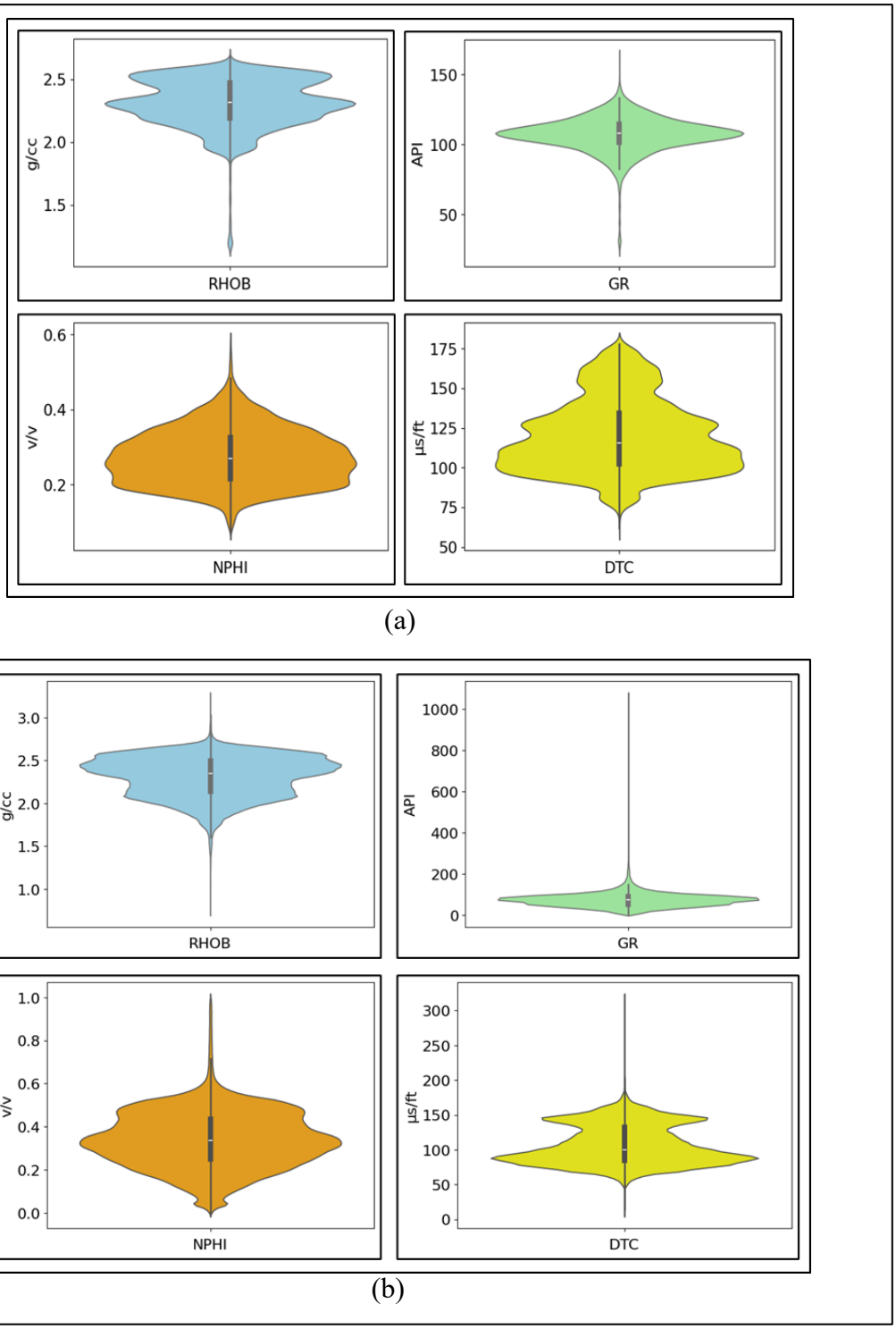

Figure 3.2 Violin Plot of the Well Log Data Distribution. (a) Force Dataset; (b) X Field Dataset.

Figure 3.2b presents the violin plot of four different well logs from the X field dataset, showing approximately 10000 well log data values. The machine learning model is developed using this dataset to evaluate its predictive performance. In addition, the same data will serve as input for the development of a three-dimensional (3D) model.

3.4 Computational Method for Mineral Composition Estimation

Well log and core data are important information for mineral composition identification and are basically interpreted by using advanced software or a laboratory analysis. Nonetheless, the limited availability of well log data and the absence of core data necessitate an alternative approach based on mathematical modelling. This mathematical approach is flexible, as it allows the number of variables and underlying patterns to be adjusted accordingly.

A step-by-step procedure for estimating mineral composition is illustrated in Figure 3.3. The workflow begins with the derivation of a mathematical formulation from the literature, incorporating conventional well log inputs such as RHOB, NPHI, and DTC logs. The subsequent step entails designing an algorithm to perform the calculation. The simultaneous method, which is one of the iterative techniques, is used to handle a complex relationship in an equation system. The results are then subjected to a validation process using well log interpretation and cross-plot analysis to ensure the reliability of the estimated mineral composition data.

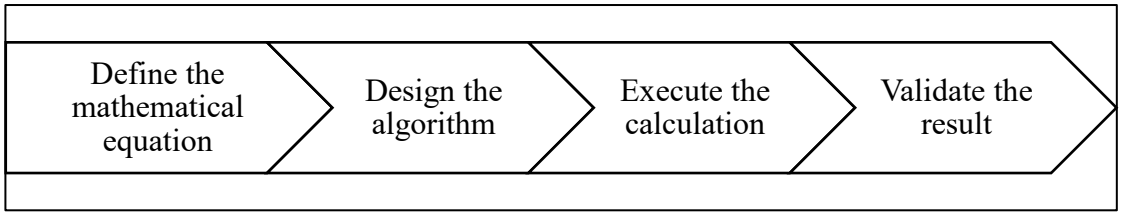

Figure 3.3 Flowchart for Mineral Composition Estimation.

3.4.1 Mathematical Equation Explanation

Based on the literature review, the method to calculate mineral composition was first expressed by Schlumberger (1989). The technique employs a system of simultaneous equations to estimate mineral fractions, where each fraction is multiplied by the theoretical response of a specific log until the computed values match the actual log measurements. A similar implementation, known as the mineral solver, is available in the Techlog software. In this study, a modified formulation was developed based on the available well log responses and the target mineral components.

$$\rho_b = \phi \cdot \rho_f + (1-\phi)(Q \cdot \rho_Q + \ldots + K \cdot \rho_K + M \cdot \rho_M + I \cdot \rho_I + Ch \cdot \rho_{Ch}) \quad (3.8)$$

$$\phi_N = \phi \cdot \phi_f + (1-\phi)(Q \cdot \phi_Q + \ldots + K \cdot \phi_K + M \cdot \phi_M + I \cdot \phi_I + Ch \cdot \phi_{Ch}) \quad (3.9)$$

$$t = \phi \cdot t_f + (1-\phi)(Q \cdot t_Q + \ldots + K \cdot t_K + M \cdot t_M + I \cdot t_I + Ch \cdot t_{Ch}) \quad (3.10)$$

$$1 = Q + C + D + K + M + I + Ch \quad (3.11)$$

Where LHS and RHS represent the actual well log response and the theoretical well log response of the RHOB, NPHI, and DTC logs, respectively. The additional variables to the previous mathematical equation are K, M, I, and Ch, which represents kaolinite, montmorillonite, illite, and chlorite, respectively. The values of ρ_f, ϕ_f, and t_f are constant, which are 1.00 g/cm^3, 1 v/v, 189 µs/ft, respectively, as the assumption for drilling fluid type is the freshwater mud. Table 3.1 provides the theoretical range values of the well log responses for seven minerals.

Table 3.1
RHOB, PEF, NPHI, GR, and DTC Readings of the Minerals.

Minerals	**RHOB (g/cm^3)**	**PEF (b/e)**	**ϕ_{CNL} (p.u)**	**GR (API)**	**DTC (µs/ft)**
Dolomite	2.85 (2.85-2.88)	3.14	1		44
Calcite	2.71	5.08	0		49
Quartz	2.65 (2.64-2.66)	1.81	-2		56
Chlorite	2.76 (2.6-3.22)	6.3	52	180-250	80
Illite	2.52 (2.52-3.0)	3.5	30	250-300	90
Kaolinite	2.41 (2.4-2.69)	1.83	37	80-130	80
Montmorillonite	2.12 (2.0-3.0)	2.04	60	150-200	120

Sources: Ellis & Singer (2007), Schlumberger (2009), Rider & Kennedy (2011), Bigelow & Inc (2002).

3.4.2 Algorithm Design

The simultaneous method is an iterative technique that is widely employed to find the roots of complex polynomials (Pavkov et al., 2023; Shams et al., 2024). Hence, it is intended to solve the complex relationships in the linear and non-linear equation system. For mineral composition identification, the iterative technique requires an initial model, which serves as an initial estimate of the mineral fractions. The algorithm

will then optimise these values one step at a time by multiplying with the theoretical response of a specific log until the computed values match the actual log measurements. Figure 3.4 presents the systematic algorithm design that applies the simultaneous method to solve for mineral composition.

The calculations were carried out in Python using libraries such as Pandas, NumPy, and SciPy.optimize. The algorithm formulated a system of four simultaneous equations with the corresponding constraints. The least squares approach was employed to define an objective function that minimises the discrepancy between theoretical responses and measured well log data (M. Hussain et al., 2022).

The mineral solver was solved using scipy.optimise.minimise function, which optimises the system of mineral fractions derived from the objective function. This process employs an iterative trial-and-error approach in which candidate solutions are systematically adjusted based on the measured well log responses until an optimal set of mineral fractions is achieved. Prior to execution, the initial values for all mineral fractions were set to 0.1 because XRD data were unavailable in this study to inform the initialisation. The optimisation was further constrained by the following conditions: (i) the sum of all mineral fractions equals one, and (ii) each mineral fraction is non-negative.

The subsequent step involves estimating the mineral fractions. At each depth interval, RHOB, NPHI, and DTC values were extracted from the dataset and used as input parameters. The mineral solver was then executed to determine the optimal set of mineral fractions that most accurately reproduces the measured well log responses. Eventually, the mineral solver will generate seven mineral fractions across depths, and these results will be stored in the dataset for further analysis.

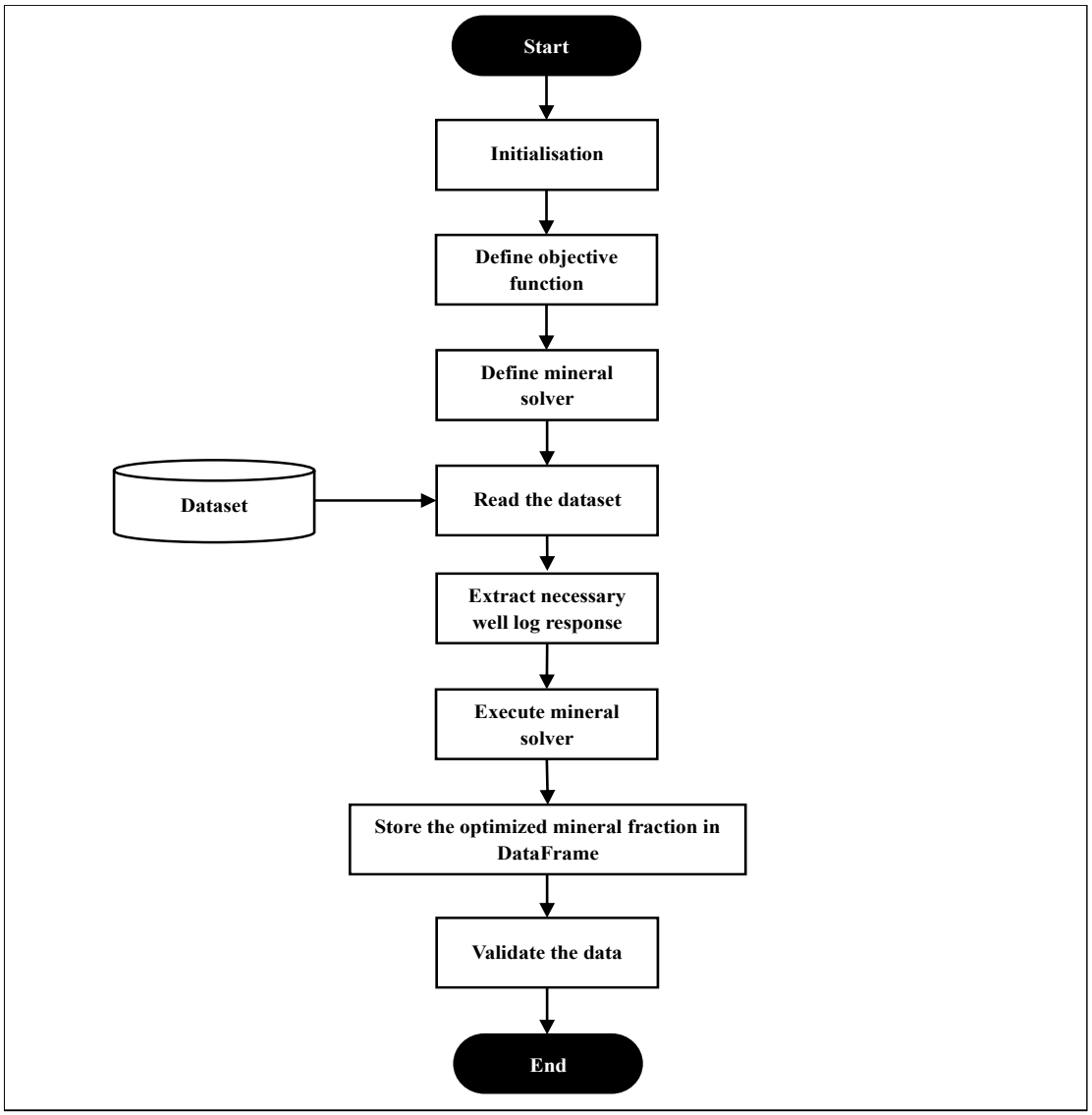

Figure 3.4 Algorithm Design for Mineral Composition Estimation.

3.5 Validation Technique for Mineral Composition Estimation

The simultaneous equation method used to estimate mineral composition is inherently constrained by the presence of multiple solutions, which in some cases may be non-unique or even infinite. As the unknown mineral variables increase, the system becomes more difficult to find an exact answer, leading to non-unique solutions that depend heavily on user-defined assumptions. To overcome this challenge, the estimated mineral fractions were validated in two ways: (i) by comparing them with well log responses and (ii) by cross-plot analysis. Figure 3.5 is an example that utilises various cross-plots alongside the corresponding well log responses for lithology identification. The markers of the cross-plots have been traced following the specific colours on the

composite well log correlation. This colour coding provides a quick-look qualitative interpretation of the corresponding well log responses.

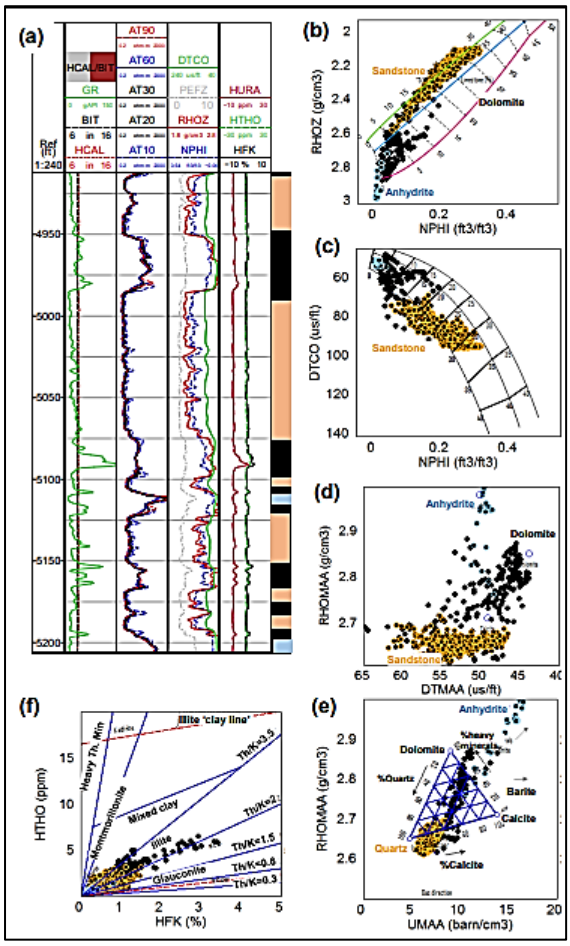

Figure 3.5 Well Log Cross-Plot Analysis. (a) Well log Correlation; (b) NPHI-RHOB Cross-Plot; (c) DTCO-NPHI Cross-Plot; (d) RHOMAA-DTMAA Cross-Plot; (e) RHOMAA-UMAA Cross-Plot; (f) Thorirum–Potassium Cross-Plot.

Source : Pothana et al. (2024)

Based on the available well logs in this study, only the NPHI-RHOB cross-plot was used. The NPHI–RHOB cross-plot was selected as the primary tool for lithological interpretation. This cross-plot is widely used to differentiate major lithology groups, such as sandstone, calcite, and dolomite. Its application ensured that the estimated mineral fractions were consistent with geologically plausible mineral groupings. To support this validation, conventional well logs, including GR, RHOB, NPHI, DTC, resistivity, and facies logs, are displayed alongside the estimated mineral composition on a well log correlation template, together with the NPHI–RHOB cross-plot. Two datasets are considered for validation: the Force dataset and the X field dataset. For the

Force dataset, validation is conducted using data from a single formation, namely the Asgard Formation.

3.6 Correlation Analysis Between Well Logs and Estimated Mineral Composition Using Heatmap

The numerical and visual explanation plays a pivotal role in measuring the contribution of the input parameters (RHOB, NPHI, and DTC logs) to the estimated mineral composition for the simultaneous equation method. Woelk et al. (2025) suggested heatmap highlights the significant contribution of the areas that are influential for the classification. Heatmap analysis, as depicted in Figure 3.6, provides a robust statistical framework for identifying both strong positive and negative correlations. Specifically, the colour intensity within the heatmap signifies the strength and direction of these correlations. A strong positive correlation indicates that as one variable increases, the other variable also tends to increase, while a strong negative correlation suggests an inverse relationship where an increase in one variable corresponds to a decrease in the other. Values closer to zero, conversely, denote a weak or negligible linear relationship between the analysed parameters, indicating their relative independence.

The heatmap shown in the figure demonstrate the moderate positive relationship between core porosity and permeability, indicating that permeability generally increases with increasing porosity. This trend is expected because larger pore volumes commonly provide enhanced fluid flow pathways within the reservoir system.

The well log dataset also exhibits several important interrelationships. DTC and NPHI display a very strong positive correlation (0.92), indicating that formations with higher porosity generally produce slower compressional wave velocities due to reduced rock matrix rigidity. In contrast, RHOB shows strong negative correlations with DTC (−0.70) and NPHI (−0.83), reflecting the typical inverse relationship between density and porosity observed in sedimentary formations.

Furthermore, gamma ray (GR) logs exhibit moderate positive correlations with DTC (0.48), DTshear (0.43), and the photoelectric factor (PEF) (0.63). These relationships may indicate that shale-rich intervals, which commonly contain significant clay mineral content, are associated with slower acoustic wave velocities and distinct photoelectric responses due to their mineralogical composition and elevated bound

water content. Therefore, these correlations provide a meaningful relationship between porosity, permeability, and well log responses, which supports the reliability of these variables for reservoir characterisation and machine learning-based development.

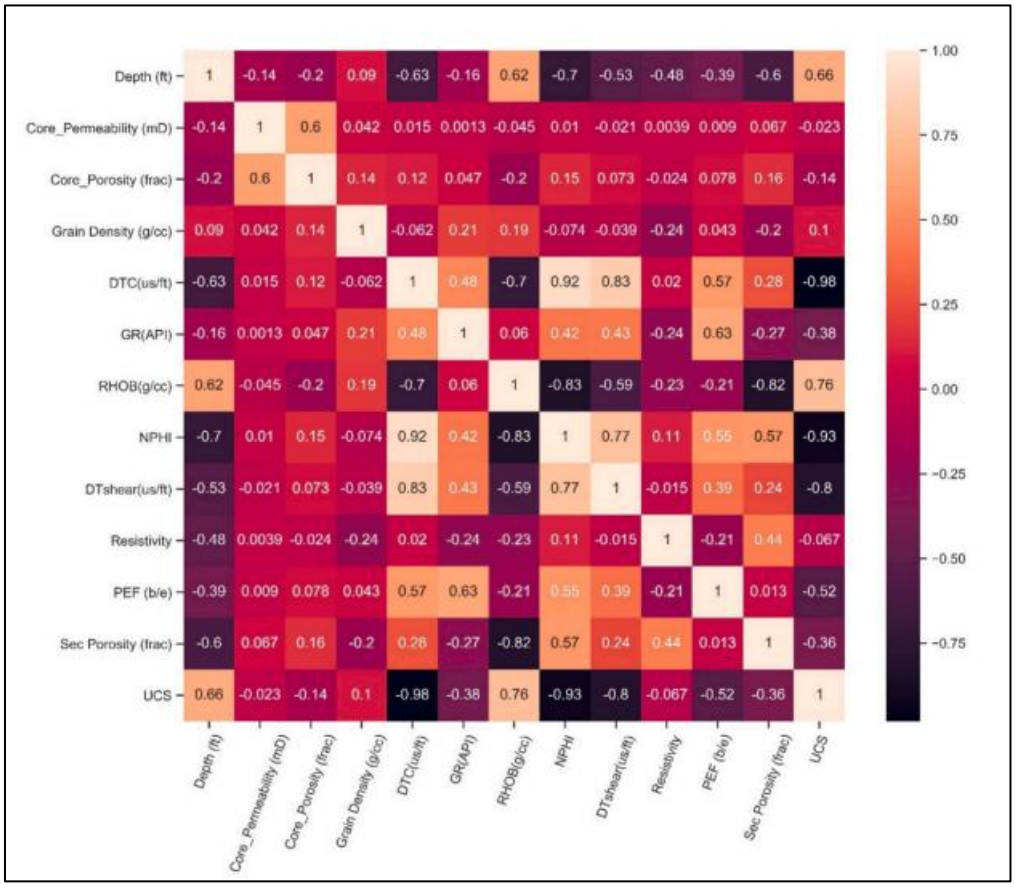

Figure 3.6 Heatmap of the Correlation amongst Well Log Dataset, Porosity, and Permeability.

Source : Sen et al. (2021)

3.7 Machine Learning Algorithm Design for Mineral Composition Prediction

This section outlines the overall research workflow and supports the development of the machine learning model. The machine learning algorithm processes the data to identify underlying patterns and trends that inform more effective decision-making. Figure 3.7 depicts the algorithm design to develop an ML mineral predictive model using the Force dataset. This study applies Extreme Gradient Boosting (XGBoost), which incorporates an advanced gradient boosting decision tree algorithm that is specifically designed for tasks such as classification and regression.

The machine learning algorithm was developed in Python using the NumPy, Pandas, XGBoost, and Scikit learn libraries. Well log measurements were used as the input variables, while the estimated mineral fraction served as the target variable. The Force dataset was divided into training and testing subsets using a 95:5 ratio, selected based on the large size of the dataset. In this study, 5% testing subset contains more than 30,000 data points, which is sufficient to provide a reliable estimate of model performance. To minimise the risk of overfitting, appropriate model fitting strategies and hyperparameter tuning were conducted.

The XGBoost regressor was used to model the non-linear relationships between mineral composition and well log data. The example of hyperparameters that are typically tested were n_estimators, learning_rate, max_depth, subsample, and colsample_by_tree. Initial values of n_estimators, learning_rate, and max_depth were set to 100,0.1, and 3, respectively. Hyperparameter tuning was implemented using the GridSearchCV technique to identify the optimal parameter combination. Model fitting and selection were guided by the mean squared error (MSE) criterion. The lowest MSE corresponds to the optimal hyperparameter combination. The machine learning model was then developed using this optimal configuration to generate predictions. Finally, model performance was evaluated using multiple metrics, including the R^2 score, mean absolute error (MAE), and root mean square error (RMSE).

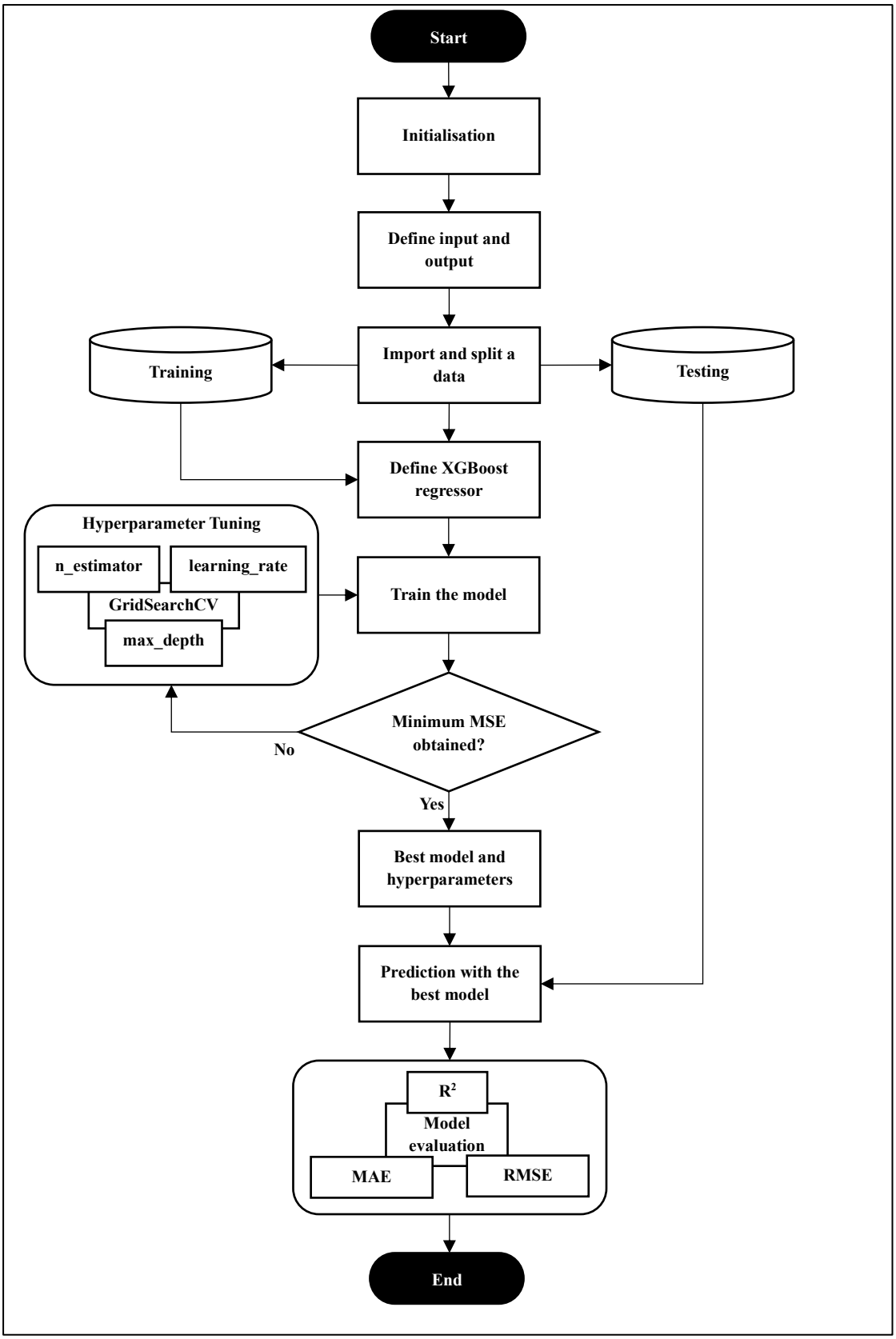

Figure 3.7 Algorithm Design for First Research Objective in Flow Diagram.

3.7.1 Initialisation

The XGBoost architecture was illustrated in Figure 3.8. For the first tree, a simple initial prediction is generated and fitted to the training dataset. The model then computes the residuals, defined as the differences between the predicted and actual values. A new decision tree is subsequently constructed and trained using these residuals. This iterative process aims to progressively minimise the residual errors propagated from the preceding tree. This process is repeated until the predefined stopping criteria are satisfied. The procedure produces an ensemble of tree-based models, each contributing to the overall prediction. Finally, the individual predictions from all trees are aggregated to obtain the final prediction output.

The implementation of the XGBoost model in this study was carried out using the Python programming language due to its extensive machine learning libraries and computational efficiency in handling large-scale datasets. The model development and training processes were primarily conducted using the XGBoost library together with supporting libraries such as Pandas, NumPy, and Scikit-learn for data preprocessing, feature engineering, model training, and performance evaluation.

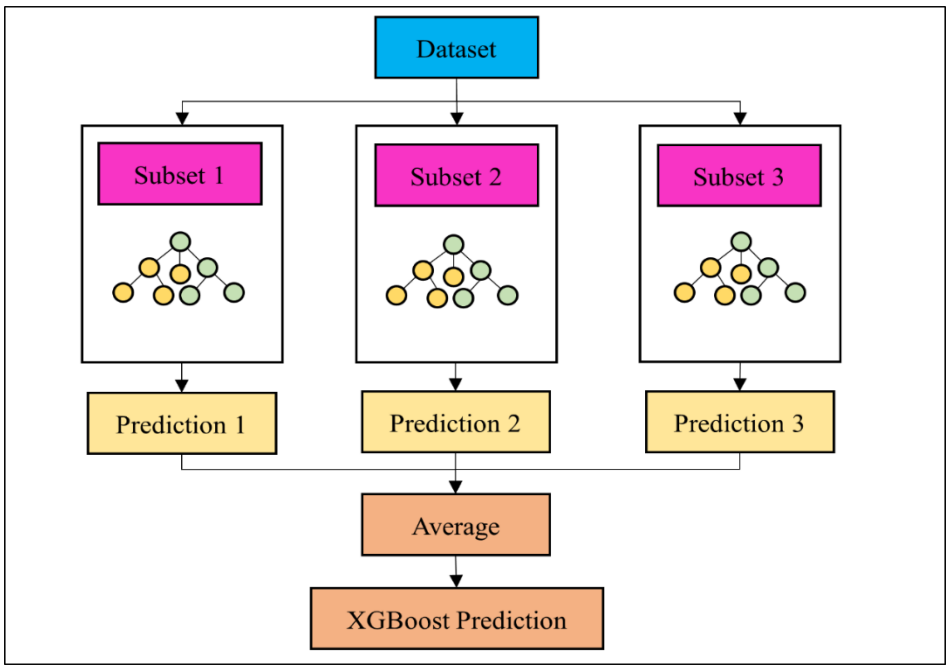

Figure 3.8 A General Architecture of the XGBoost.

Source : Amjad et al. (2022)

3.7.2 Model Training

In the subsequent step, the pre-processed dataset is prepared. The Force dataset of 640,000 well log data points from 56 wells is then imported, with variables clearly designated as inputs and targets. The target variables represent the dependent variables, whereas the input variables correspond to the independent variables. Figure 3.9 depicts three input variables and seven target variables, representing the well log responses and mineral composition, respectively. The dataset is then divided into two subsets, namely the training dataset and the testing dataset. The data splitting ratio is determined based on the size of the dataset. For a large dataset, the training and testing sets are allocated in a ratio of 95:5. In this study, the 5% testing dataset contains more than 30,000 data points, which is sufficient to provide a reliable and precise evaluation of the machine learning model's performance.

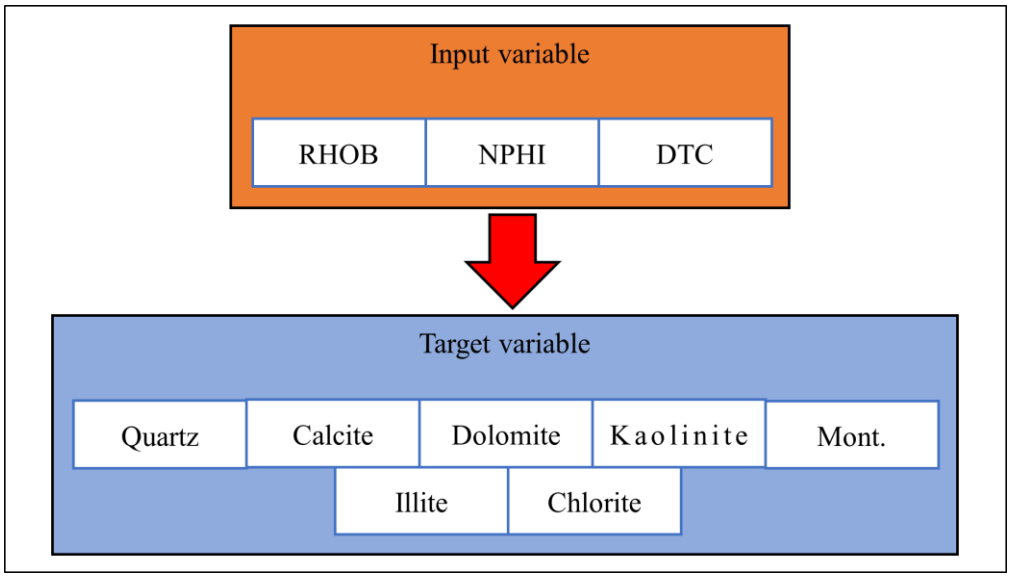

Figure 3.9 Input and Target Variables.

XGBoost Regressor is defined with initial parameters. The parameters are described as follows:

- objective: represents the type of learning task to perform.
- n_estimators: represents the number of decision trees to be built in the ensemble model.
- learning_rate: represents the rate of each new tree added to the ensemble model.

- max_depth: represents the maximum depth of a tree that grows in the ensemble model.
- subsample: controls the fraction of the training data to be a random sample for each tree.
- colsample_bytree: controls the fraction of the columns to be random samples for each tree.

The initial values for n_estimators, learning_rate, and max_depth are 100, 0.1, and 3, respectively. Basically, a lower learning rate prevents the output data from overfitting issues. Increasing the n_estimators and max_depth values tends to make a model more complex and potentially overfit the data. These parameters are applied during model training to generate the corresponding prediction values from the dataset.

3.7.3 Model Evaluation and Hyperparameter Tuning

The model fitting procedure is aimed at generating the best-suited parameters for a model and preventing the risk of overfitting. This procedure is conducted before the model is applied to the testing dataset. The model fitting procedure implements the mean squared error (MSE) to calculate the average squared difference between the predicted and actual values, as expressed in the equation below:

$$MSE = \frac{\sum_{i=1}^{n}(y_i - \hat{y}_i)^2}{n} \ldots \quad (3.12)$$

The hyperparameter tuning is configured and applied in the algorithm using the GridSearchCV technique to determine the optimal combination, with cross-validation set to 5. Table 3.2 lists a set of values for each parameter. This set of values was selected to satisfy the following criteria: (a) balanced model complexity; (b) stable gradient boosting behaviour; and (c) computational efficiency. Applying GridSearchCV helps to prevent the model from overfitting and ensures the model is manageable for multi-mineral prediction. The optimal hyperparameter combination yields the lowest MSE. These optimal hyperparameters were then used to retrain the model to achieve robust predictive accuracy. Finally, the trained XGBoost model was applied to the dataset to

predict mineral composition, and its performance was evaluated using standard prediction metrics.

Table 3.2
List of the XGBoost Hyperparameter Values.

Parameter	Values
n_estimators	50, 100, 150
learning_rate	0.05, 0.1, 0.15
max_depth	3, 4, 5, 6
subsample	0.8
colsample_bytree	1

3.7.4 XGBoost Performance Evaluation Technique

To systematically assess the accuracy and reliability of the trained XGBoost model, several performance metrics were employed using the optimised hyperparameters. Model evaluation was conducted on two datasets. First, the trained model was evaluated using the Force testing dataset, which consists of approximately 30,000 rows of well log data, as previously described. Subsequently, the X Field dataset, comprising approximately 10,000 rows of well log data, was utilised as a blind test dataset to assess the model's generalisability and robustness across different geological basin settings. The primary performance evaluation metric was the coefficient of determination (R^2), which quantifies the proportion of variance in the target variables that is explained by the model. A high R^2 indicates a greater degree of conformity between the predicted and actual values, resulting in a strong model precision. The expression of R^2 is shown below:

$$R^2 = 1 - \frac{\sum_{i=1}^{n}(y_i - \hat{y}_i)^2}{\sum_{i=1}^{n}(y_i - \bar{y})^2} \tag{3.13}$$

Where n is the number of samples, y_i is the actual value of minerals (%), $\hat{y}_i$ is the predicted value of minerals (%), and $\bar{y}$ is the mean of the actual value of minerals (%). However, model performance should not be assessed using a single indicator, as this may obscure errors in the mean estimation and the overall prediction scale.

Thus, absolute error measures were also included, including the mean absolute error (MAE) and the root mean square error (RMSE). MAE measures the mean size of absolute errors, and RMSE measures the square root of the mean squared errors between predictions and actual values. Both measures give information on the magnitude of the prediction errors. The lower the MAE and RMSE, the better the model accuracy and the less the difference between the predicted and actual mineral compositions. The interpretation of MAE and RMSE values is summarised as follows:

$$MAE = \frac{1}{n}\sum_{i=1}^{n}|y_i - \hat{y}_i| \ldots \quad (3.14)$$

$$RMSE = \sqrt{\frac{\sum_{i=1}^{n}(y_i - \hat{y}_i)^2}{n}} \ldots \quad (3.15)$$

The other realistic validation method is the comparison of the predicted and actual mineral fractions using the log interpretation method. This comparison provides an overall assessment of the trained XGBoost model's predictive accuracy and identifies the input variables that contribute to its weaker performance.

3.8 3D Static Reservoir Modelling Approach

In this study, the three-dimensional (3D) static reservoir modelling workflow used to estimate CO_2 adsorption capacity is illustrated in Figure 3.10. The workflow comprises of: (i) preparation of input data for structural and property modelling, (ii) structural modelling, including horizons, zones, layering, and fault representation, (iii) distribution of two-dimensional (2D) mineral log data into a 3D grid model, and (iv) development of the 3D adsorption capacity model, integrating the CO_2 adsorption capacity estimated using the property calculator.

The modelling workflow begins with the preparation of input data, including well log data, well tops, and well deviation information. These datasets are occasionally digitised into two-dimensional (2D) maps to generate surfaces that represent the general geological characteristics of the formation. Structural modelling is then performed in Petrel, starting with the definition of the fault system, followed by the application of pillar gridding to construct a three-dimensional (3D) grid. Horizons, zones, layering,

and faults are subsequently incorporated in a systematic manner to establish a robust structural framework for subsequent property modelling.

The two-dimensional mineral log data predicted by the trained XGBoost model are then integrated into the 3D structural grid during the property modelling stage. Two models are generated: (i) a 3D mineralogical model, which distributes mineral fractions throughout the reservoir, and (ii) a 3D facies model, in which upscaled mineralogical data are assigned to facies. These models are subsequently used to derive mineralogical properties for estimating CO_2 adsorption capacity. The adsorption capacity is calculated using the property calculator and distributed directly across the 3D grid. Finally, simulation and analysis are conducted to evaluate the behaviour of CO_2 adsorption capacity under varying pressure and temperature conditions, yielding a spatially resolved assessment of the formation's CO_2 storage potential.

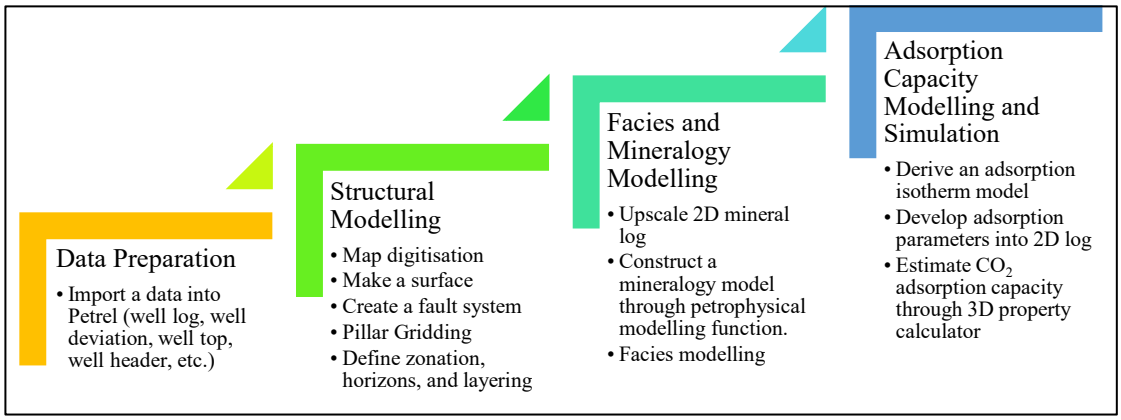

Figure 3.10 Flowchart for Second Research Objective.

3.8.1 Data Preparation

The dataset used in this study comprises deviation files (.prn), well tops (.txt), well headers (.dat), and well type files (.prn). Well log data are available from three wells: X-1, X-2ST1, and X-2. The available logs (RHOB, NPHI, DTC, and GR logs), are utilised for well log interpretation. However, mineral composition data are available only for well X-1, as DTC logs are absent in the adjacent wells, which prevents reliable mineral composition estimation for those intervals.

Reservoir temperature and pressure were defined as the primary input parameters for estimating CO_2 adsorption capacity. A pressure gradient representative of a depleted reservoir was applied to determine formation pressure and temperature at

varying depths. Additional adsorption parameters were also considered, including the maximum adsorption capacity of individual minerals (q_m), the characteristic adsorption energy (E), the heterogeneity factor (n), and the universal gas constant (R). These parameters were subsequently used to compute CO_2 adsorption capacity within the three-dimensional (3D) grid model. The values of these parameters are discussed in a subsequent section. It should be noted that this workflow does not incorporate PVT data, as the present study does not involve dynamic simulation.

3.8.2 Structural Modelling Workflow

This section describes the workflow to create the three-dimensional (3D) structural model of the X field, as shown in Figure 3.11. The structural model forms the foundation of both geological and petrophysical models in 3D reservoir modelling. It is constructed based on horizons, zones, layering, and faults. The initial structural framework is established by digitising contour lines and fault lines from two-dimensional maps. Polygon lines are then identified and modelled to generate faults within the structural framework. Subsequently, the 3D grid is created using pillar gridding. The skeleton grid is automatically generated to define the top, middle, and bottom boundaries of the model. Porosity, facies, and water saturation data were interpreted using Techlog software. These data were subsequently used for stratigraphic correlation, resulting in the identification of thirteen zones (Table 3.3). Each zone was further subdivided into ten layers to optimise cell thickness while preserving model resolution. The final grid cell dimensions were 182 × 80 × 130 m, with a total of 1,892,800 grid cells. Figure 3.12 presents the final 3D structural model of the X field, including the fault system, skeleton grid, zones, and horizons.

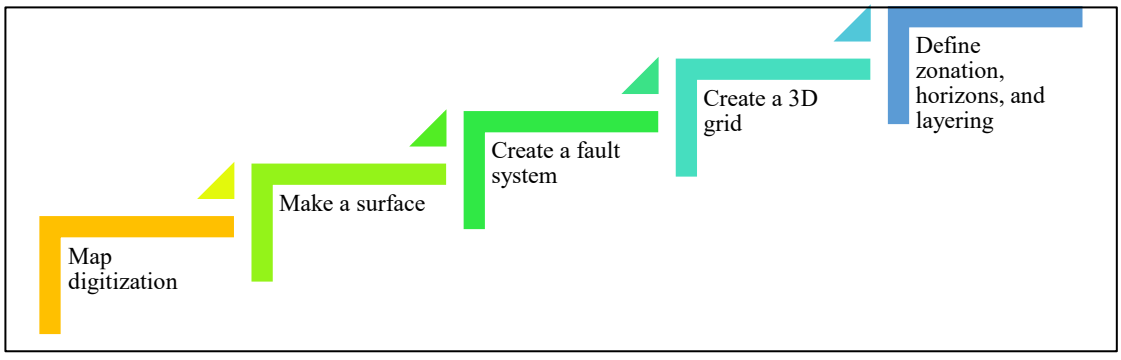

Figure 3.11 Flowchart for 3D Structural Modelling.

Table 3.3
Zonation Data.

Zonation	Measured Depth (m)		
	X-1	X-2	X-2ST1
B	1242	1252	1377
D1	1309.5	1321.63	1462.5
D2	1394	1416	1579
D3	1462	1484	1654
D4	1482	1519	1686
D5	1510	1542.5	1716
E1	1539	1570.5	1756.5
E2	1579	1615	1804
E3	1620	1651	1847.5
E4	1672	1715	1920
E5	1695	1740	1948.5
E6	1714	1756	1963
E7	1730	1770	1971

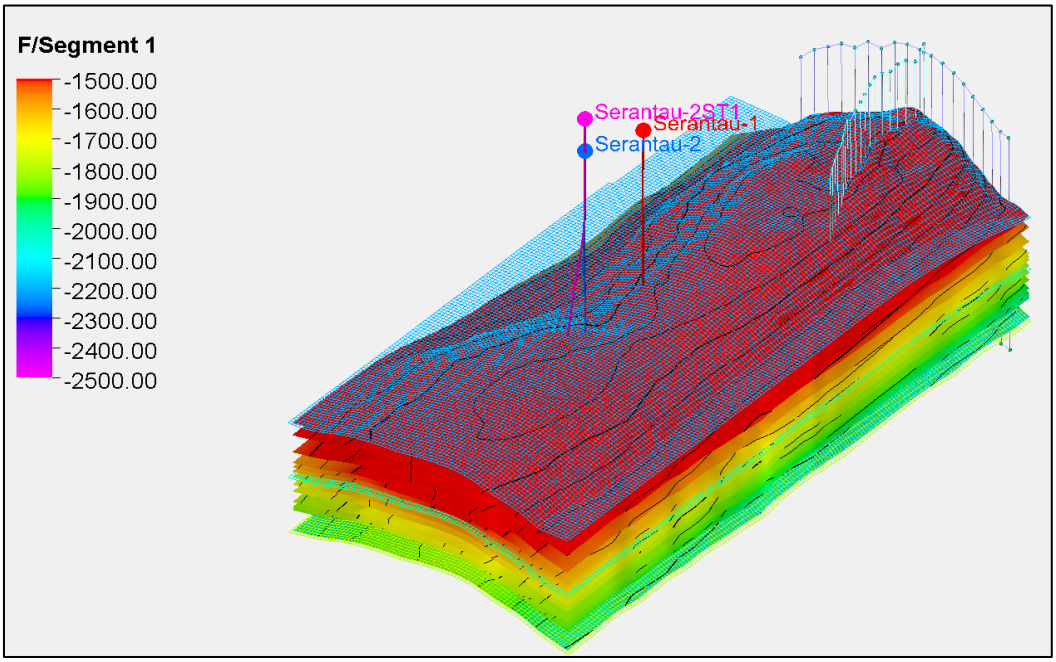

Figure 3.12 3D Structural Model of the X Field.

3.8.3 Facies and Mineralogy Modelling Workflow

The workflow for developing the mineralogy and facies models is presented in Figure 3.13. Both models characterise the geological nature of the subsurface, although they represent it in different ways. The mineralogy model is designed to visualise the proportions of individual minerals within each grid cell, whereas the facies model illustrates the spatial distribution of lithological units across the formation. In this study,

the mineralogy model is used to estimate the CO_2 adsorption capacity of different minerals, thereby enabling an assessment of the relationship between mineralogical composition and CO_2 adsorption capacity.

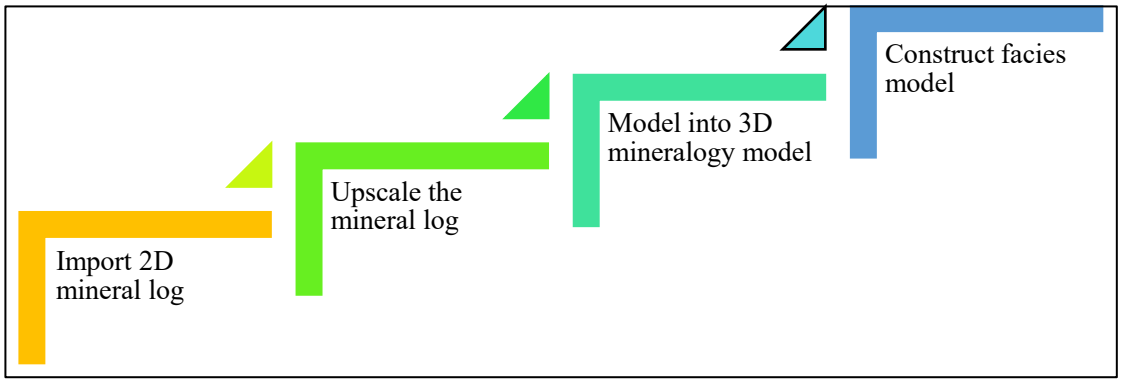

Figure 3.13 Flowchart for 3D Mineralogy and Facies Modelling.

The first step involves preparing the mineral composition data predicted by the machine learning model for the X-1 well. These data are then formatted as log curves, representing mineral fractions as a function of depth (Figure 3.14a). The workflow subsequently proceeds to the upscaling stage (Figure 3.14b). Each 2D mineral log is upscaled individually using an arithmetic averaging approach, which distributes mineral fractions across the strata according to the layering defined during structural modelling. The two-dimensional (2D) mineral logs are subsequently converted into three-dimensional (3D) grid cells. A separate 3D mineralogy model is generated for each mineral using the petrophysical modelling function in Petrel (Figure 3.14c). The modelling method, Gaussian random function simulation (GRFS), is selected for 3D mineralogy modelling to capture the spatial variability of the random field. This technique forms part of a conditional simulation framework that combines kriging with unconditional simulation (Iltaf et al., 2021). This method provides a more realistic representation of uncertain spatial distributions while maintaining relatively low computational cost.

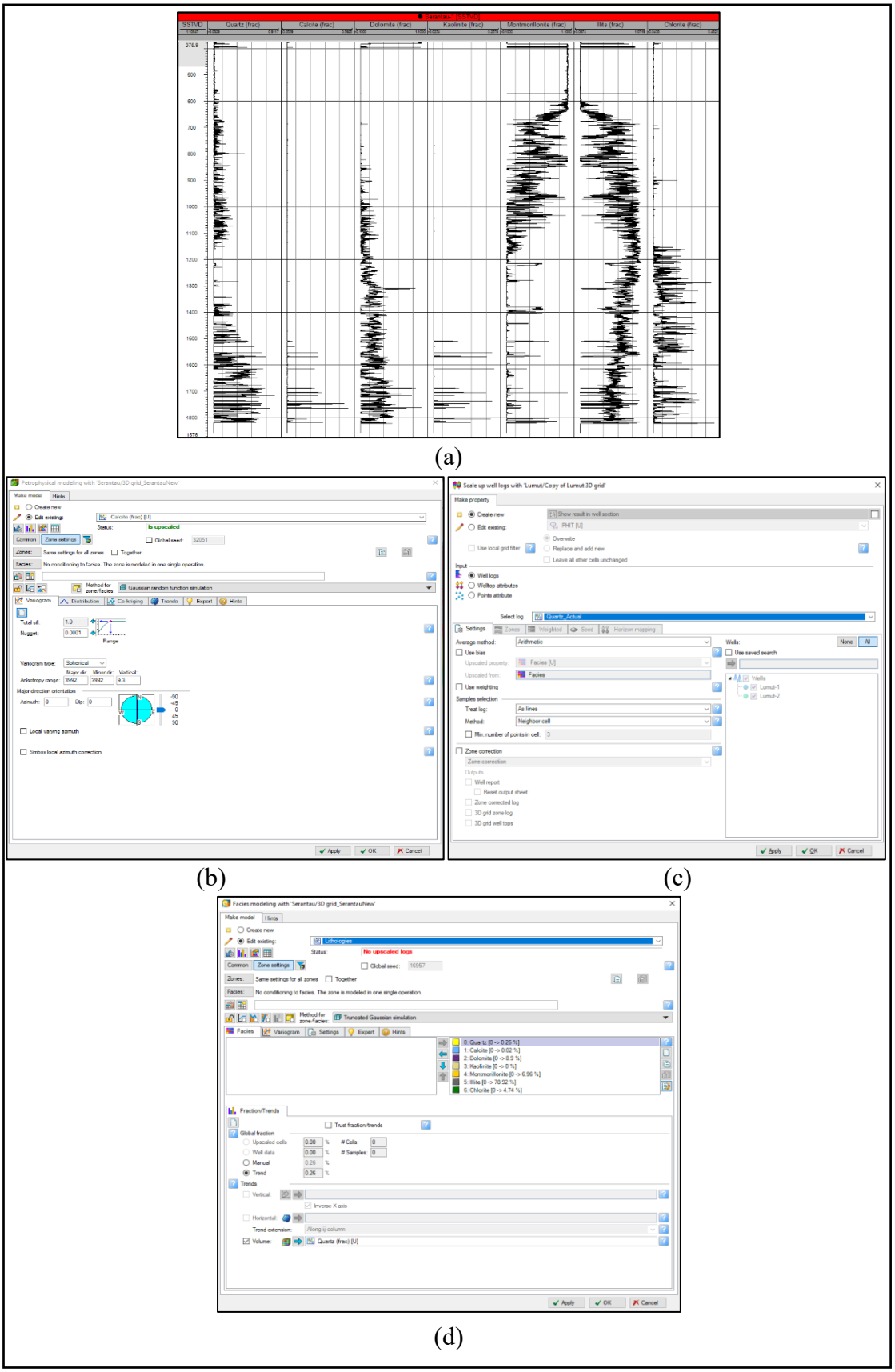

Figure 3.14 Mineralogy and Facies Modelling Process. (a) 2D Mineral Log; (b) Upscaling Setting; (c) Petrophysical Modelling Setting; (d) Facies Modelling Setting.

The 3D mineralogy models represent the distributions of quartz, calcite, dolomite, kaolinite, montmorillonite, illite, and chlorite. These mineralogy models are subsequently integrated into 3D facies modelling using the Truncated Gaussian Simulation (TGS) method, as illustrated in Figure 3.13d. This approach allocates property proportions across the area of interest based on variogram tuning (Pereira et al., 2023). The flexibility of this method is suitable for addressing the various uncertainties.

3.8.4 Adsorption Capacity Modelling Workflow

The final milestone of this research is the development of the three-dimensional (3D) adsorption capacity model. The workflow for this stage is concisely illustrated in the flowchart shown in Figure 3.15. Initially, the governing mathematical equation is derived based on comparisons established in the literature review. Subsequently, the key parameters influencing the adsorption isotherm are defined, including the adsorption coefficient and dependent variables such as pressure and temperature. These parameters are incorporated into a 3D grid model using the petrophysical modelling function.

The developed 3D grid model is then used to generate a 3D Polanyi potential model through the application of a 3D property calculator. Using the same approach, the Polanyi potential model is applied in the adsorption isotherm mathematical equation to estimate adsorption capacity and generate the 3D adsorption capacity model, as shown in Figure 3.15.

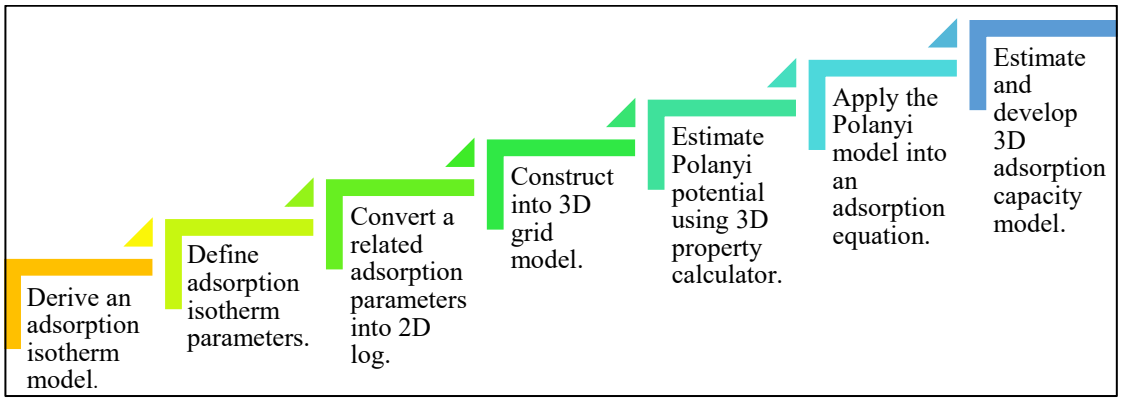

Figure 3.15 Flowchart for Adsorption Capacity Modelling.

3.8.5 Derivation of Adsorption Isotherm Model

The initial step involves deriving the mathematical equation for adsorption capacity based on the literature review. In this study, the Dubinin–Astakhov (D–A) model was selected because of its strong adaptability to heterogeneous subsurface conditions and its proven applicability to adsorption in porous geological media. The heterogeneity factor (n) represents the degree of subsurface formation variability and is directly reflected in the pore size distribution of the porous medium (Wedler & Span, 2021). Therefore, the estimation of adsorption capacity is fundamentally governed by mineralogical characteristics. The Dubinin–Astakhov mathematical formulation is derived from experimental data fitted to its linearised form and is expressed as follows:

$$q_e = q_m exp\left[-\left(\frac{\varepsilon}{E}\right)^n\right] \tag{4.16}$$

Where q_e is the amount of CO_2 adsorbed per unit mass of the specific minerals (mg/g), q_m is the maximum adsorption capacity of specific minerals (mg/g), ε is the Polanyi potential, E is the characteristic energy of adsorption (J/mol), n is a heterogeneity factor. The heterogeneity factor is based on several influencing factors, such as specific surface area (SSA) and pore volume of the minerals (T. Wang et al., 2023). An extensive literature review was conducted to determine the approximate value of these parameters, as shown in Table 3.4. Parameters n for quartz, calcite, and dolomite were assumed to be equal to 1 because of their non-complex physical properties, and the rest of the minerals are based on the experimental data in the literature.

Table 3.4
Approximate Values for the qm, n, and *E* Parameters.

Minerals	q_m **(mg/g)**	E **(J/mol)**	n
Quartz	0.5	5510	1
Calcite	1	4810	1
Dolomite	1	5971	1
Kaolinite	3	4123	1.413
Montmorillonite	10	5787	1.638
Illite	4	4689	1.245
Chlorite	3	4288	1.486

Sources: Gu et al. (2018), Tao et al. (2021), Y. Zhang, Li, et al. (2024), Akpasi & Isa (2022), Liang et al. (2016).

In the case of physical adsorption, the interaction between CO_2 and mineral surfaces is governed by dispersion forces, also known as van der Waals forces, which are intrinsically independent of temperature. Consequently, the temperature affects adsorption prediction through the Polanyi potential theory (P. Zhao et al., 2022). This theory describes the characteristic curve for the CO_2-mineral system, as shown in the expression:

$$\varepsilon = RT \ln\left(\frac{P_0}{P}\right) \tag{4.17}$$

Where R is the universal gas constant (8.314 J/mol·K), T is the reservoir temperature (K), P is the reservoir pressure (MPa), and P_o is the saturated pressure for CO_2, which is 7.38 MPa.

In this study, a depleted reservoir is chosen as a geological storage site for CO_2. In general, prolonged hydrocarbon production commonly results in a reduction of reservoir pressure and may induce wellbore instability (Shahbazi et al., 2020). Additionally, the isenthalpic expansion of CO_2 during injection can cause a significant decrease in reservoir temperature (Aghajanloo et al., 2024). Therefore, the formation pressure and temperature are expected to be lower than the hydrostatic pressure in the depleted reservoir. The changes in thermodynamic conditions may impact the adsorption capacity. To determine the formation pressure and temperature, we adopt a basic equation that is commonly used, as expressed below:

$$P = \left(\frac{dP}{dD}\right) \times D \tag{4.18}$$

$$T = T_s + (G + D) \tag{4.19}$$

Where dP/dD represents oil or water gradient (psi/ft), D is a depth (ft), T_s is the surface temperature (°C), and G is a geothermal gradient (°C/ft). We assume the oil and water gradients are equal to 0.265 and 0.3 psi/ft, respectively, due to the decreases in the formation pressure and temperature. Oil-water contact (OWC) was identified at a depth of 1652 m. The OWC is used to determine the pressure and temperature distribution within the reservoir, as it defines the boundary at which either an oil or a water pressure gradient is applied.

The mathematical formulation is applied by evaluating the adsorption behaviour of each mineral phase individually. To describe the adsorption potential of the entire formation, the total amount of CO_2 adsorbed is determined by summing the adsorption capacities of all minerals, as shown below:

$$q_{total} = \sum_{i=1}^{7} q_{e_i} \cdot M_i \tag{4.20}$$

Where M is the mineral fraction, and i is the type of minerals (quartz, calcite, dolomite, kaolinite, montmorillonite, illite, and chlorite). The estimation process generates eight adsorption capacity models: one model represents the total adsorption capacity contributed by all seven minerals, and the remaining seven models show the spatial distribution of adsorption capacity for individual mineral phases.

3.8.6 Spatial Mapping of the Adsorption Model.

This section describes the implementation of the mathematical formulation used to construct the three-dimensional (3D) adsorption capacity model. Figure 3.16 illustrates the workflow for visualising the adsorption-related parameter, namely the Polanyi potential. Initially, the continuous adsorption-dependent parameters, formation pressure and temperature were calculated and imported as two-dimensional (2D) well logs (Figure 3.16a), followed by an upscaling process (Figure 3.16b). The upscaled

pressure and temperature logs were then used to transform the 2D well log data into a 3D grid model through the petrophysical modelling function (Figure 3.16c). Finally, the Polanyi potential formulation was implemented within the 3D property calculator to estimate and spatially distribute the Polanyi potential across the formation (Figure 3.16d). The developed 3D Polanyi potential model is shown in Figure 3.17.

The subsequent step involves applying the 3D Polanyi potential property to the adsorption capacity equation. This formulation incorporates mineral fractions represented within the 3D grid model, together with mineral-specific adsorption coefficients. Figure 3.18a illustrates an example calculation of the adsorption capacity for quartz, integrating the 3D grid property model, Polanyi adsorption potential, mineral fraction, and constant adsorption coefficients. Similar calculations are performed for the remaining minerals. The individual mineral adsorption capacities are then aggregated (Figure 3.18b) to generate a 3D static reservoir model that visualises the potential amount of CO_2 adsorbed within the X Field.

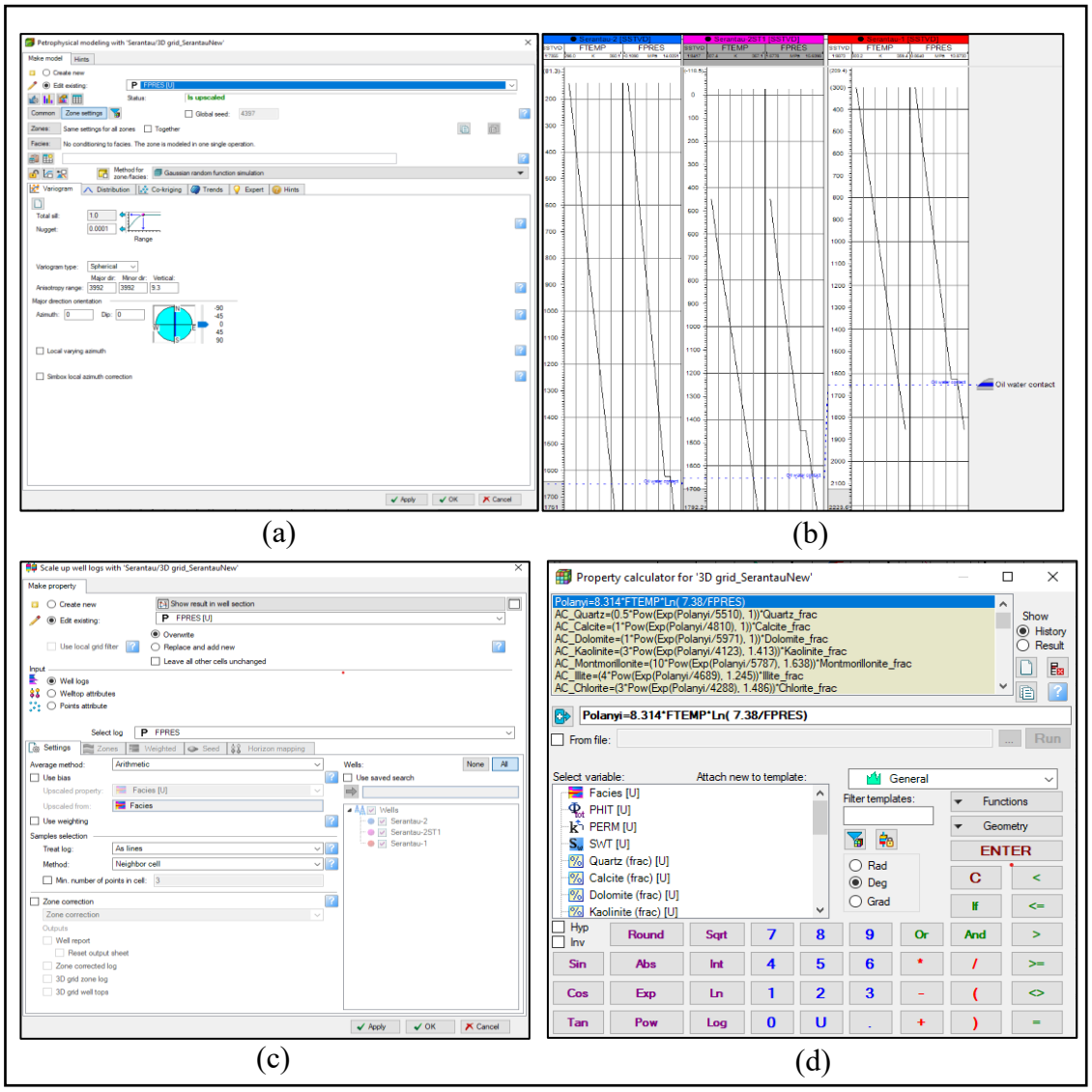

Figure 3.16 Adsorption Parameters Modelling Process. (a) 2D Log of Formation Pressure and Temperature; (b) Upscale Setting; (c) Petrophysical Modelling Setting; (d) Polanyi Potential Estimation on 3D Property Calculator.

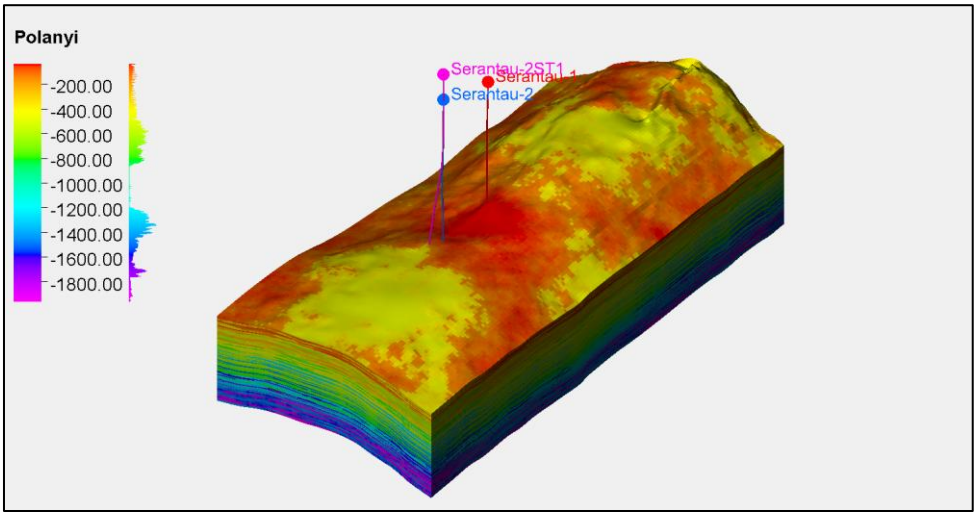

Figure 3.17 3D Polanyi Potential Model.

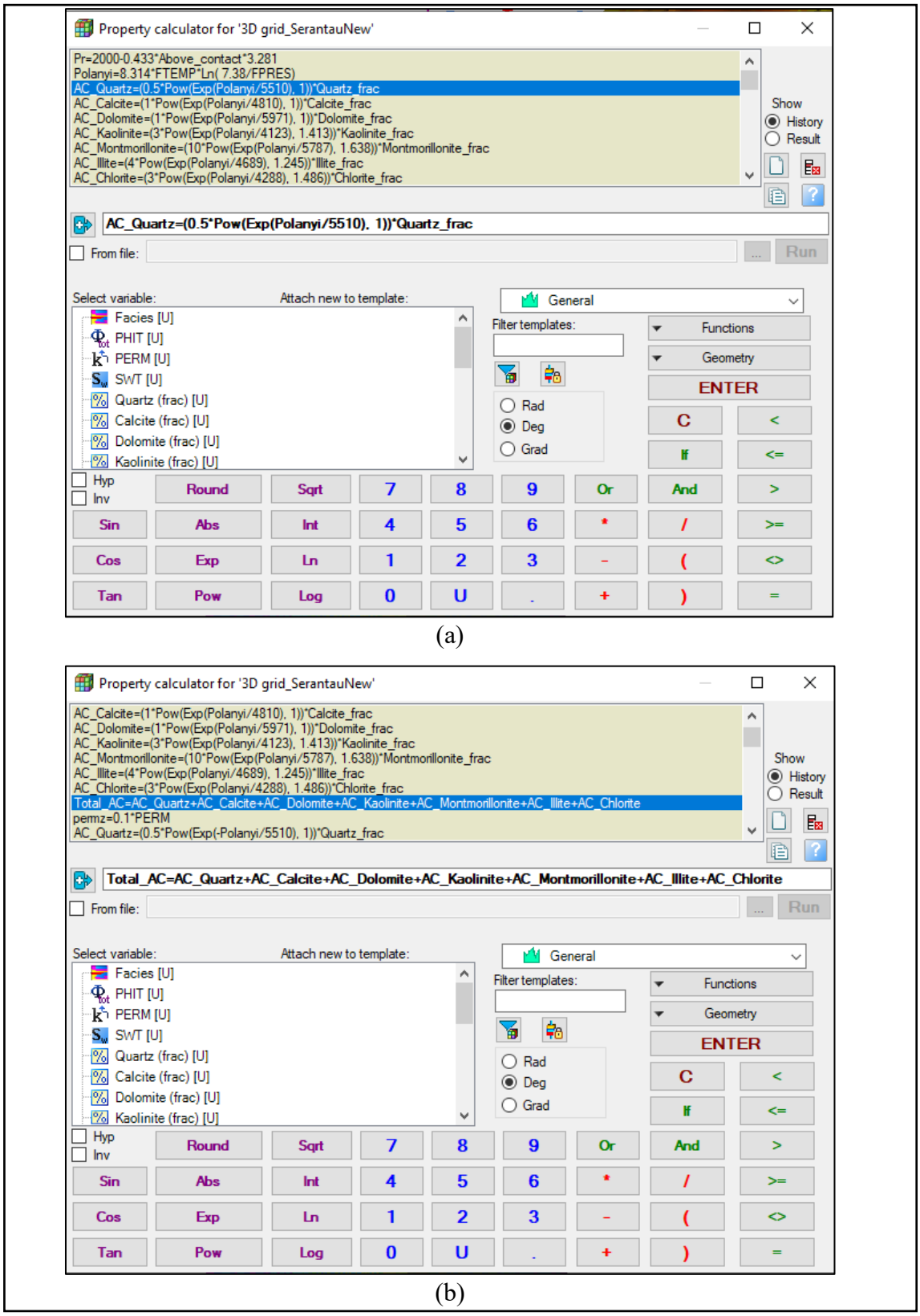

Figure 3.18 CO_2 Adsorption Capacity Estimation. (a) Adsorption Capacity for Each Mineral; (b) Total Adsorption Capacity across All Minerals.

3.8.7 Simulation

A three-dimensional (3D) static reservoir model for adsorption capacity was developed through upscaling and geological modelling. This model is used to simulate CO_2 storage performance under different scenarios, with reservoir condition parameters provided as inputs. The static simulation studies directly integrate adsorption capacity with key reservoir conditions, including pressure and temperature. This simulation was conducted under supercritical conditions, where the pressure and temperature are equal to or exceed 7.38 MPa and 31.1°C, respectively. To examine the effects of pressure and temperature on CO_2 storage performance, constant pressure and temperature values were applied across all depths. This approach also enables an assessment of the feasibility of implementing adsorption-based simulations within a 3D static reservoir model.

A basic workflow of 3D static modelling simulation consists of four steps, as shown in Figure 3.19. The initial step is to define the formation pressure and temperature under supercritical CO_2 conditions. In this simulation, the selected pressure and temperature ranges are 10 MPa, 15 MPa, and 20 MPa, and 303.15 K, 353.15 K, and 393.15 K, respectively. The selection of the pressure and temperature is based on the CO_2 adsorption experiment performed on the coal and activated carbon samples by Y. Chang et al. (2024) and Gomaa et al. (2022), respectively. These values are used to calculate the Polanyi potential, as presented in Table 3.5.

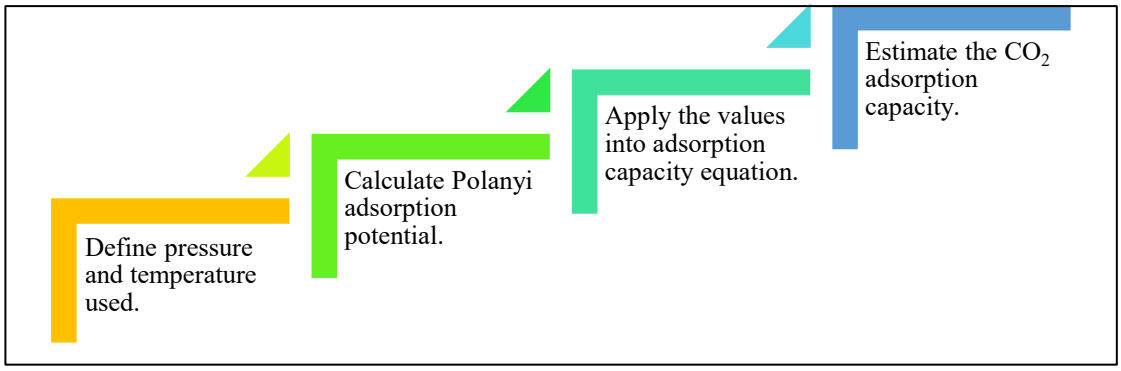

Figure 3.19 Flowchart for Third Research Objective.

Once the Polanyi potential is determined, the adsorption capacity is estimated following the methodology described in the preceding section. This estimation incorporates mineral fractions represented within the 3D grid model together with the

corresponding adsorption coefficients. The resulting CO_2 adsorption capacity under varying pressure and temperature conditions is then spatially distributed across the 3D static reservoir model. The results of this research are presented and discussed in Chapter Four.

Table 3.5
Polanyi Potential Data at Different Pressures and Temperatures.

Temperature (K)	Pressure (MPa)	Polanyi Potential (J/mol)
303.15	10	-765.72
	15	-1787.65
	20	-2512.72
353.15	10	-892.02
	15	-2082.50
	20	-2927.16
393.15	10	-993.05
	15	-2318.38
	20	-3258.71

CHAPTER 4
RESULTS AND DISCUSSIONS

This chapter presents a comprehensive discussion of the results derived from the methodology presented in the previous chapter. Overall, the findings highlight the novel integration of machine learning with reservoir characterisation workflows, demonstrating its capability to accurately predict mineral composition and to enable the successful development of high-resolution three-dimensional (3D) static reservoir models. A key focus of this study is the relationship between mineralogical properties and CO_2 adsorption capacity, which provides new insight beyond conventional interpretations of CO_2 geological storage and strengthens the understanding of mineral-controlled storage behaviour in subsurface formations. Through this chapter, the study aims to synthesise recent advancements in dynamic carbon capture and storage applications (CCS) by leveraging 3D reservoir modelling approaches. Despite the comprehensive analyses presented, inherent uncertainties persist, primarily due to limited data volume and insufficient parameter variability. Consequently, no single methodology can be regarded as universally optimal for this application. The chapter, therefore, concludes with critical insights, practical recommendations, and directions for future research to address these limitations and to advance the state of knowledge in this field.

4.1 Machine Learning for Mineral Prediction

4.1.1 Analysis of the Mineral Composition from Well Log Data on the Force Dataset Using a Simultaneous Equation Method

Figure 4.1 presents the available well logs for the Asgard Formation from the Force dataset, comprising gamma ray (GR), bulk density (RHOB), neutron porosity (NPHI), compressional slowness (DTC), and resistivity logs. In addition, facies information (sandstone, shaly sand, shale, marl, and dolomite) is provided to analyse the reliability of the estimated mineral composition of seven minerals (quartz, calcite, dolomite, kaolinite, montmorillonite, illite, and chlorite). In this formation, there are nine zones were classified and described as follows:

A1: The gamma ray (GR) log in this zone exhibits moderate to relatively high values, indicating a dominance of marl (calcareous clay) rather than pure shale. A minor presence of dolomite is also inferred. The consistently low resistivity suggests a water-saturated interval due to high shale or clay content (Chunmei et al., 2023).

A2: Both GR and resistivity logs show a slight increase within this zone. Mineralogical interpretation suggests comparable proportions of marl and shale. A thin sandstone layer is present at the top of the zone, interbedded with marl and shale; however, its influence on the well log response is minimal. This subdued response is attributed to the thin-bedded nature of the sandstone laminae, which are below the vertical resolution of the logging tools, as well as the dominance of clay-rich marl that masks the sandstone signal through volumetric averaging (Kolomytsev & Kalistratov, 2017).

B: The well log response in this zone is broadly similar to that of Zone A2. However, it is predominantly shale-rich, with several thin dolomite layers inferred from the higher GR readings. Elevated GR values indicate the presence of radioactive minerals commonly associated with clay or shale-rich lithologies (W. Hussain et al., 2024).

C1: At the top of this zone, elevated GR readings indicate shale dominance. With increasing depth, GR values decrease, suggesting a reduction in clay content. At specific depths, sandstone is inferred, as evidenced by a slight decrease in NPHI and DTC readings, accompanied by a marginal increase in RHOB readings.

C2: This zone is dominated by shale, as indicated by consistently high GR readings. Moreover, the presence of shaly sand layers was observed.

D: This zone is primarily composed of shale, with minor contributions from shaly sand and dolomite. The well log responses closely resemble those observed in the overlying zone, indicating minimal lithological variation.

E: This zone is entirely shale-dominated, as reflected by high GR readings and a slightly elevated NPHI response, which may indicate increased clay-bound water content.

F: Unusual well log responses are observed in this zone, particularly in the NPHI and RHOB logs. However, these anomalies do not significantly alter the overall facies interpretation. The zone remains predominantly shale, with minor occurrences of shaly sand layers.

G: Zone G is fully dominated by shale, as evidenced by consistently high GR readings. Slight increases in NPHI logs (Woo et al., 2021), and low resistivity (Zhu et al., 2023), further supports the interpretation of a compact, clay-rich lithology.

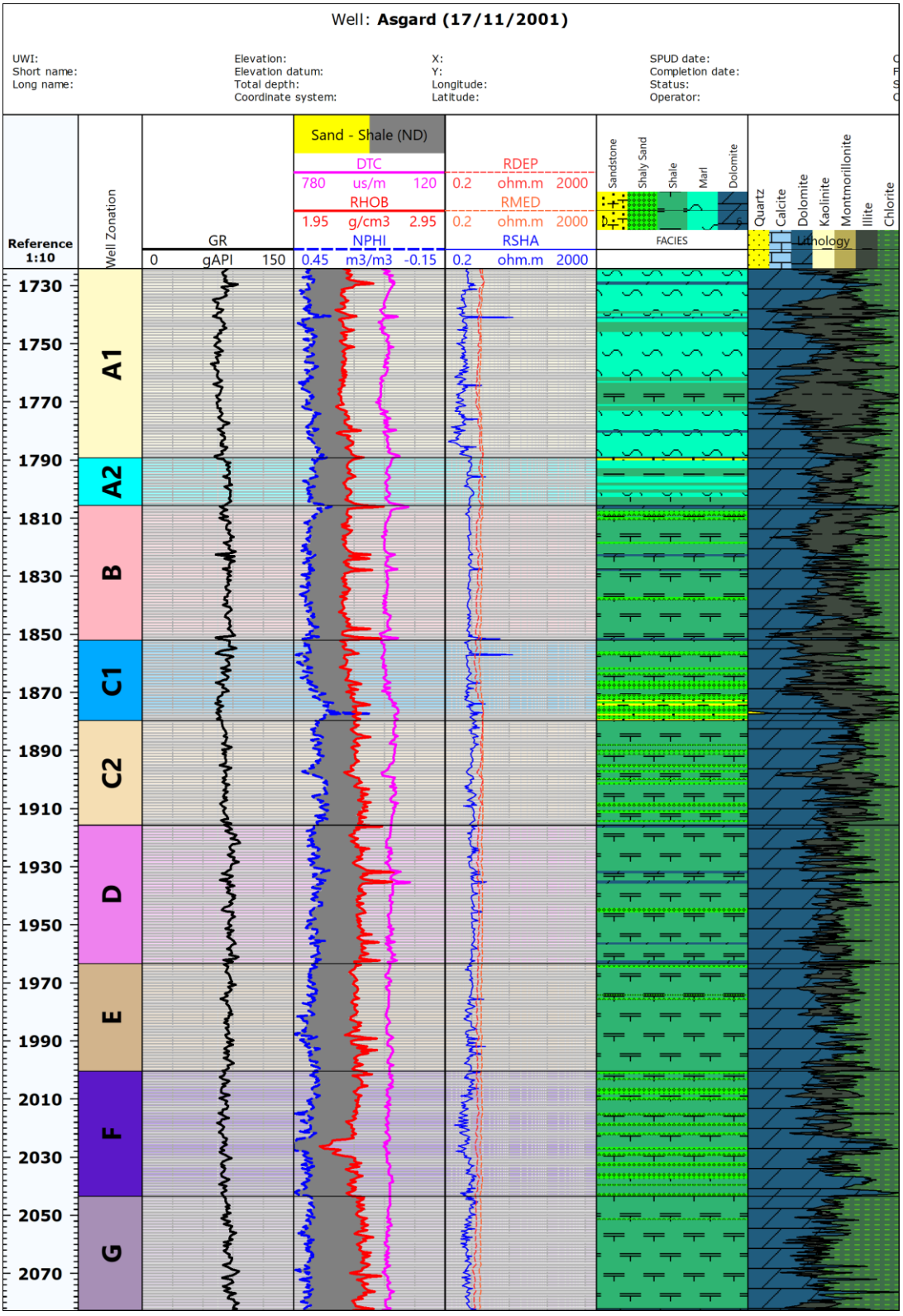

Figure 4.1 Well Log and Mineral Composition Interpretation on the Force Dataset.

The GR response, particularly around the mid-section of the interval, indicates a shaly or silty zone, which is further supported by high NPHI and low resistivity responses. Hydrocarbon-bearing zones are typically inferred from NPHI–RHOB crossovers, and together with resistivity logs, with larger separations commonly associated with gas and smaller separations with oil (Eid et al., 2025a). In this case, the Asgard Formation exhibits no distinct NPHI–RHOB crossover indicative of hydrocarbons; when considered in conjunction with the resistivity response, this observation suggests that the interval is likely water-bearing.

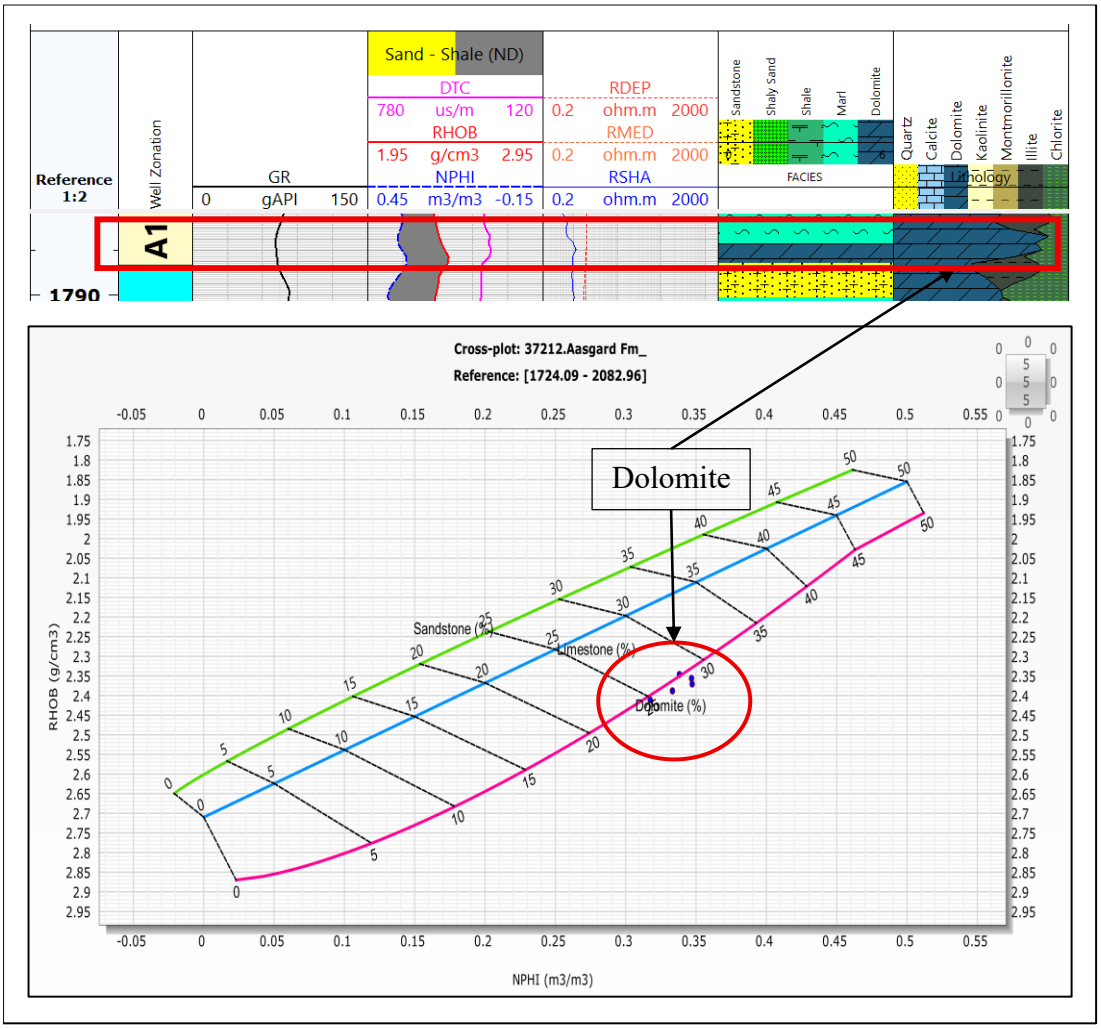

Figure 4.2 NPHI-RHOB Cross-Plot for Dolomite Identification on the Force Dataset.

Using an NPHI–RHOB cross-plot to distinguish lithologies and identify clusters that follow dolomite-rich versus clay-rich trends is a common industry practice (Yahia et al., 2025), particularly when trendlines or templates are calibrated against available facies information. The NPHI–RHOB cross-plot for the Asgard Formation reveals two

distinct clusters corresponding to dolomite and clay-dominated intervals. The zone between 1788 and 1789 m exhibits a notably high dolomite content, characterised by average GR, RHOB, and NPHI values of 72 API, 2.30 g/cm³, and 0.33, respectively. The moderate GR responses, which are close to the clean-formation baseline, indicate a reduced concentration of radioactive clay-rich minerals at this depth (Djoï, 2024). However, GR alone is insufficient to differentiate dolomite from limestone or clean sandstone; dolomite identification typically depends on the diagnostic NPHI response and, where available, supporting facies information (Hussein, 2023). When the NPHI response, facies description, and the NPHI–RHOB cross-plot in Figure 4.2 are considered collectively, the evidence supports the interpretation of a dolomite-dominated interval.

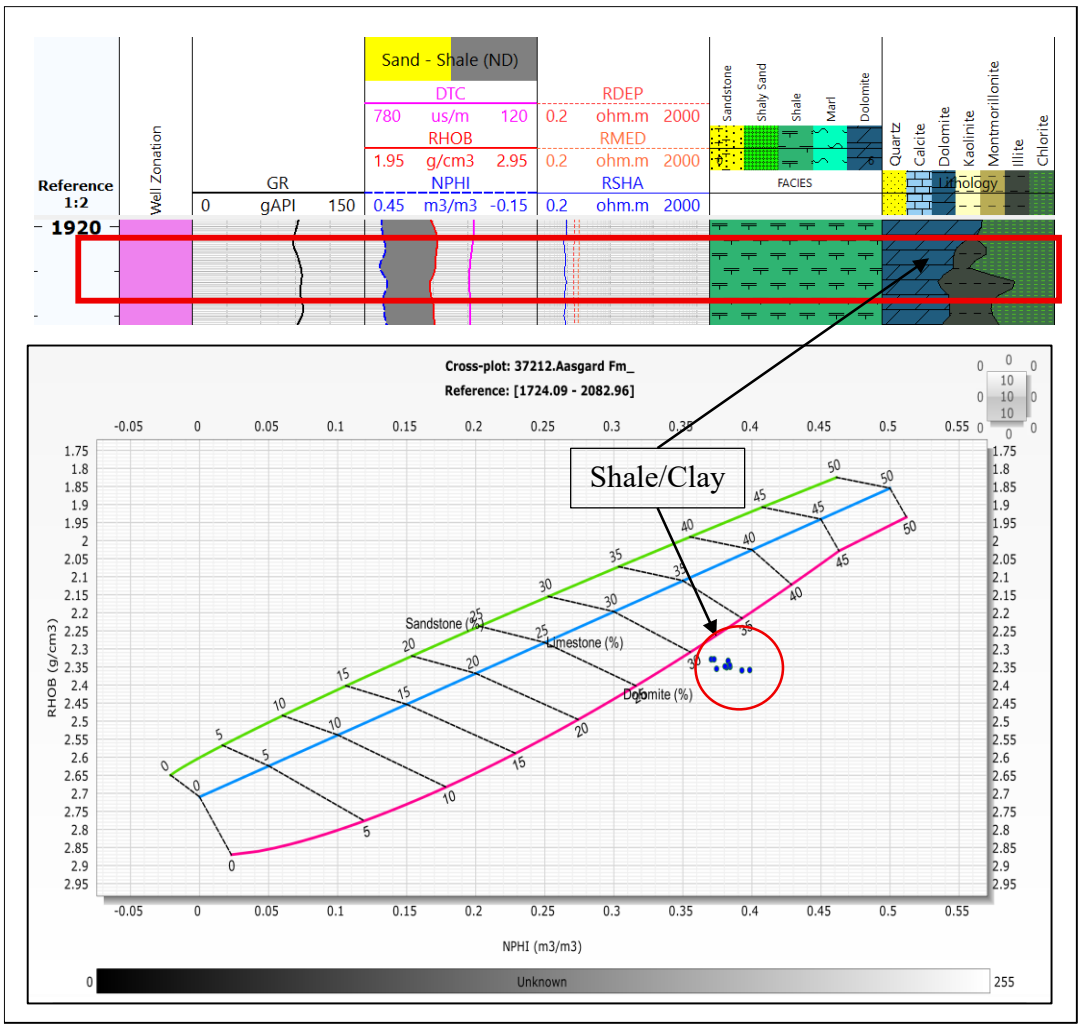

Figure 4.3 NPHI-RHOB Cross-Plot for Shale Clay Identification in the Force Dataset.

Between 1920 and 1922 m, a clay-rich zone is identified, with average GR, RHOB, and NPHI values of 94 API, 2.3 g/cm³, and 0.38, respectively. The relatively elevated GR and NPHI responses indicate a strong clay mineral signal, which is reflected by the corresponding facies interpretation. The cross-plot results in Figure 4.3 show that the data points fall below the dolomite line. The formation appears to be predominantly clay or shale, which is commonly associated with lower RHOB values due to its less compacted structure and relatively high porosity (Lei et al., 2022). Overall, the estimated mineral composition demonstrates reasonable agreement with the expected geological interpretation.

4.1.2 Analysis of the Mineral Composition from Well Log Data in the X Field Dataset Using a Simultaneous Equation Method

In the X Field, thirteen zones were identified and classified based on well log responses and lithological characteristics, as constructed in Figure 4.4b. Using the log interpretation, the zones were described as follows:

B: A clay-rich zone is identified based on high GR log values, ranging approximately from 85 to 135 gAPI. The NPHI–RHOB crossover and elevated resistivity are also observed, which are commonly associated with the presence of hydrocarbon gas (Eid et al., 2025a). It should be noted that hydrocarbons significantly influence the interpretation of NPHI and RHOB responses. As a result, certain gas-bearing intervals are misclassified as montmorillonite. This misclassification occurs because the gas effect reduces RHOB values, producing responses similar to those characteristics of montmorillonite. The simultaneous inversion method assumes water-filled pore space; therefore, this assumption results in overlapping log responses and ambiguous interpretations in gas-bearing intervals. Without applying gas corrections, the simultaneous equation approach is unable to correctly identify these depths as clean sandstone.

D1: High GR values, ranging approximately from 80 to 140 gAPI, indicate a clay-rich interval with a minor hydrocarbon presence at a depth of 1308 m. An increase in dolomite content is also observed.

D2: The clay-rich zone is identified by elevated GR readings, ranging approximately from 80 to 145 gAPI. Higher hydrocarbon potential in the form of gas is

observed between depths of 1406 and 1430 m, as indicated by a pronounced NPHI–RHOB crossover and elevated resistivity.

D3: A clay-rich zone is identified by GR readings ranging from 110 to 135 gAPI, followed by intervals dominated by dolomite and quartz. The absence of significant resistivity variation, together with a small NPHI–RHOB crossover, indicates the presence of an oil-bearing zone.

D4: A quartz exists in the oil-bearing zone at depths 1493 to 1500 m because of the small separation of NPHI and RHOB logs, and moderate resistivity readings. Overall, this zone was dominated by clay content with GR readings ranging from 85 to 140 gAPI.

D5: A clay-rich interval is identified by elevated gamma ray values ranging from 80 to 140 gAPI, with minor contributions from dolomite and quartz. The presence of hydrocarbon gas is inferred from a pronounced increase in resistivity and a clear NPHI–RHOB crossover.

E1: High GR reading indicates a clay-rich zone in almost every depth. A minor amount of quartz was also identified within the oil-bearing zone.

E2: The interval is dominated by clay, with minor amounts of dolomite and quartz. Two distinct layers exhibiting gas effects are identified within this zone.

E3: Quartz and clay are the dominant minerals within this zone. A minor hydrocarbon-related effect is observed near 1640 m, where an elevated resistivity response may indicate the presence of gas. Between 1644 and 1671 m, a small NPHI–RHOB crossover suggests a hydrocarbon-bearing interval, most likely oil-saturated rather than gas-charged when integrated with the resistivity response. This interval is interpreted as shaly sand, consistent with its relatively low RHOB value and an average NPHI value of approximately 0.20.

E4: A clay-rich interval is indicated by elevated GR values ranging from approximately 80 to 120 gAPI, with minor amounts of quartz and dolomite. The absence of a resistivity peak confirms that no hydrocarbons are present in this zone.

E5: A clay-rich interval is identified by elevated GR values ranging from approximately 90 to 130 gAPI, with only minor contributions from dolomite and quartz. A single hydrocarbon-bearing layer is observed at a depth of 1704 m, indicated by an NPHI–RHOB crossover in conjunction with a moderate resistivity response.

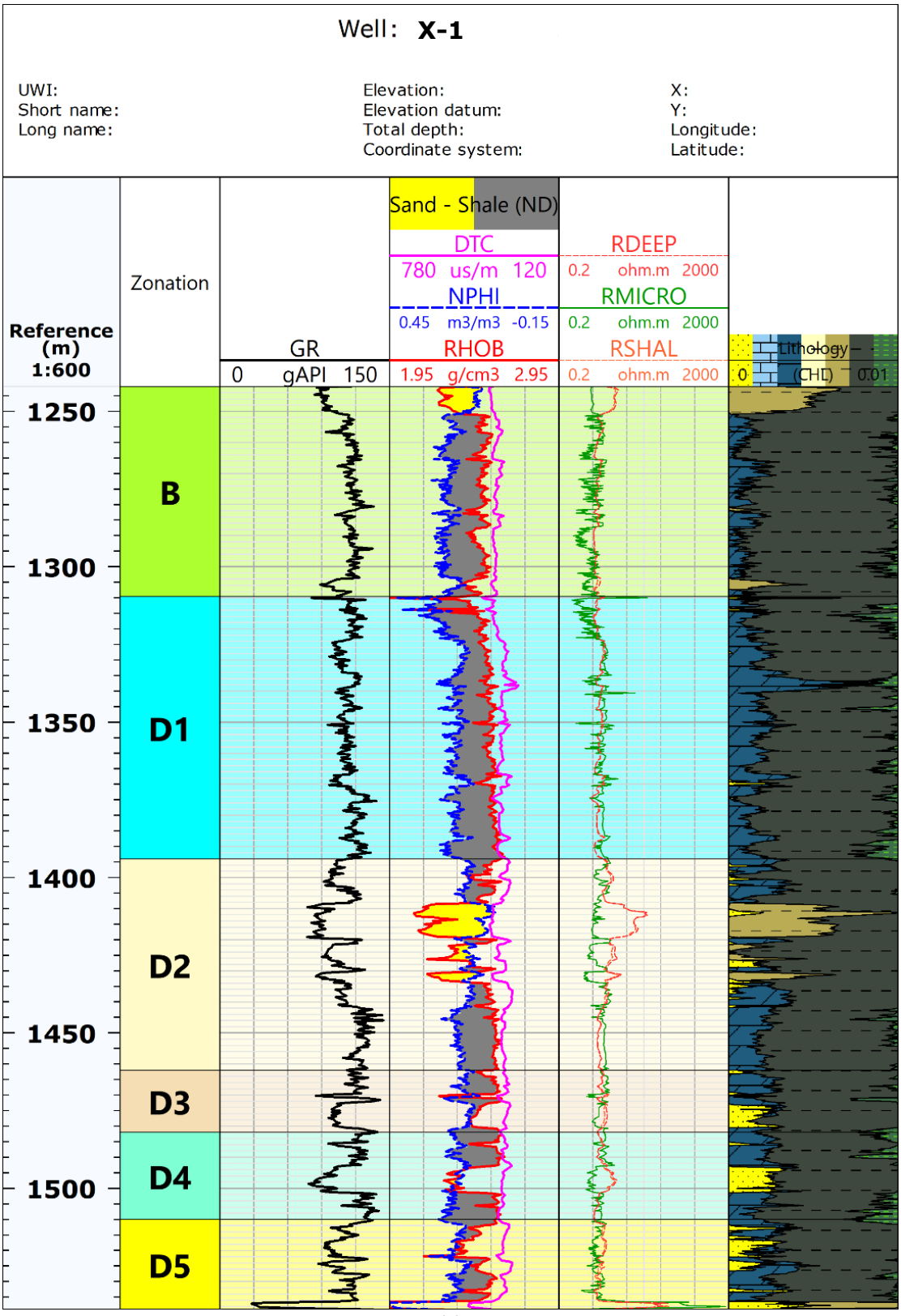
Well: X-1
UWI:
Short name:
Long name:
Elevation:
Elevation datum:
Total depth:
Coordinate system:
X:
Y:
Longitude:
Latitude:
Reference (m) 1:600
Zonation
GR
0 gAPI 150
Sand - Shale (ND)
DTC
780 us/m 120
NPHI
0.45 m3/m3 -0.15
RHOB
1.95 g/cm3 2.95
RDEEP
0.2 ohm.m 2000
RMICRO
0.2 ohm.m 2000
RSHAL
0.2 ohm.m 2000
Lithology
0 (CHL) 0.01
1250
1300
1350
1400
1450
1500
B
D1
D2
D3
D4
D5

(a)

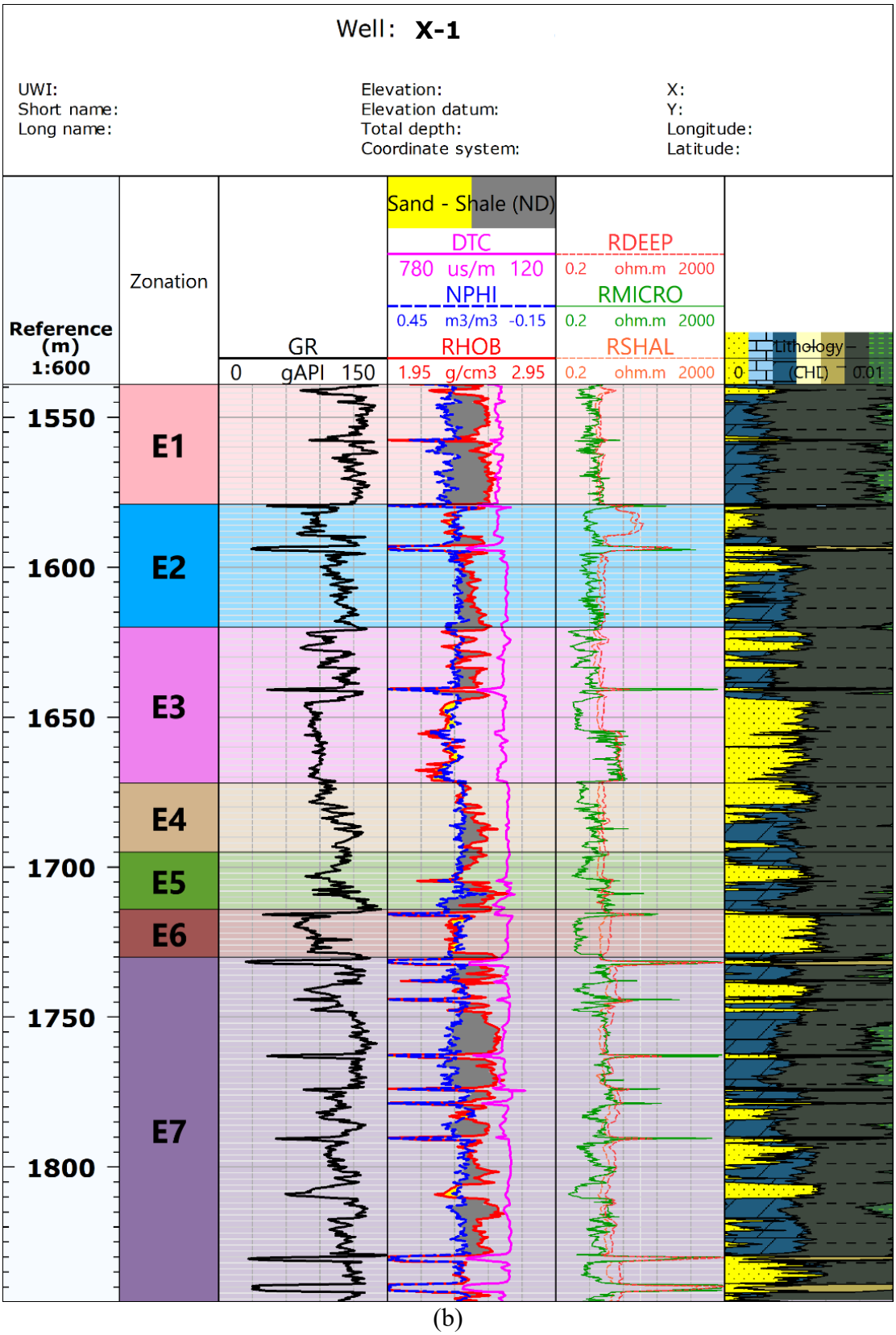

(b)

Figure 4.4 Well Log Combined with Mineral Composition on the X Field Dataset. (a) Zone B – D5; (b) Zone E1 – E7.

E6: The mineral composition suggests that the zone is characteristic of shaly sand. At the upper boundary of the interval, around 1715 m, an elevated resistivity response indicates a possible gas-related effect. Below this depth, the interval is interpreted as oil-bearing, as evidenced by a small NPHI–RHOB crossover in combination with a moderate resistivity response.

E7: A clay-rich zone was found since the GR reading was higher in some intervals, together with a trace amount of dolomite and quartz. Five layers exhibit trace amounts of hydrocarbons in gaseous form within the zone, as indicated by pronounced peaks in the resistivity log. The GR, RHOB, and NPHI logs exhibit elevated responses with increasing clay content. In contrast, their values decrease as the proportions of quartz and dolomite increase. The resistivity log, meanwhile, shows a strong correspondence with quartz content.

Taken together, these conventional well logs capture distinct mineralogical responses within the formation and constitute a fundamental input dataset for training machine learning models to quantitatively infer mineralogical composition from well log measurements.

Three mineralogical clusters are identified within the X field, namely quartz, dolomite, and clay. These clusters are distinguished using a neutron density cross-plot, as shown in Figure 4.5, which is employed to evaluate the accuracy of the simultaneous equation method in estimating mineral composition from conventional well log data in the X field dataset.

At depths between 1808 and 1810 m, quartz and clay are observed within the hydrocarbon-bearing zone. The average GR, RHOB, and NPHI values at this interval are 66 API, 2.27 g/cm^3, and 0.20, respectively (Figure 4.5). The low GR reading indicates a minimal presence of radioactive minerals. Concurrently, the reduced RHOB and NPHI responses suggest that the interval is predominantly quartz-rich. The NPHI-RHOB cross-plot further indicates that the data points cluster between the sandstone and limestone reference lines, suggesting that the interval comprises a mixture of quartz and shale, which is characteristic of a shaly sand formation.

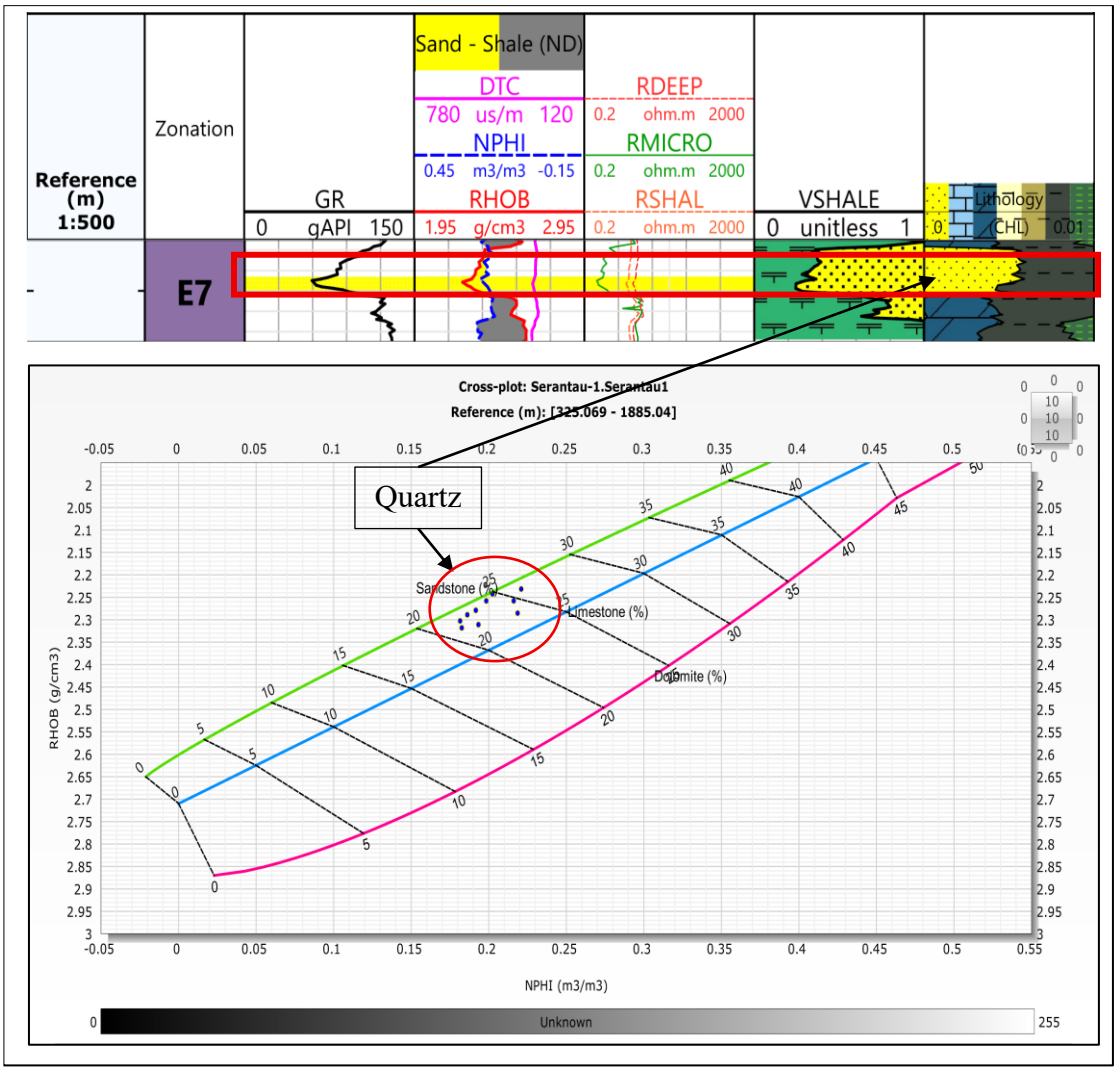

Figure 4.5 NPHI-RHOB Cross-Plot for Quartz Identification on the X Field Dataset.

A dolomite layer was observed at depth from 1336 to 1340 m with an average of GR, RHOB, and NPHI readings of 114 API, 2.53 g/cm3, and 0.23 (Figure 4.6). The elevated GR and RHOB readings suggest the presence of dolomite within the formation. The NPHI-RHOB cross-plot indicates that the data points lie predominantly along the dolomite reference line, with slight scatter above it. This observation suggests that the interval is dominated by dolomite-rich lithology.

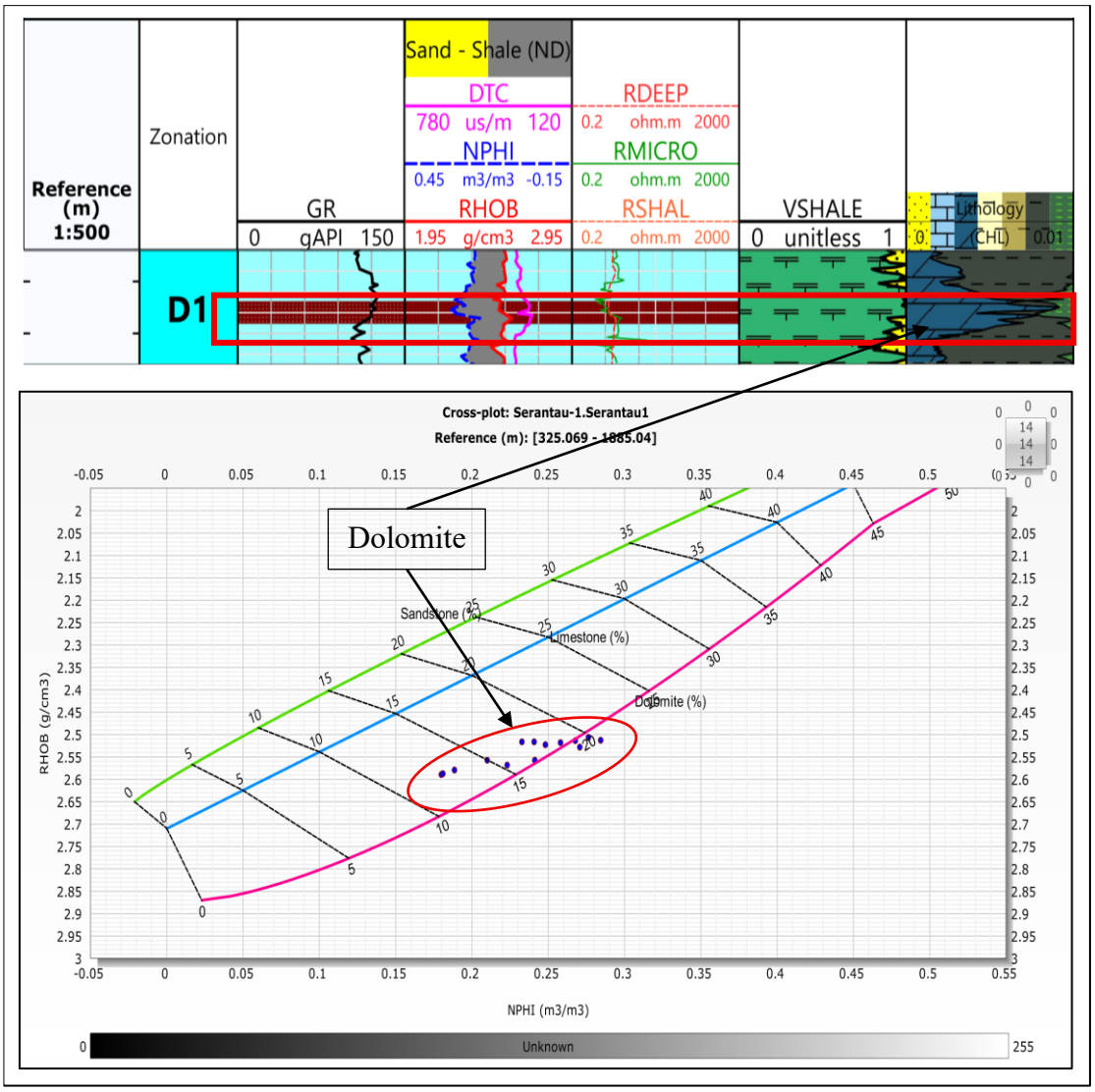

Figure 4.6 NPHI-RHOB Cross-Plot for Dolomite Identification on the X Field Dataset.

The interval between 1561 and 1562 m is interpreted as shale- or clay-rich, with average GR, RHOB, and NPHI values of 126 API, 2.48 g/cm³, and 0.28, respectively (Figure 4.7). The high GR response, which is close to the shale baseline, indicates an increased concentration of radioactive clay-bearing minerals. The NPHI–RHOB cross-plot shows that most data points plot below the dolomite trend line, suggesting that the interval is primarily composed of clay minerals. The RHOB and NPHI values further reinforce this interpretation, as both logs typically exhibit higher readings in clay-dominated intervals. Accordingly, this interval is interpreted as being dominated by clay-rich lithology.

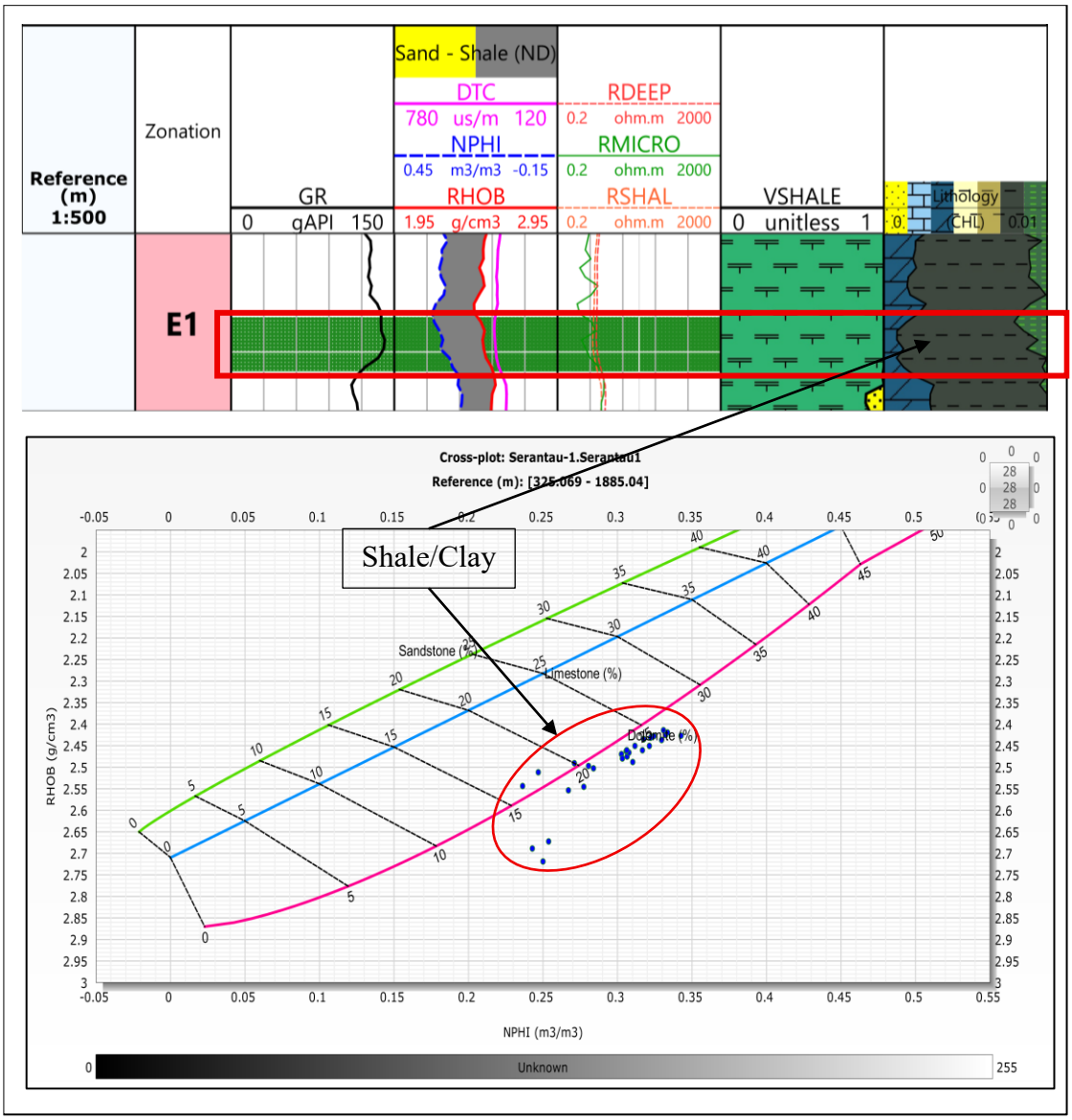

Figure 4.7 NPHI-RHOB Cross-Plot for Shale Clay Identification on the X Field Dataset.

4.1.3 Data Description and Analysis Based on the Heatmap

Figure 4.8 represents a correlation heatmap illustrating the relationships between the well log responses and the estimated mineral composition. Usually, the darker the colour of the cell, the higher the correlation. A strong positive correlation indicates that as one variable increases, the other variable also tends to increase, while a strong negative correlation suggests an inverse relationship where an increase in one variable corresponds to a decrease in the other.

The RHOB, NPHI, and DTC logs exhibit significant correlations with mineralogical components because these logs are fundamentally governed by rock

properties, particularly porosity and mineral composition (Bhattacharya, 2022). In this study, well log responses demonstrate stronger correlations with quartz, dolomite, montmorillonite, and illite compared to other minerals, and the underlying reasons for these relationships are discussed below.

Among the carbonate minerals, well log responses show the strongest correlation with dolomite. The strong positive correlation between dolomite and RHOB log is attributed to the relatively high matrix density of dolomite (2.87 g/cm³). Conversely, the DTC log exhibits a strong negative correlation with dolomite. Their stable crystal packing and high rock stiffness reflect reduced compressional travel time (Weger et al., 2024). On the other hand, a weak correlation between NPHI log and dolomite is explained by the low hydrogen content of dolomite-rich formations (Z. Feng et al., 2022).

NPHI and DTC logs display moderate negative correlations with quartz. Generally, the physical characteristics of quartz-rich formations are tightly packed and mechanically stiffer (Ahmad, 2025). However, the comparatively lower matrix density and longer compressional travel time suggest that quartz-rich formations exhibit a lower stiffness than dolomite-rich formations. The RHOB log shows close-to-zero correlation with quartz. The influence of hydrocarbon gas effects within the study interval significantly miscalculates the matrix density of the quartz, resulting in overlaps with the identical mineral properties, which are montmorillonite.

Well log responses exhibit distinct and systematic relationships with clay minerals, particularly montmorillonite and illite. DTC and NPHI logs show strong positive correlations with montmorillonite, consistent with its high bound-water content and swelling characteristics (S. Li et al., 2022). Its strong negative correlation with RHOB log reflects lower bulk density associated with high porosity and expandable clay behaviour (Noreen et al., 2025). In contrast, DTC and RHOB logs display moderate correlations with illite, weaker than those observed for montmorillonite. This response can be attributed to illite's slightly higher matrix density and reduced compressional travel time, which are consistent with its lower water content and more compact crystal structure (Singh, 2022).

In summary, the correlation heatmap confirms that well log responses are strongly governed by mineralogical composition, particularly carbonate and clay minerals. The pronounced sensitivity of RHOB, NPHI, and DTC logs to quartz,

dolomite, montmorillonite, and illite highlights their critical role in lithological classification.

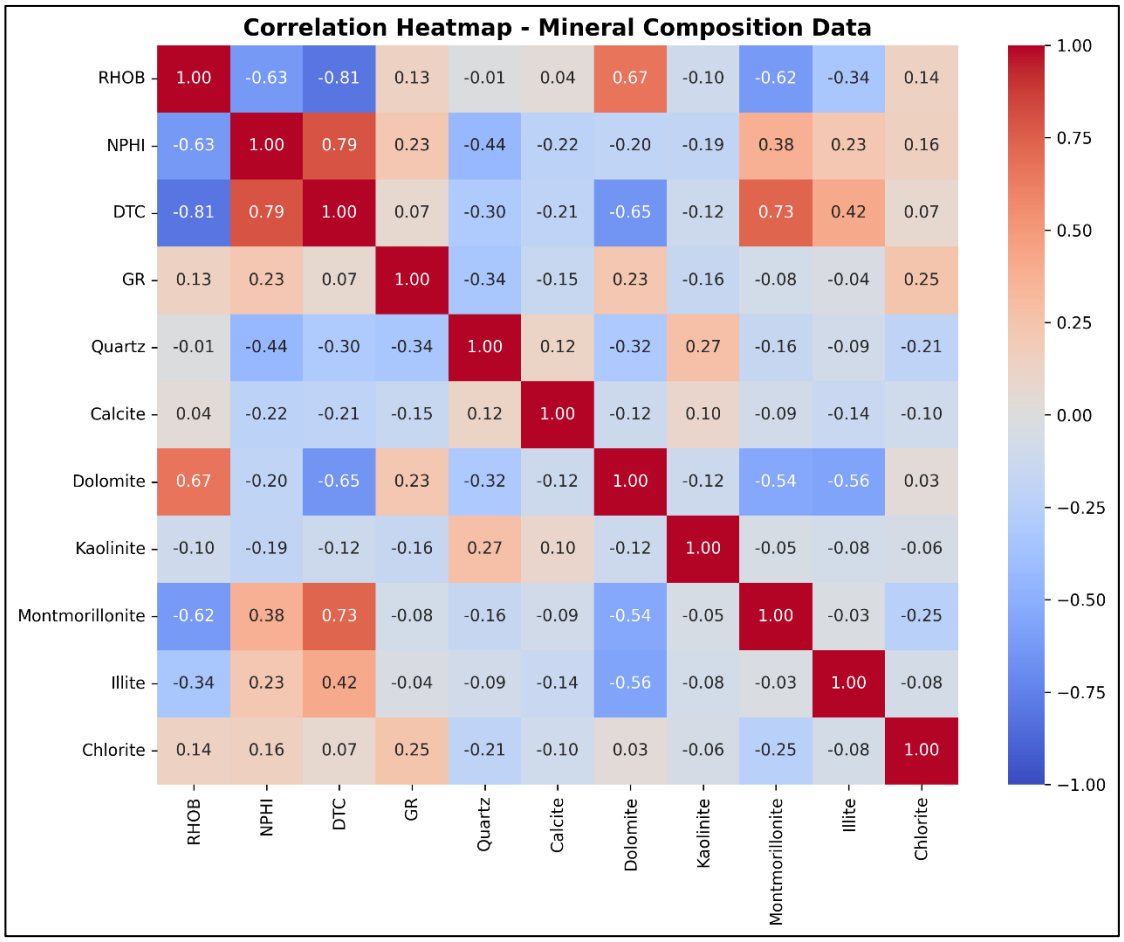

Figure 4.8 Heatmap of Well Log and Mineral Composition Correlation Matrix.

4.1.4 Training the XGBoost Model on the Force Dataset

This section describes the development and evaluation of an XGBoost model performance using the Force dataset, with three well log inputs: RHOB, NPHI, and DTC logs, to estimate the mineral fraction of seven minerals. Given the large size of the Force dataset, comprising approximately 640,000 data points, the data were randomly split into training and testing sets using a 95:5 ratio. Hyperparameter optimisation was performed to determine the model configuration that produced the lowest prediction error Table 4.1. Finally, a post-processing normalisation step was applied to ensure that the predicted mineral fractions summed to one.

Table 4.1
Optimised Hyperparameters for the XGBoost Model.

n_estimator	learning_rate	max_depth	subsample	colsample_by tree
150	0.05	6	0.8	1

The performance metrics, including RMSE, MAE, and R^2, were used to evaluate the performance of the XGBoost model on the testing dataset. The model demonstrates high predictive accuracy and minimal performance discrepancy between the training and testing datasets, indicating good generalisation (Table 4.2). These results confirm the effectiveness of the optimised hyperparameters selected during the model development stage. Overall, the model exhibits strong predictive capability, as evidenced by high R^2 values and low error metrics, supporting the suitability of XGBoost for predicting mineral composition from conventional well log data.

Table 4.2
Performance of the ML Model on the Force Dataset.

Mineral	Training			Testing		
	MAE	RMSE	R^2	MAE	RMSE	R^2
Quartz	0.010	0.025	0.986	0.010	0.027	0.983
Calcite	0.008	0.030	0.918	0.008	0.031	0.912
Dolomite	0.014	0.029	0.995	0.015	0.030	0.994
Kaolinite	0.001	0.005	0.965	0.001	0.006	0.953
Montmorillonite	0.003	0.009	0.999	0.003	0.009	0.999
Illite	0.017	0.027	0.991	0.017	0.027	0.991
Chlorite	0.011	0.021	0.978	0.011	0.021	0.977

The XGBoost-trained model demonstrates strong predictive performance using only three well log inputs, in contrast to the approach of Hu et al. (2023), which employed six well logs to achieve comparable predictions. This observation suggests that increasing the number of input logs does not necessarily enhance model performance and may, in some cases, introduce unnecessary complexity. In the subsequent section, a blind test using the X Field dataset from a different basin is conducted to further assess the robustness of the model.

4.1.5 Application of the Trained XGBoost Model on the X Field Dataset

The XGBoost-trained model was applied to the X-1 field well for mineral composition prediction based on conventional well log inputs: RHOB, NPHI, and DTC logs. Table 4.3 demonstrates the ML model's performance in predicting the mineral composition of seven minerals on the X field dataset. The overall performance was evaluated on the blind dataset, achieving an MAE of 0.009, an RMSE of 0.021, and an R^2 score of 0.884. Therefore, the XGBoost model demonstrated strong performance in predicting mineral composition acrossdifferent basins.

Table 4.3
Performance of the ML Model on the X Field Dataset.

Mineral	**RMSE**	**MAE**	**R^2**
Quartz	0.012	0.026	0.959
Calcite	0.002	0.019	0.705
Dolomite	0.011	0.024	0.988
Kaolinite	0.001	0.010	0.639
Montmorillonite	0.011	0.021	0.997
Illite	0.020	0.031	0.991
Chlorite	0.005	0.012	0.911
Overall	0.009	0.021	0.884

Figure 4.9 shows the actual and predicted mineral composition values of the seven minerals for the X field dataset. Five minerals show excellent R^2 scores, namely quartz, dolomite, montmorillonite, illite, and chlorite. In contrast, calcite and kaolinite exhibit substantially lower R^2 scores because their concentrations are extremely low, making the relative variance difficult to capture accurately. However, their lower RMSE and MAE give a strong indication that the model is making an accurate prediction in absolute terms, showing the predicted values are numerically close to the actual values.

To assess result consistency, the predicted and reference mineral compositions are evaluated through side-by-side visualisation within the well log interpretation framework. Figure 4.10 presents the GR log to distinguish clay-rich intervals from other lithologies, while the corresponding mineral composition profiles are displayed on the right, including mineral fractions predicted by the XGBoost model (red dots) and those

estimated using the simultaneous equation. As observed, the mineral composition trends predicted by the XGBoost-trained model closely follow those derived from the simultaneous equation method. Exceptions are noted for calcite and kaolinite, for which visual interpretation is limited due to their relatively low abundances.

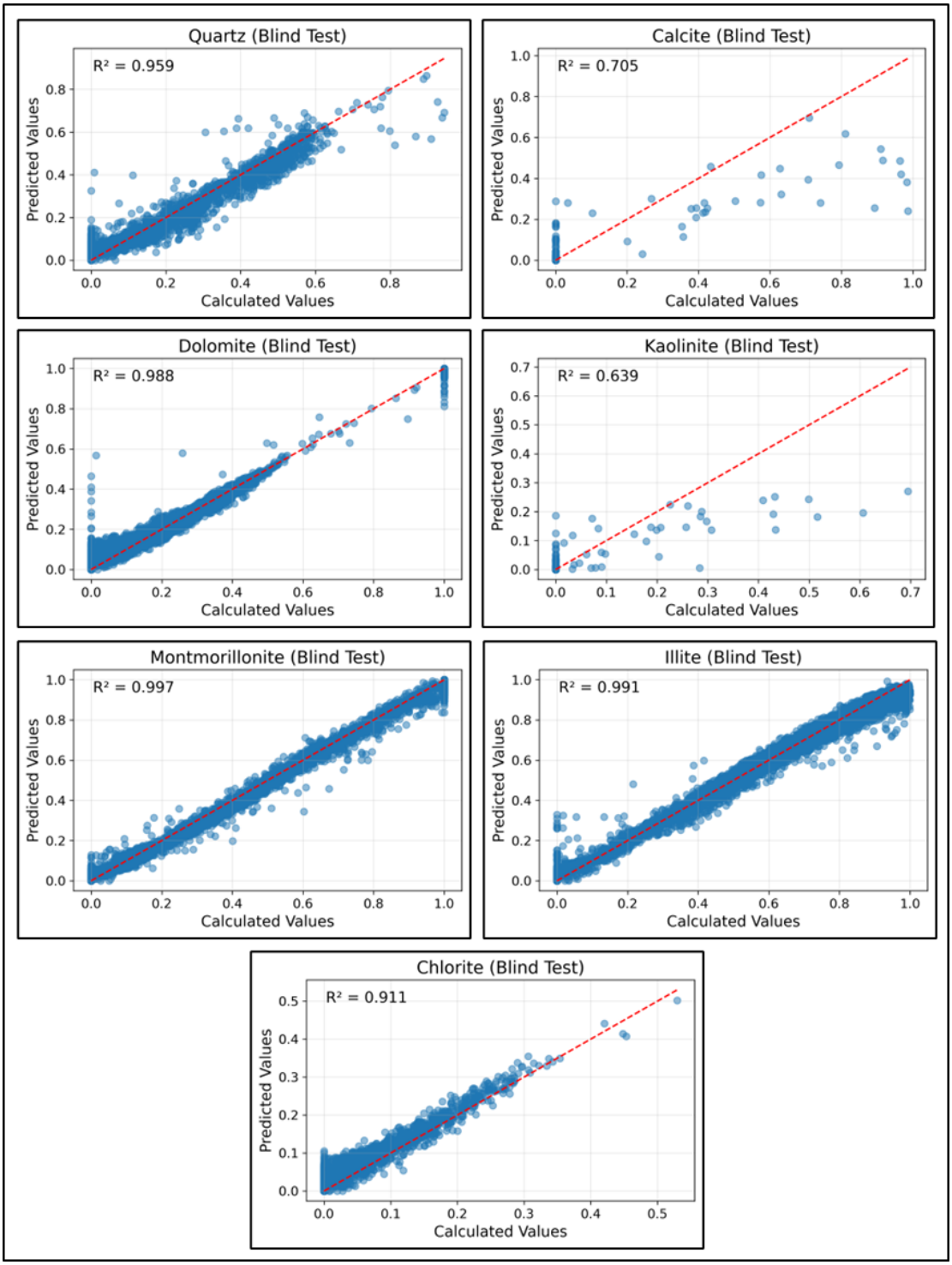

Figure 4.9 Scatter Plots of the Actual vs Predicted Mineral Composition on the X Field Dataset.

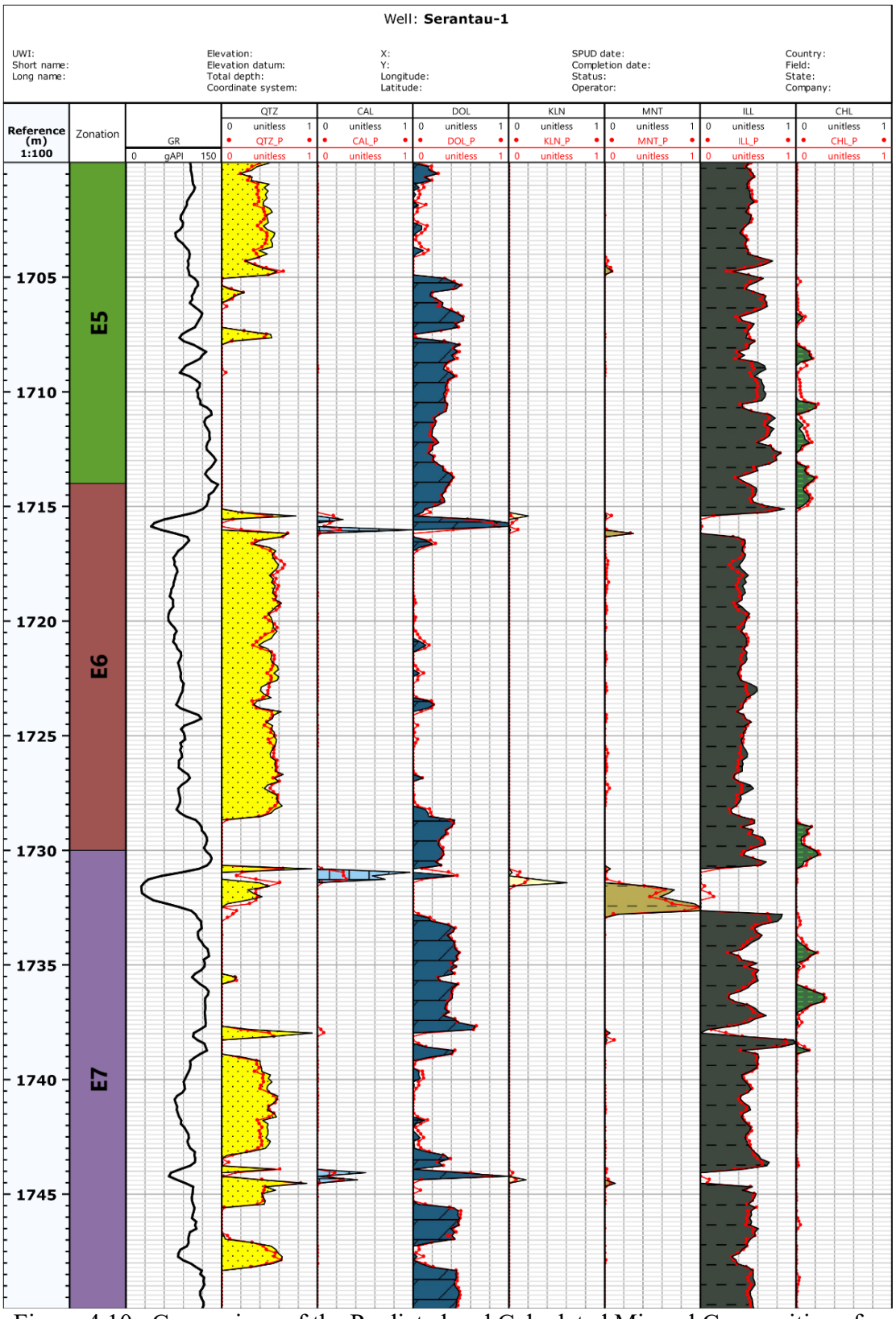

Figure 4.10 Comparison of the Predicted and Calculated Mineral Compositions for the X Field Dataset.

Collectively, the XGBoost algorithm effectively captures the nonlinear and complex relationships between mineralogical composition and well log responses in

heterogeneous formations. This finding is consistent with the results of Wang et al. (2024), who reported that XGBoost outperforms alternative methods such as random forest (RF), ridge regression (RR), support vector regression (SVR), deep learning (DL) models, and artificial neural networks (ANNs).

4.1.6 Model Limitations

In many geological formations, the most to least abundant clay mineral types are typically starting with illite/montmorillonite, chlorite, kaolinite, and followed by montmorillonite (Du et al., 2025; Hou et al., 2022). Although the dataset includes well logs from 56 formations, the mineral composition data are sparse for certain minerals such as kaolinite and chlorite, resulting in an imbalanced dataset. Consequently, the developed machine learning model may have limited capability in distinguishing among individual clay minerals. This limitation reduces the reliability of the predictions in formations where kaolinite and chlorite are dominant minerals, such as the Early Cretaceous Weald Basin in southeast England (Akinlotan et al., 2022). Although this model demonstrates strong performance in the study area, its application to other basins is necessary to further evaluate and enhance its generalisability.

4.2 3D Static Reservoir Model and Adsorption Capacity Estimation on X Field Dataset

The primary objective of the three-dimensional (3D) modelling of the X field is to evaluate CO_2 geological mineral storage by analysing the relationship between mineralogical composition and CO_2 adsorption capacity. By integrating structural, compositional, and spatial information, the model enables a detailed assessment of the interactions between mineral phases and adsorbed gases, thereby providing deeper insights into the mechanisms governing CO_2 capture and storage.

4.2.1 3D Mineralogy Model

illustrates the three-dimensional (3D) spatial distribution of minerals within the X field, which comprises quartz, calcite, dolomite, kaolinite, montmorillonite, illite, and chlorite. Figure 4.11b presents the three-dimensional (3D) mineralogy models of seven

minerals generated using a Gaussian random function simulation. The legend in the figure denotes the minimum and maximum mineral fractions and their spatial distribution within the range. This modelling utilised upscaled mineral logs derived from mineral composition data predicted by the XGBoost model.

The three-dimensional (3D) mineralogy models were subsequently integrated into the modelling workflow to construct a three-dimensional (3D) facies model. The sequential indicator simulation algorithm is particularly suitable for representing such irregular geological settings and provides a realistic characterisation of facies geometries (Heneish et al., 2025). This approach is particularly suitable for studies with limited well and mineralogical data, as our primary objective is to develop a model that characterises mineral distribution and examines the relationship between mineralogical composition and CO2 adsorption capacity.

Table 4.4 summarises the compositional breakdown of the seven minerals. The X field is dominated by clay minerals, which account for 65.29% of the total mineral composition. The remaining constituents, namely dolomite, quartz, and calcite, contribute 18.55%, 15.89%, and 0.26%, respectively. Following model development, statistical comparisons and histogram analyses were conducted to assess model reliability. Strong agreement is observed among the upscaled mineral logs, the 3D facies model, and the 3D mineralogical model across all zones.

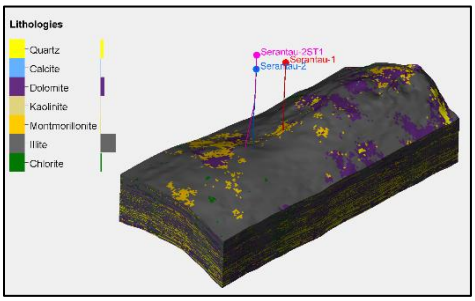

(a) Facies model

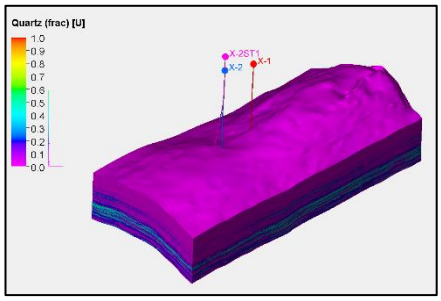

(b) Mineralogy model of quartz

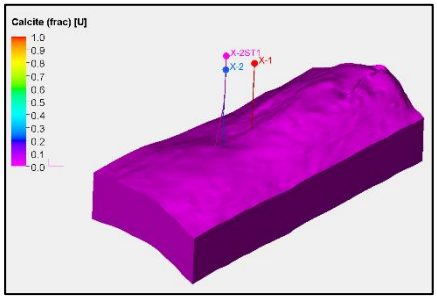

(c) Mineralogy model of calcite

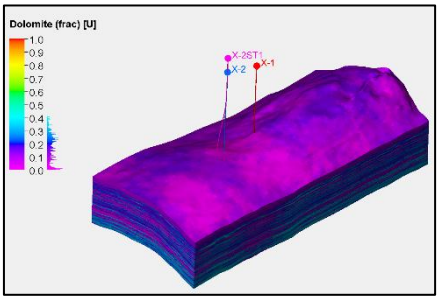

(d) Mineralogy model of dolomite

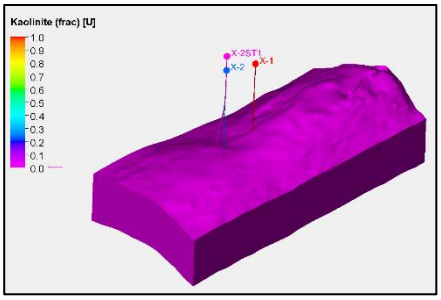

(e) Mineralogy model of kaolinite

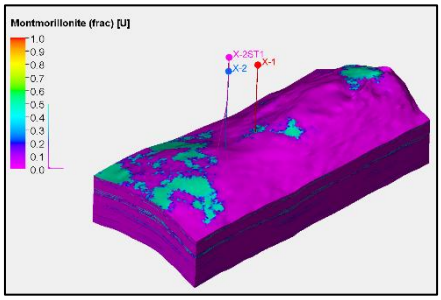

(f) Mineralogy model of montmorillonite

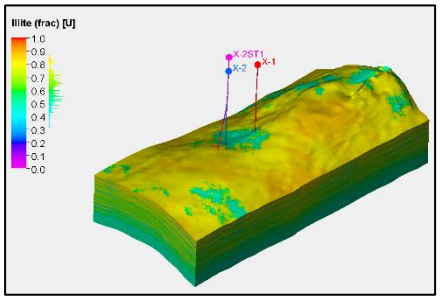

(g) Mineralogy model of illite

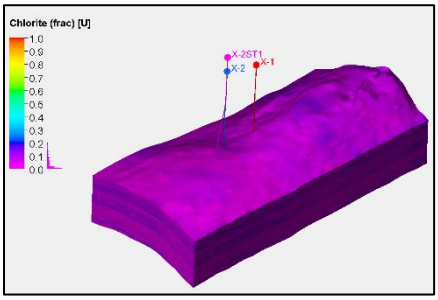

(h) Mineralogy model of chlorite

Figure 4.11 (a) 3D Facies Model of the X Field; (b)-(h)3D Mineralogy Model of the Seven Minerals.

Table 4.4
Mineral Composition of the Seven Minerals in the X Field.

Zone Name	Mineral Percentage (%)							
	QTZ	CAL	DOL	KLN	MNT	ILL	CHL	Clay Minerals
B1	0.26	0.02	9.29	0	5.69	80.82	3.92	90.43
D1	0.57	0.04	20.4	0	0.38	71.46	7.15	78.99
D2	3.96	0.02	15.96	0	10.73	66.51	2.81	80.05
D3	12.71	0.09	20.1	0	2.44	62.45	2.21	67.1
D4	13.63	0.26	21.44	0	0.53	61.25	2.87	64.65
D5	8.93	0.05	22.58	0	0.26	64.05	4.12	68.43
E1	5.74	0.05	21.57	0.04	2.51	63.19	6.89	72.63
E2	15.39	0.5	19.7	0.4	2.14	60.89	0.99	64.42
E3	32.69	0.28	8.91	0.25	1.25	55.83	0.79	58.12
E4	22.43	0.07	24.21	0	0.1	52.81	0.38	53.29
E5	16.68	1.08	23.56	0.08	0.45	54.81	3.33	58.67
E6	58.04	0.28	6.08	0.13	1.14	33.51	0.82	35.6
E7	15.56	0.66	27.36	0.52	2.7	49.79	3.42	56.43
Total	15.89	0.26	18.55	0.11	2.33	59.80	3.05	65.29

4.2.2 Analysis of the Developed 3D Facies and Mineralogy Model

Figure 4.12 indicates a comparison of the developed three-dimensional (3D) models, demonstrating that the mineralogical model is consistently mapped with the facies model. Model refinement was achieved through multiple configurations, including the selection of different variograms and simulation methods. Identifying an optimal configuration is essential to improving overall model accuracy. The facies model for quartz highlights the presence of quartz-enriched zones, particularly in the left, right, and central–upper regions of the model. These spatial trends are corroborated by the mineralogical model, which indicates elevated quartz fractions in the same areas, whereas regions with lower quartz content correspond to non-quartz lithologies.

A similar pattern is observed for dolomite. Dolomitic lithologies are predominantly distributed in the central region, with smaller occurrences on both lateral sides of the model. This distribution is consistent with zones of high dolomite fractions identified in the mineralogical model. Notably, the dolomite-rich areas spatially overlap with quartz-enriched zones.

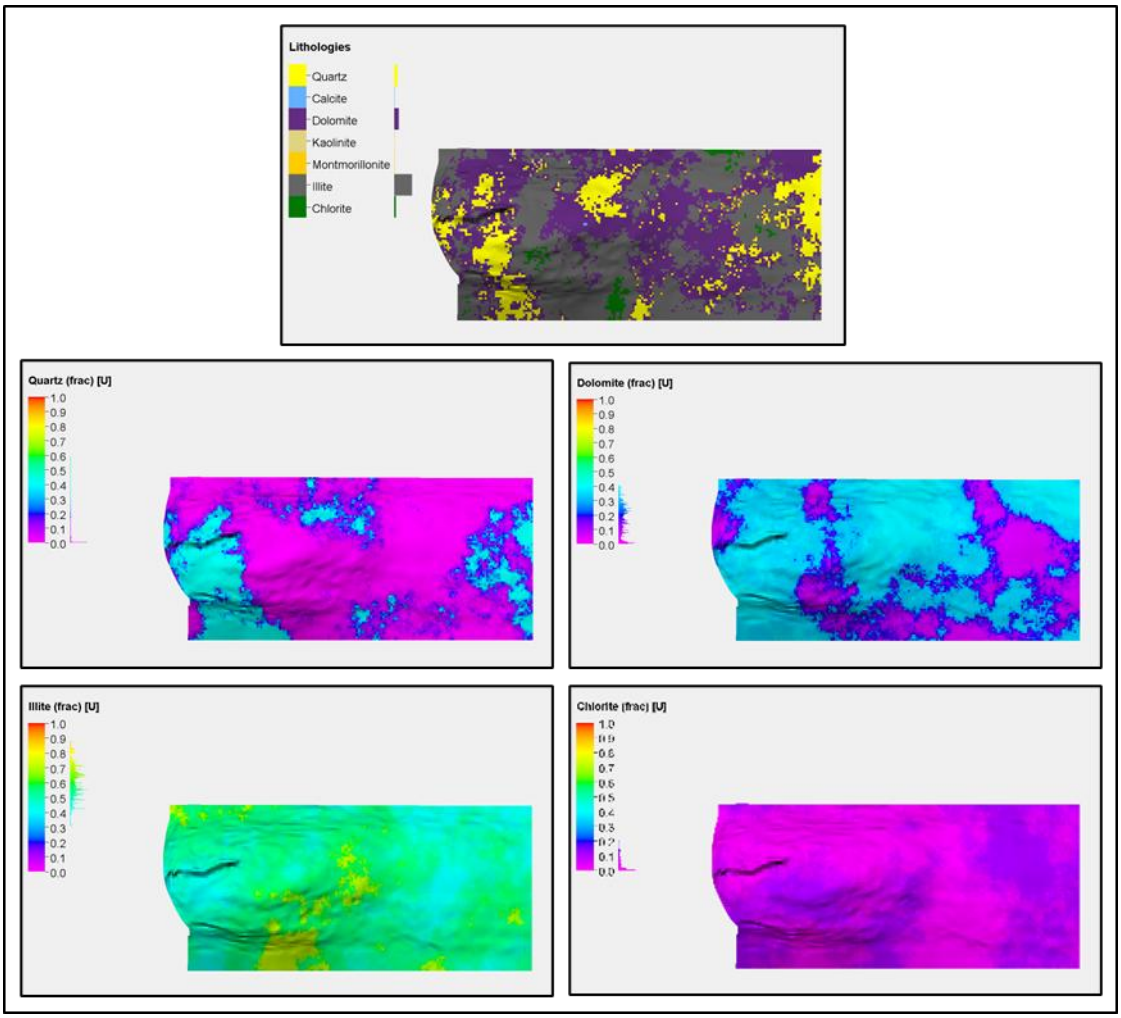

Figure 4.12 Comparison of Mineralogy Model with the Facies Model.

In the case of illite, the facies model exhibits an irregular distribution, particularly in the central and lower left areas. Consistently, the mineralogical model indicates a substantial presence of illite in these regions. The minor discrepancies between the two models can be attributed to their differing conceptual frameworks, whereby facies models classify lithologies based on dominant mineral constituents, while mineralogical models represent compositional variations as continuous fields. Unlike other phases of minerals, the distribution of chlorite is highly irregular. The facies model shows isolated patches of chlorite due to its low composition. This pattern is consistent with the mineralogical model, which indicates only minor proportions of chlorite across most of the sampled areas.

Broadly, the results show that quartz, dolomite, and illite have a high level of consistency, while the chlorite shows relatively inaccurate distribution within the model because of its low composition in the geological storage.

4.2.3 3D Adsorption Capacity Model

The developed three-dimensional (3D) adsorption capacity model provides an improved visualisation of spatial adsorption across the entire field, facilitating the identification of potential CO_2 storage sites. Using this model, the contribution of each mineral phase to the overall adsorption capacity can be explicitly evaluated.

Figure 4.13a shows the three-dimensional (3D) spatial distribution of the potential CO_2 adsorption sites of the X field after totalling up the amount of CO_2 adsorbed contributed by different minerals that are presented in Figure 4.13b. The legend indicates the minimum and maximum amounts of CO_2 that can be adsorbed. This model was constructed from the three-dimensional (3D) mineralogical model using a 3D property calculator.

Table 4.5 demonstrates the estimated values of adsorption capacity for each zone in mg/g, as well as the contribution of the adsorption capacity for specific minerals. Incorporating adsorption capacity data alongside structural trapping enhances modelling accuracy and reduces uncertainty in CO_2 storage estimates.

The three-dimensional (3D) static reservoir model helps in understanding the spatial distribution and heterogeneity of the formation, which are essential for CCS applications. It was observed that the mineralogical, geochemical, petrophysical, and geomechanical changes occurring during mineral dissolution and precipitation processes significantly influence porosity and permeability (Tibane et al., 2021).

The mineral composition plays a major role in controlling the distribution of CO_2 storage capacity. The presence and relative proportions of quartz, carbonate, and clay minerals are known to influence CO_2 adsorption behaviour. For example, formations with higher proportions of quartz or carbonate minerals, which are relatively less reactive with CO_2, tend to exhibit lower adsorption capacities compared with formations enriched in clay minerals, which show stronger reactivity and higher CO_2 adsorption potential (Al-Khdheeawi et al., 2023). By understanding how mineral composition controls the distribution of adsorption capacity, it becomes possible to identify zones of high and low CO_2 adsorption potential within the formation.

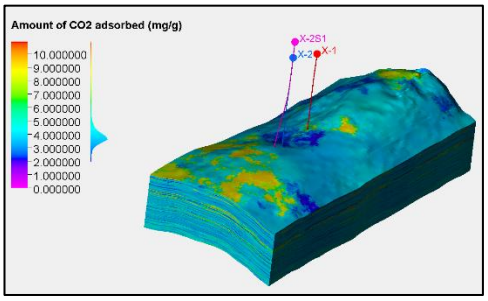

(a) CO_2 adsorbed by all minerals

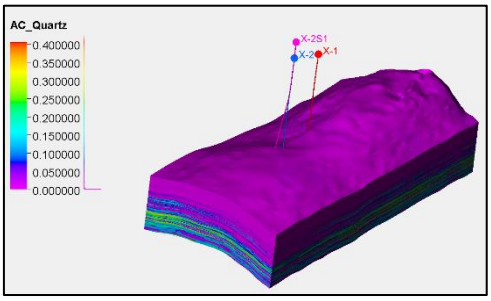

(b) CO_2 adsorbed by quartz

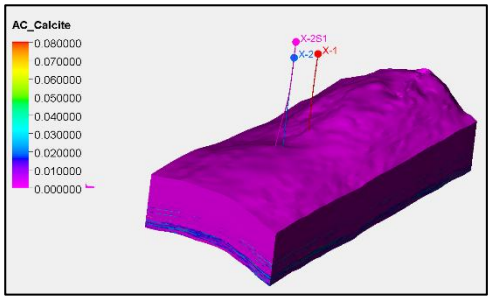

(c) CO_2 adsorbed by calcite

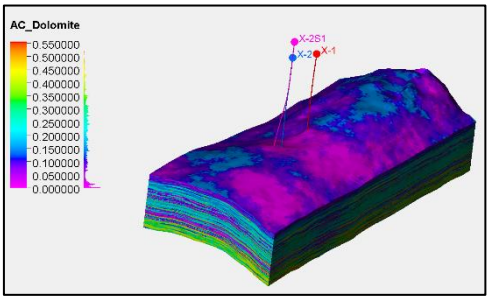

(d) CO_2 adsorbed by dolomite

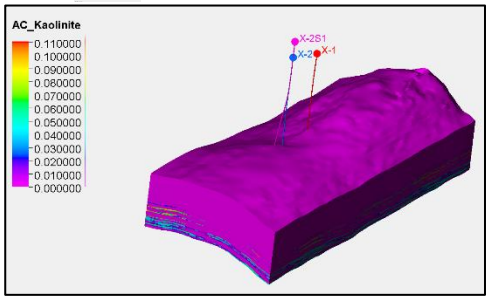

(e) CO_2 adsorbed by kaolinite

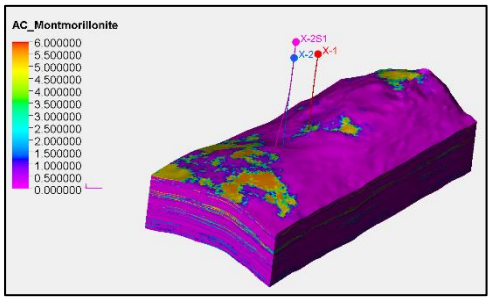

(f) CO_2 adsorbed by montmorillonite

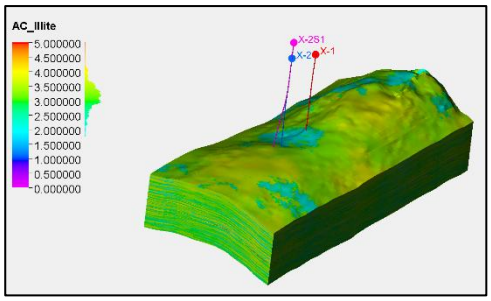

(g) CO_2 adsorbed by illite

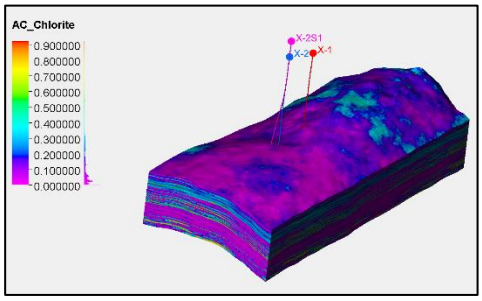

(h) CO_2 adsorbed by chlorite

Figure 4.13 (a) 3D Adsorption Capacity Model of the X Field; (b)-(h) 3D Adsorption Capacity of the Seven Minerals.

Table 4.5
Estimated Adsorption Capacity.

Zone Name	Amount of CO_2 adsorbed (mg/g)							
	QTZ	CAL	DOL	KLN	MNT	ILL	CHL	**Total**
B1	193	33	13029	0	105248	471531	21585	611619
D1	386	67	29519	1	5663	441600	40700	517935
D2	2727	45	23911	5	210574	425817	17877	680955
D3	7332	33	24381	28	30087	474530	35064	571456
D4	8434	74	26177	11	6307	467809	41142	549953
D5	5188	69	34584	38	3880	462829	34199	540787
E1	3583	173	31406	305	48953	470758	49391	604569
E2	10452	826	33367	2289	42061	459537	8734	557264
E3	26072	551	17732	1569	24783	449263	5921	525892
E4	17783	155	43678	6	1978	448351	7593	519544
E5	13229	909	45615	787	9617	443207	31156	544520
E6	39341	760	14357	1047	32775	362003	15249	465533
E7	14202	1568	48556	3179	59824	429504	32788	589621

The 3D adsorption capacity model, governed by mineralogical composition, showed a heterogeneous distribution across the formation. Clay minerals dominated the entire X field. In terms of CO_2 storage, the mineral-specific quantification, specifically for clay minerals, acts as an indicator that increases the amount of CO_2 adsorbed. Neglecting the mineral-specific interaction may result in an underestimation of the reactive surface area and thereby influence the accuracy of the potential CO_2 storage capacity (Eid et al., 2025b).

Despite the expected increase in the accuracy of CO_2 storage capacity estimation resulting from 3D modelling, serious uncertainties remain (Eid et al., 2025b). A preliminary model based solely on the areal extent of the formation and estimated mineral composition and adsorption capacity may be acceptable for initial screening. However, such estimates depend on strong assumptions and can result in substantial discrepancies. In this study, uncertainties in mineralogical modelling primarily arise from the absence of core data and the limited availability of well log data, while uncertainties in adsorption capacity modelling are associated with variability in adsorption isotherms under different pressure and temperature conditions. To address these uncertainties, variations in 3D static modelling were applied to provide a more comprehensive assessment of CO_2 storage under multiple scenarios. This approach enables the estimation of spatial variations in CO_2 adsorption both laterally and

vertically within the formation, thereby improving risk-informed decision-making for carbon capture and storage applications.

In conclusion, the combined evaluation of mineral-specific adsorption capacity confirms the strong potential of this approach for CO_2 storage. This study demonstrates that the model can identify the mineral phases that contribute most significantly to adsorption capacity and accurately represent their spatial distribution, which can be used to indicate favourable storage zones. For example, the results show that zones characterised by a higher proportion of clay minerals with larger reactive surface areas exhibit greater CO_2 adsorption compared with zones dominated by quartz and carbonate minerals, which have lower reactive surface areas. When integrated with 3D static reservoir models, mineral-specific adsorption capacity models clearly highlight the critical role of mineralogical composition in adsorption behaviour, thereby supporting the optimisation of CO_2 injection strategies, including injection rates, well placement, and overall storage design.

4.3 Simulation of the CO_2 Storage Performance

The developed model enables the simulation of CO_2 adsorption as a function of pressure and temperature. To evaluate the effects of these parameters on adsorption capacity, nine combinations of pressure and temperature were considered, all under supercritical CO_2 conditions, while the adsorption coefficient was held constant. Variations in CO_2 adsorption capacity with pressure and temperature arise from multiple interacting factors, including changes in gas density, thermal agitation, mineral surface affinity, pore structure, and adsorption isotherm behaviour, which are inherently complex to quantify in detail. For clarity, this study focuses on illustrating the relationship between pressure and temperature and their combined influence on CO_2 adsorption capacity, thereby capturing their dominant impact on CO_2 storage performance.

Figure 4.14 presents a graphical representation of the CO_2 adsorption capacity based on the nine groups of input parameters, pressures and temperatures. Figure 4.14 Additionally, Figure 4.15 shows the relationship between pressures and temperatures, and the amount of CO_2 adsorbed. The amount of CO_2 adsorbed under the nine pressure–temperature conditions increases progressively with increasing pressure and temperature, as theoretically expected. Although higher pressure leads to greater CO_2

adsorption, the rate of increase gradually diminishes under supercritical conditions, consistent with typical adsorption isotherm behaviour. The model shows the phenomenon that normally happens, aligned with the research by S.-J. Han et al. (2022) Given the spatial distribution of CO_2 adsorption capacity within the entire study area, both pressure and temperature play important roles in the estimation of CO_2 storage capacity, particularly critical in a depleted reservoir.

The synergistic evaluation of adsorption capacity under varying temperatures and pressures is critical for CO_2 storage strategies. Under supercritical conditions, CO_2 is hypothesised to exhibit non-linear behaviour, with adsorption rates becoming highly sensitive to changes in bulk density and mineral–CO_2 interactions, both of which vary spatially throughout the reservoir (Z. Sun et al., 2023). The simulation allows for imaging the spatial distribution of CO_2 storage throughout the reservoir conditions, ensuring an accurate estimation. In addition, accurate simulation of pressure and temperature profiles is essential for monitoring operations in carbon capture and storage projects, particularly for targeting zones where storage performance is expected to be most effective (Shi et al., 2024). The inclusion of the 3D model in the CO_2 storage strategies indirectly assists in reducing the risk of overpressure and leakage probability, thus ensuring safer and more effective CO_2 storage (Hao et al., 2021).

On the whole, this modelling approach is far more accurate than the standard ways of estimating the CO_2 storage capacity as it helps to simulate temperature and pressure behaviours on the CO_2 adsorption capacity, and as such, minimises uncertainties in CCS application. It enables a closer insight into an adsorption trapping mechanism at real P-T conditions, and risk-informed decision-making, as well as enhances confidence in the long-term security and viability of geological CO_2 storage.

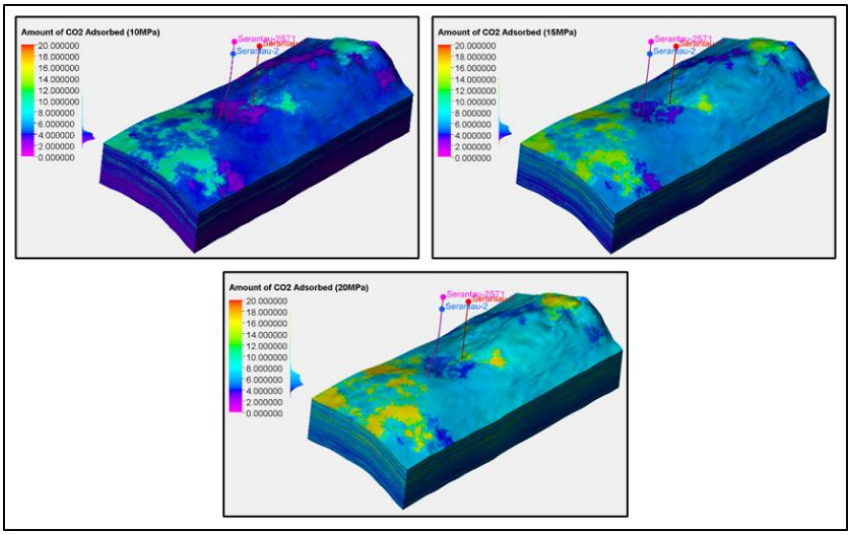

(a) At 303.15K

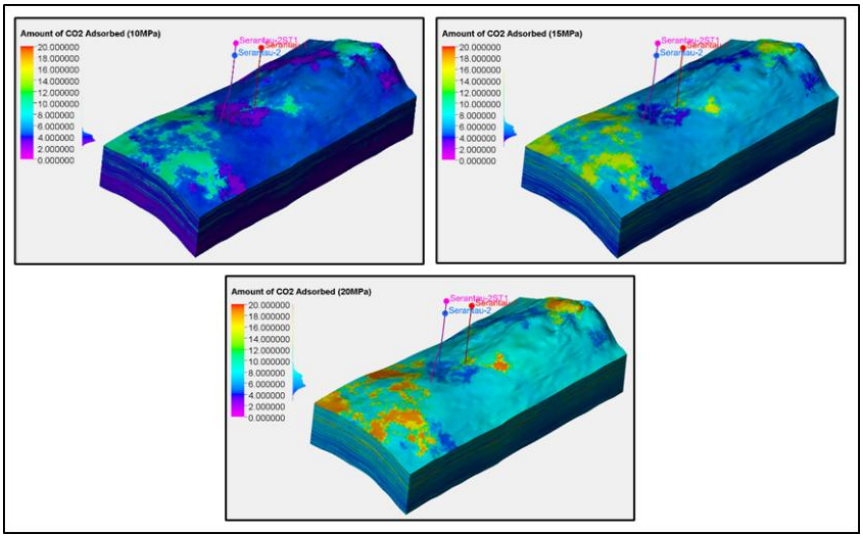

(b) At 353.15K

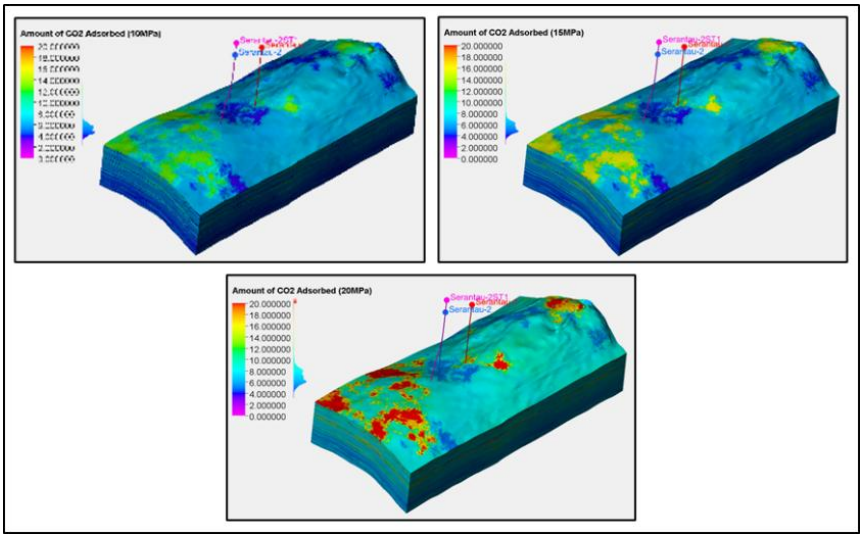

(c) At 393.15K

Figure 4.14 CO_2 Adsorption Capacity at Pressures of 10, 15, and 20 MPa under Temperature Conditions of (a) 303.15 K, (b) 353.15 K, and (c) 393.15 K.

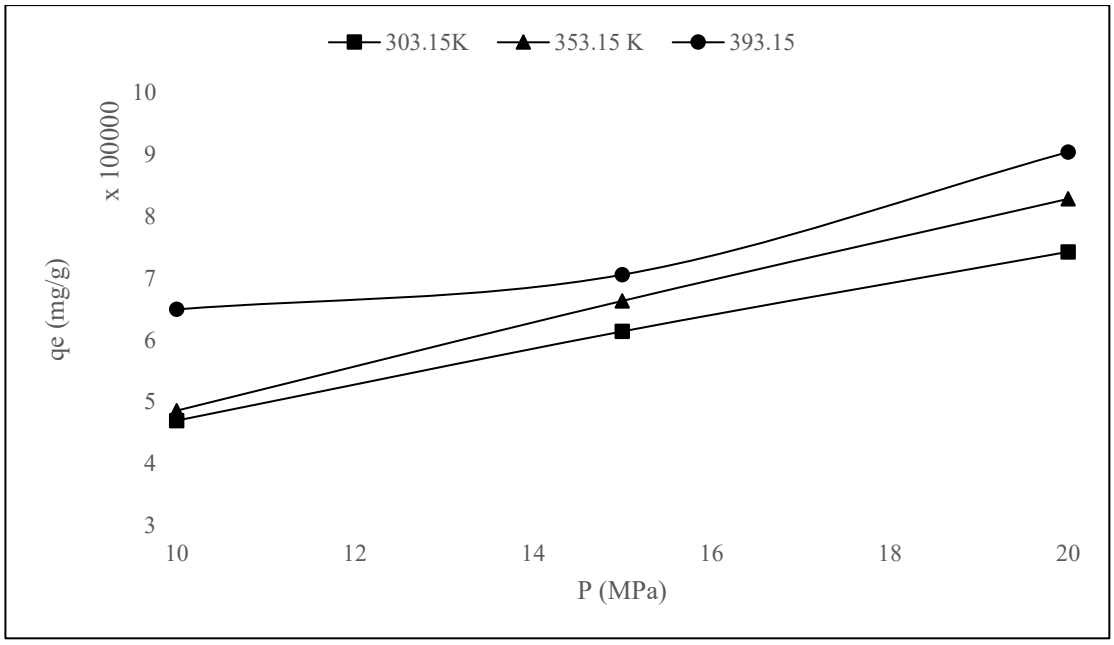

Figure 4.15 Correlation on the Variation of Pressure and Temperature with the Amount of CO_2 Adsorbed.

CHAPTER 5
CONCLUSION AND RECOMMENDATION

5.1 Conclusion

A three-dimensional (3D) static reservoir model of CO_2 adsorption capacity across different mineral phases was developed under varying pressure and temperature conditions. By constructing multiple three-dimensional (3D) mineralogical and adsorption capacity models and performing numerical simulations based on conventional well log data from the X field, this study captures spatial variations that elucidate the relationship between mineralogical composition and adsorption behaviour. These results provide valuable insight for large-scale, early-stage evaluation of CO_2 geological storage potential. The conclusions drawn in relation to the research objectives are presented below:

1. In the absence of core data and with limited well log information, an XGBoost model was successfully developed to predict mineral composition from conventional well logs, using mineral composition estimates derived from the simultaneous equation method as training targets. The trained model was subsequently applied to the X field. The model demonstrates strong predictive performance, achieving an MAE of 0.009, an RMSE of 0.021, and an R^2 value of 0.884. The predicted mineral compositions closely match those obtained from the simultaneous equation method, indicating a reasonable level of generalisability across different basins. Nevertheless, model performance remains sensitive to data variability and availability.
2. This research successfully developed a three-dimensional (3D) static reservoir model of CO_2 adsorption capacity based on a three-dimensional (3D) mineralogical framework. The mineralogical model was constructed using mineral composition predictions derived from the X field dataset and subsequently employed to generate a three-dimensional (3D) adsorption capacity model through a three-dimensional (3D) property calculator. The resulting model captures spatial variations in CO_2 adsorption that directly reflect the underlying mineral distribution. According to the model results, clay-dominated zones exhibit higher CO_2 adsorption than intervals

dominated by quartz, calcite, or dolomite. The model, therefore, identifies the mineral phases that contribute most significantly to adsorption capacity and provides a reliable representation of mineral distribution that can be used to indicate favourable CO_2 storage zones.

3. The developed three-dimensional (3D) adsorption capacity model was successfully simulated at various pressures and temperatures. During the simulation, nine groups of different pressures and temperatures are created in total, notably supercritical CO_2 conditions. The results indicate that the amount of CO_2 adsorbed increases progressively with increasing pressure and temperature. However, although higher pressure enhances overall adsorption, the adsorption rate gradually decreases under supercritical conditions, consistent with adsorption isotherm behaviour (S.-J. Han et al., 2022). Consequently, the simulation enables the identification of reservoir pressure and temperature conditions that are most favourable for maximising CO_2 adsorption capacity. Furthermore, the results provide a meaningful basis for visualising the spatial distribution of CO_2 storage throughout the reservoir, thereby improving estimation accuracy and reducing uncertainty in identifying optimal CO_2 storage zones.

In conclusion, the three-dimensional (3D) static reservoir model effectively visualises the spatial distribution of CO_2 adsorption capacity across the reservoir. Incorporating this three-dimensional (3D) modelling approach into CO_2 storage strategies can indirectly reduce the risks of overpressure and leakage, thereby supporting safer and more effective carbon capture and storage applications.

5.2 Recommendation

This research demonstrates the effectiveness of using conventional well log data for mineral composition prediction and its subsequent application in constructing a three-dimensional (3D) adsorption capacity model. Nevertheless, there remains scope for further improvement and refinement in future studies. Based on the machine learning prediction results, dataset imbalance may constrain model performance. Addressing this limitation requires diversification of the training data through careful selection of well logs that better represent minerals that were previously underrepresented. Incorporating these additional logs into the training dataset can help

balance mineral class distributions, improve model generalisability, and ultimately enhance prediction accuracy.

For further improvement of the machine learning model, future research should incorporate datasets from multiple geological settings and depositional environments to enhance the generalisation capability. In addition, future studies may integrate a more comprehensive range of well log datasets, including gamma ray (GR), resistivity, photoelectric factor (PEF), nuclear magnetic resonance (NMR), and other advanced petrophysical logs.

Seismic data, Xray-diffraction (XRD), Fourier Transform Infrared Spectroscopy (FTIR) and Scanning Electron Microscopy (SEM) could also be incorporated to provide additional mineralogical, chemical, pore structure and stratigraphic information to validate the machine learning model. These validation methods may improve the accuracy of mineral prediction by providing ground-truth laboratory measurements and reducing uncertainties.

This research confirms the feasibility of developing three-dimensional (3D) mineralogical and static reservoir models for CO_2 adsorption capacity. However, the current framework should be extended toward more detailed and fully dynamic simulations. Internal processes related to chemistry, physics, and geomechanics require more comprehensive investigation in future work. In addition, integration with advanced simulation platforms is recommended to better capture mineral reactions and assess long-term storage integrity. For example, OpenGeoSys is widely used to simulate time-dependent mineral transformations and coupled thermos-hydro-mechanical-chemical processes (Poonoosamy et al., 2021). The application of this software in future research is expected to support more informed and reliable decision-making in the evaluation of CO_2 geological storage.

REFERENCES

Abudeif, A. M., Mohammed, M. A., Masoud, M. M., Radwan, A. E., Alarifi, N., Bellucci, S., & Tawfik, F. A. (2025). Influence of Shale on Petrophysical Properties and Reservoir Quality: Insights from the Matulla Formation, Saqqara Field, Gulf of Suez, Egypt. *Pure and Applied Geophysics*, *182*(7), 2799–2820. https://doi.org/10.1007/s00024-025-03711-4

Abunowara, M., Bustam, M. A., Sufian, S., Babar, M., Eldemerdash, U., Mukhtar, A., Ullah, S., Assiri, M. A., Al-Sehemi, A. G., & Lam, S. S. (2023). High pressure CO2 adsorption onto Malaysian Mukah-Balingian coals: Adsorption isotherms, thermodynamic and kinetic investigations. *Environmental Research*, *218*, 114905. https://doi.org/10.1016/j.envres.2022.114905

Afolayan, B. A., Mackay, E., & Opuwari, M. (2023). 3D Static Modeling and CO2 Static Storage Estimation of the Hydrocarbon-Depleted Charis Reservoir, Bredasdorp Basin, South Africa. *Natural Resources Research*, *32*(3), 1021–1045. https://doi.org/10.1007/s11053-023-10180-w

Aghajanloo, M., Yan, L., Berg, S., Voskov, D., & Farajzadeh, R. (2024). Impact of CO2 hydrates on injectivity during CO2 storage in depleted gas fields: A literature review. *Gas Science and Engineering*, *123*, 205250. https://doi.org/10.1016/j.jgsce.2024.205250

Ahmad, S. (2025). Mineralogical and textural controls on the mechanical behavior of sandstones from the Nizampur and Kohat Basinds, Pakistan. *Acta Geodynamica et Geomaterialia*, 485. https://doi.org/10.13168/AGG.2025.0035

Akinlotan, O. O., Moghalu, O. A., Hatter, S. J., Okunuwadje, S., Anquilano, L., Onwukwe, U., Haghani, S., Anyiam, O. A., & Jolly, B. A. (2022). Clay mineral formation and transformation in non-marine environments and implications for Early Cretaceous palaeoclimatic evolution: The Weald Basin, Southeast England. *Journal of Palaeogeography*, *11*(3), 387–409. https://doi.org/10.1016/j.jop.2022.04.002

Akpasi, S. O., & Isa, Y. M. (2022). Effect of operating variables on CO2 adsorption capacity of activated carbon, kaolinite, and activated carbon – kaolinite composite adsorbent. *Water-Energy Nexus*, *5*, 21–28. https://doi.org/10.1016/j.wen.2022.08.001

Alafnan, S., Awotunde, A., Glatz, G., Adjei, S., Alrumaih, I., & Gowida, A. (2021). Langmuir adsorption isotherm in unconventional resources: Applicability and limitations. *Journal of Petroleum Science and Engineering*, *207*, 109172. https://doi.org/10.1016/j.petrol.2021.109172

Alaqarbeh, M. (2021). *Adsorption Phenomena: Definition, Mechanisms, and Adsorption Types: Short Review*. *13*, 43–51. https://doi.org/10.48419/IMIST.PRSM/rhazes-v13.28283

Alberti, G., Amendola, V., Pesavento, M., & Biesuz, R. (2012). Beyond the synthesis of novel solid phases: Review on modelling of sorption phenomena. *Coordination Chemistry Reviews*, *256*(1–2), 28–45. https://doi.org/10.1016/j.ccr.2011.08.022

Al-Ghouti, M. A., & Da'ana, D. A. (2020). Guidelines for the use and interpretation of adsorption isotherm models: A review. *Journal of Hazardous Materials*, *393*, 122383. https://doi.org/10.1016/j.jhazmat.2020.122383

Ali, A., Chiang, Y. W., & Santos, R. M. (2022). X-ray Diffraction Techniques for Mineral Characterization: A Review for Engineers of the Fundamentals, Applications, and Research Directions. *Minerals*, *12*(2), 205. https://doi.org/10.3390/min12020205

Al-Khdheeawi, E. A., Mahdi, D. S., Yuan, Y., & Iglauer, S. (2023). Influence of Clay Content on CO2-Rock Interaction and Mineral-Trapping Capacity of Sandstone Reservoirs. *Energies*, *16*(8), 3489. https://doi.org/10.3390/en16083489

AL-khulaidi, G., Sun, Y., Alareqi, Ahmed. G., Ibrahim, A.-W., Magaji, A., & Zhang, X. (2024). Review on Carbon Capture, Utilization, and Storage for Enhancing Gas Recovery. *Energy & Fuels*, *38*(10), 8355–8384. https://doi.org/10.1021/acs.energyfuels.3c05211

Amjad, M., Ahmad, I., Ahmad, M., Wróblewski, P., Kamiński, P., & Amjad, U. (2022). Prediction of Pile Bearing Capacity Using XGBoost Algorithm: Modeling and Performance Evaluation. *Applied Sciences*, *12*(4), 2126. https://doi.org/10.3390/app12042126

Andrew Emuobosa Esiri, Dazok Donald Jambol, & Chinwe Ozowe. (2024). Best practices and innovations in carbon capture and storage (CCS) for effective CO2 storage. *International Journal of Applied Research in Social Sciences*, *6*(6), 1227–1243. https://doi.org/10.51594/ijarss.v6i6.1212

Aquino, T. F. de, Estevam, S. T., Viola, V. O., Marques, C. R. M., Zancan, F. L., Vasconcelos, L. B., Riella, H. G., Pires, M. J. R., Morales-Ospino, R., Torres, A. E. B., Bastos-Neto, M., & Cavalcante, C. L. (2020). CO2 adsorption capacity of zeolites synthesized from coal fly ashes. *Fuel*, *276*, 118143. https://doi.org/10.1016/j.fuel.2020.118143

Asante-Okyere, S., Ziggah, Y. Y., & Marfo, S. A. (2021). Improved total organic carbon convolutional neural network model based on mineralogy and geophysical well log data. *Unconventional Resources*, *1*, 1–8. https://doi.org/10.1016/j.uncres.2021.04.001

Ayodele, O. L., Chatterjee, T. K., & Opuwari, M. (2021). Static reservoir modeling using stochastic method: a case study of the cretaceous sequence of Gamtoos Basin, Offshore, South Africa. *Journal of Petroleum Exploration and Production Technology*, *11*(12), 4185–4200. https://doi.org/10.1007/s13202-021-01306-y

Baban, A., Keshavarz, A., Amin, R., & Iglauer, S. (2023). Residual Trapping of CO2 and Enhanced Oil Recovery in Oil-Wet Sandstone Core – A Three-Phase Pore-Scale Analysis Using NMR. *Fuel*, *332*, 126000. https://doi.org/10.1016/j.fuel.2022.126000

Babikir, I., Elsaadany, M., Sajid, M., & Laudon, C. (2022). Evaluation of principal component analysis for reducing seismic attributes dimensions: Implication for supervised seismic facies classification of a fluvial reservoir from the Malay Basin, offshore Malaysia. *Journal of Petroleum Science and Engineering*, *217*, 110911. https://doi.org/10.1016/j.petrol.2022.110911

Badejo, S. A., Fraser, A. J., Neumaier, M., Muxworthy, A. R., & Perkins, J. R. (2021). 3D petroleum systems modelling as an exploration tool in mature basins: A study from the Central North SeaUK. *Marine and Petroleum Geology*, *133*, 105271. https://doi.org/10.1016/j.marpetgeo.2021.105271

Bashir, A., Ali, M., Patil, S., Aljawad, M. S., Mahmoud, M., Al-Shehri, D., Hoteit, H., & Kamal, M. S. (2024). Comprehensive review of CO2 geological storage: Exploring principles, mechanisms, and prospects. *Earth-Science Reviews*, *249*, 104672. https://doi.org/10.1016/j.earscirev.2023.104672

Beckhoff, B., Kanngießer, B., Langhoff, N., Wedell, R., & Wolff, H. (2007). *Handbook of Practical X-Ray Fluorescence Analysis*. Springer Berlin Heidelberg. https://books.google.com.my/books?id=c6d8EPYHn1EC

Bhattacharya, S. (2022). Unsupervised time series clustering, class-based ensemble machine learning, and petrophysical modeling for predicting shear sonic wave slowness in heterogeneous rocks. *Geophysics*, *87*(5), D161–D174. https://doi.org/10.1190/geo2021-0478.1

Bigelow, E. L., & Inc, B. H. (2002). *Introduction to Wireline Log Analysis*. Baker Hughes. https://books.google.com.my/books?id=epaTQwAACAAJ

Biswas, S., Mohapatra, S. S., Kumari, U., Meikap, B. C., & Sen, T. K. (2020). Batch and continuous closed circuit semi-fluidized bed operation: Removal of MB dye using sugarcane bagasse biochar and alginate composite adsorbents. *Journal of Environmental Chemical Engineering*, *8*(1), 103637. https://doi.org/10.1016/j.jece.2019.103637

Bø Hunvik, K. W., Loch, P., Wallacher, D., Kirch, A., Cavalcanti, L. P., Rieß, M., Daab, M., Josvanger, V., Grätz, S., Yokaichiya, F., Knudsen, K. D., Rodrigues Miranda, C., Breu, J., & Fossum, J. O. (2021). CO $_2$ Adsorption Enhanced by Tuning the

Layer Charge in a Clay Mineral. *Langmuir*, *37*(49), 14491–14499. https://doi.org/10.1021/acs.langmuir.1c02467

Boetcher, S. K. S., Perskin, J. B., Maidenberg, Y., Traum, M. J., & von Hippel, T. (2023). Direct atmospheric cryogenic carbon capture in cold climates. *Carbon Capture Science & Technology*, *8*, 100127. https://doi.org/10.1016/j.ccst.2023.100127

Cao, C., Liu, H., Hou, Z., Mehmood, F., Liao, J., & Feng, W. (2020). A Review of CO2 Storage in View of Safety and Cost-Effectiveness. *Energies*, *13*(3), 600. https://doi.org/10.3390/en13030600

Cao, X., Liu, Z., Hu, C., Song, X., Quaye, J. A., & Lu, N. (2024). Three-Dimensional Geological Modelling in Earth Science Research: An In-Depth Review and Perspective Analysis. *Minerals*, *14*(7), 686. https://doi.org/10.3390/min14070686

Chang, C. I. (2003). *Hyperspectral Imaging: Techniques for Spectral Detection and Classification* (Number v. 1). Springer US. https://books.google.com.my/books?id=JhBbXwFaA6sC

Chang, Y., Yao, Y., Wang, L., & Zhang, K. (2024). High-Pressure adsorption of supercritical methane and carbon dioxide on Coal: Analysis of adsorbed phase density. *Chemical Engineering Journal*, *487*, 150483. https://doi.org/10.1016/j.cej.2024.150483

Chen, C., Gu, Y., Zhang, D., Wu, T., Li, A., Ren, Y., Shang, Q., Zhang, J., Bian, X., Su, F., Yang, J., Sun, Q., Li, X., Liu, W., Sun, Z., Zhang, S., & Feng, Y. (2024). Geology and mineralization of the Hongqiling large magmatic nickel-copper-cobalt deposit (22×10^4 t) in Jilin Province, China: A review. *China Geology*, *7*(4), 762–796. https://doi.org/10.31035/cg2023106

Chen, C., Tang, Y., & Guo, X. (2022). Comparison of structural characteristics of high-organic-sulfur and low-organic-sulfur coal of various ranks based on FTIR and Raman spectroscopy. *Fuel*, *310*, 122362. https://doi.org/10.1016/j.fuel.2021.122362

Chen, G., Chen, M., Hong, G., Lu, Y., Zhou, B., & Gao, Y. (2020). A New Method of Lithology Classification Based on Convolutional Neural Network Algorithm by Utilizing Drilling String Vibration Data. *Energies*, *13*(4), 888. https://doi.org/10.3390/en13040888

Chen, Z. (2025). Challenges and opportunities of CO2 storage in depleted shallow gas reservoirs in Alberta Oilsands area, Western Canada Sedimentary Basin, Canada. *Fuel*, *381*, 133384. https://doi.org/10.1016/j.fuel.2024.133384

Chuka Anthony Arinze, Izionworu, V. O., Daniel Isong, Cosmas Dominic Daudu, & Adedayo Adefemi. (2024). Integrating artificial intelligence into engineering processes for improved efficiency and safety in oil and gas operations. *Open*

Access Research Journal of Engineering and Technology, *6*(1), 039–051. https://doi.org/10.53022/oarjet.2024.6.1.0012

Chunmei, L., Furong, W., Dianguang, Z., Cai, P., Hongxi, G., & Jie, L. (2023). Logging-based assessment of low-resistivity oil zones: A case study from Sudan. *Energy Geoscience*, *4*(2), 100079. https://doi.org/10.1016/j.engeos.2021.11.005

Cremers, D. A., & Radziemski, L. J. (2013). *Handbook of Laser-Induced Breakdown Spectroscopy*. Wiley. https://books.google.com.my/books?id=O4kAmW60RcsC

Cui, Q., Yang, H., Li, X., & Lu, Y. (2022). Identification of lithofacies and prediction of mineral composition in shales – A case study of the Shahejie Formation in the Bozhong Sag. *Unconventional Resources*, *2*, 72–84. https://doi.org/10.1016/j.uncres.2022.09.002

Da Silveira, J. R. B., De Figueiredo, J. J. S., Lima, C. R. L., Gonçalvez, J. F. V., & Do Amaral, M. L. (2024). S-wave log construction through semi-supervised regression clustering using machine learning: A case study of North Sea fields. *Journal of Applied Geophysics*, *229*, 105476. https://doi.org/10.1016/j.jappgeo.2024.105476

Dai, X., Wei, C., Wang, M., Zhang, J., Wang, X., Shi, X., & Vandeginste, V. (2023). Understanding CO2 mineralization and associated storage space changes in illite using molecular dynamics simulation and experiments. *Energy*, *283*, 128467. https://doi.org/10.1016/j.energy.2023.128467

Das, R. S., & Agrawal, Y. K. (2011). Raman spectroscopy: Recent advancements, techniques and applications. *Vibrational Spectroscopy*, *57*(2), 163–176. https://doi.org/10.1016/j.vibspec.2011.08.003

Daya Sagar, B. S., Cheng, Q., & Agterberg, F. (Eds.). (2018). *Handbook of Mathematical Geosciences*. Springer International Publishing. https://doi.org/10.1007/978-3-319-78999-6

de Jonge-Anderson, I., Ramachandran, H., Widyanita, A., Busch, A., Doster, F., & Nicholson, U. (2025). Regional screening of saline aquifers in the Malay Basin for CO2 storage. *International Journal of Greenhouse Gas Control*, *143*, 104347. https://doi.org/10.1016/j.ijggc.2025.104347

de Oliveira, L. A. B., Custódio, L. F. N., Fagundes, T. B., Ulsen, C., & Carneiro, C. de C. (2021). Stepped machine learning for the development of mineral models: Concepts and applications in the pre-salt reservoir carbonate rocks. *Energy and AI*, *3*, 100050. https://doi.org/10.1016/j.egyai.2021.100050

Deng, Y., Yang, Y., & Yang, T. (2025). Three systems of the oil and gas formation in the world. *Petroleum Research*, *10*(1), 1–27. https://doi.org/10.1016/j.ptlrs.2024.06.008

Djoï, A. N. (2024). Statistical Approach to Gamma Ray Signature of Clean Shales, Limestones and Sandstones: Case Study of Benin's Offshore Coastal Sedimentary Basin. *International Journal of Geoscience, Engineering and Technology*, *10*(1), 1–8. https://doi.org/10.70597/ijget.v10i1.541

Du, X.-Y., Jin, Z.-J., Zeng, L.-B., Liu, G.-P., Li, S.-X., Ostadhassan, M., Liang, X.-P., Wang, G.-P., & Lu, G.-Q. (2025). Characteristics, controlling factors and mechanisms of natural fractures formation in lacustrine shale oil reservoirs: The Chang 7 member in Ordos Basin, China. *Petroleum Science*, *22*(4), 1391–1406. https://doi.org/10.1016/j.petsci.2025.03.005

Duan, X., Hu, Z., Gao, S., Shen, R., Liu, H., Chang, J., & Wang, L. (2018). Shale high pressure isothermal adsorption curve and the production dynamic experiments of gas well. *Petroleum Exploration and Development*, *45*(1), 127–135. https://doi.org/10.1016/S1876-3804(18)30012-0

Eid, A. M., Mabrouk, W. M., Amer, M., & Metwally, A. (2023). 3D structural modeling using seismic data and well logs for Khatatba reservoir in Matruh-Shushan Basin, North Western Desert, Egypt. *Scientific Reports*, *13*(1), 20158. https://doi.org/10.1038/s41598-023-47487-w

Eid, A. M., Mabrouk, W. M., Amer, M., & Metwally, A. (2025a). Detailed petrophysical analysis and insights into the Alam El Bueib 3E reservoir from the berenice field, Western desert, Egypt. *Scientific Reports*, *15*(1), 29595. https://doi.org/10.1038/s41598-025-14708-3

Eid, A. M., Mabrouk, W. M., Amer, M., & Metwally, A. (2025b). Reservoir modeling of heterogeneities, structures, and petrophysical properties of the Berenice Oil Field: Implications for sustainable management and CO2 storage in the North Western Desert, Egypt. *Marine and Petroleum Geology*, *180*, 107466. https://doi.org/10.1016/j.marpetgeo.2025.107466

El Sharawy, M. S., & Nabawy, B. S. (2018). The role of gamma-ray logs in deciphering geochemical and geological aspects of the Rudeis Formation, Gulf of Suez, Egypt. *Arabian Journal of Geosciences*, *11*(10), 242. https://doi.org/10.1007/s12517-018-3560-0

El-Bagoury, M. (2020). Integrated petrophysical study to validate water saturation from well logs in Bahariya Shaley Sand Reservoirs, case study from Abu Gharadig Basin, Egypt. *Journal of Petroleum Exploration and Production Technology*, *10*(8), 3139–3155. https://doi.org/10.1007/s13202-020-00969-3

Ellis, D. V., & Singer, J. M. (2007). Clay Quantification. In *Well Logging for Earth Scientists* (pp. 597–627). Springer Netherlands. https://doi.org/10.1007/978-1-4020-4602-5_21

El-Masry, J., Gomaa, I., Heidari, Z., & Maalouf, E. (2025, May 17). Quantification of Mechanical Integrity of Clay Minerals in Clay-Rich Rocks Under CO2 Geological

Storage. *SPWLA 66th Annual Symposium Transactions*. https://doi.org/10.30632/SPWLA-2025-0005

Esfandian, H., & Rezazadeh. M. (2020). Modeling and Comparison of Optimized Isotherm Models for H2, N2, CO, CH4 and CO2 Adsorption Using Cuckoo Search Optimization Algorithm. *International Journal of Engineering*, *33*(5). https://doi.org/10.5829/ije.2020.33.05b.01

Fakher, S., & Imqam, A. (2020). A review of carbon dioxide adsorption to unconventional shale rocks methodology, measurement, and calculation. *SN Applied Sciences*, *2*(1), 5. https://doi.org/10.1007/s42452-019-1810-8

Feng, H., Wang, Z., Min, Z., Qiao, L., Guo, J., Liu, J., & Zhao, G. (2025). Fine 3D geological modeling method for underground gas storage and application in injection production optimization. *Gas Science and Engineering*, 205542. https://doi.org/10.1016/j.jgsce.2025.205542

Feng, Q., Li, R., Jia, Y., & Liang, Z. (2025). Big data and artificial intelligence-based optimization of petroleum exploration and reservoir modeling: Intelligent pathways for enhancing efficiency and accuracy. *Advances in Resources Research*, *5*(2), 477–495. https://doi.org/10.50908/arr.5.2_477

Feng, Y., Zhang, S., Ma, C., Liu, F., Mosleh, M. H., & Shin, H. (2023). The role of geomechanics for geological carbon storage. *Gondwana Research*, *124*, 100–123. https://doi.org/10.1016/j.gr.2023.07.003

Feng, Z., Feng, C., Zhong, Y., Qin, Z., Mao, R., Zhao, L., & Zong, X. (2022). TOC estimation of shale oil reservoir by combining nuclear magnetic resonance logging and nuclear physics logging. *Journal of Geophysics and Engineering*, *19*(4), 833–845. https://doi.org/10.1093/jge/gxac052

Fontaine, H., Rodziah, D., & Singh, U. (1990). Discovery of an Upper Triassic limestone basement in the Malay Basin, offshore Peninsular Malaysia: regional implications. *Journal of Southeast Asian Earth Sciences*, *4*(3), 219–232. https://doi.org/10.1016/S0743-9547(05)80015-7

Gaurina-Međimurec, N., & Novak Mavar, K. (2020). Carbon Capture and Storage (CCS): Geological Sequestration of CO_2. In *CO2 Sequestration*. IntechOpen. https://doi.org/10.5772/intechopen.84428

Gautam, Sah, R. P., & Sahoo, S. (2023). A review on adsorption isotherms and kinetics of CO2 and various adsorbent pairs suitable for carbon capture and green refrigeration applications. *Sādhanā*, *48*(1), 27. https://doi.org/10.1007/s12046-023-02080-9

Ghazali, Z., Suhaili, N., Tahari, M. N. A., Yarmo, M. A., Hassan, N. H., & Othaman, R. (2020). Impregnating deep eutectic solvent choline chloride:urea:polyethyleneimine onto mesoporous silica gel for carbon dioxide

capture. *Journal of Materials Research and Technology*, *9*(3), 3249–3260. https://doi.org/10.1016/j.jmrt.2020.01.073

Gheytanzadeh, M., Baghban, A., Habibzadeh, S., Esmaeili, A., Abida, O., Mohaddespour, A., & Munir, M. T. (2021). Towards estimation of CO2 adsorption on highly porous MOF-based adsorbents using gaussian process regression approach. *Scientific Reports*, *11*(1), 15710. https://doi.org/10.1038/s41598-021-95246-6

Gomaa, I., Guerrero, J., Heidari, Z., & Espinoza, D. N. (2022, September 26). Experimental Measurements and Molecular Simulation of Carbon Dioxide Adsorption on Carbon Surface. *SPE Annual Technical Conference and Exhibition*. https://doi.org/10.2118/210264-MS

Gonçalves, V. S. F., & De Carvalho, V. R. (2025). A Review of Interpretability Methods for Gradient Boosting Decision Trees. *Journal of the Brazilian Computer Society*, *31*(1), 640–654. https://doi.org/10.5753/jbcs.2025.5324

Gu, Y., Ding, W., Yin, S., Yin, M., & Xiao, Z. (2018). Adsorption characteristics of clay minerals in shale. *Petroleum Science and Technology*, *36*(2), 108–114. https://doi.org/10.1080/10916466.2017.1405031

Guang, W., Zhang, Z., Liu, X., He, X., Luo, P., & Lu, Y. (2025). Adsorption selectivity of confined CH4-CO2 mixture in coal: Influence of physicochemical structure and thermodynamic competitive mechanism. *Separation and Purification Technology*, *360*, 130982. https://doi.org/10.1016/j.seppur.2024.130982

Gunawardene, O. H. P., Gunathilake, C. A., Vikrant, K., & Amaraweera, S. M. (2022). Carbon Dioxide Capture through Physical and Chemical Adsorption Using Porous Carbon Materials: A Review. *Atmosphere*, *13*(3), 397. https://doi.org/10.3390/atmos13030397

Guo, J., Wang, C., Wang, Y., Zhang, W., Zhao, Q., Wei, H., & Nie, X. (2026). A shale-oil reservoir multi-mineral inversion method based on well-logging data using an improved random-forest approach: methodology and application. *Applied Computing and Geosciences*, *29*, 100334. https://doi.org/10.1016/j.acags.2026.100334

Haagsma, A., Fukai, I., Howat, E., Schuetter, J., Conner, A., Grove, B., Mishra, S., & Gupta, N. (2021). *Well Logging in Fractured Media* (pp. 27–68). https://doi.org/10.1007/978-3-030-62986-1_2

Hacıosmanoğlu, G. G., Mejías, C., Martín, J., Santos, J. L., Aparicio, I., & Alonso, E. (2022). Antibiotic adsorption by natural and modified clay minerals as designer adsorbents for wastewater treatment: A comprehensive review. *Journal of Environmental Management*, *317*, 115397. https://doi.org/10.1016/j.jenvman.2022.115397

Hamza, A., Hussein, I. A., Al-Marri, M. J., Mahmoud, M., & Shawabkeh, R. (2021). Impact of clays on CO2 adsorption and enhanced gas recovery in sandstone reservoirs. *International Journal of Greenhouse Gas Control*, *106*, 103286. https://doi.org/10.1016/j.ijggc.2021.103286

Hamza, A., Hussein, I. A., Al-Marri, M. J., Mahmoud, M., Shawabkeh, R., & Aparicio, S. (2021). CO2 enhanced gas recovery and sequestration in depleted gas reservoirs: A review. *Journal of Petroleum Science and Engineering*, *196*, 107685. https://doi.org/10.1016/j.petrol.2020.107685

Han, S., Sang, S., Zhang, J., Xiang, W., & Xu, A. (2023). Assessment of CO2 geological storage capacity based on adsorption isothermal experiments at various temperatures: A case study of No. 3 coal in the Qinshui Basin. *Petroleum*, *9*(2), 274–284. https://doi.org/10.1016/j.petlm.2022.04.001

Han, S., Wang, S., Guo, C., Sang, S., Xu, A., Gao, W., & Zhou, P. (2024). Distribution of the adsorbed density of supercritical CO2 onto the anthracite and its implication for CO2 geologic storage in deep coal. *Geoenergy Science and Engineering*, *234*, 212624. https://doi.org/10.1016/j.geoen.2023.212624

Han, S.-J., Sang, S.-X., Duan, P.-P., Zhang, J.-C., Xiang, W.-X., & Xu, A. (2022). The effect of the density difference between supercritical CO2 and supercritical CH4 on their adsorption capacities: An experimental study on anthracite in the Qinshui Basin. *Petroleum Science*, *19*(4), 1516–1526. https://doi.org/10.1016/j.petsci.2022.03.003

Hanif, H. R. (2024). The Role of Artificial Intelligence in Optimizing Oil Exploration and Production. *Eurasian Journal of Chemical, Medicinal and Petroleum Research*, *3*(5), 176–190. https://www.ejcmpr.com/article_210864.html

Hao, J., Wen, H., Ma, L., Fei, J., & Ren, L. (2021). Theoretical Derivation of a Prediction Model for CO_2 Adsorption by Coal. *ACS Omega*, *6*(20), 13275–13283. https://doi.org/10.1021/acsomega.1c00957

Harati, S., Rezaei Gomari, S., Ramegowda, M., & Pak, T. (2024). Multi-criteria site selection workflow for geological storage of hydrogen in depleted gas fields: A case for the UK. *International Journal of Hydrogen Energy*, *51*, 143–157. https://doi.org/10.1016/j.ijhydene.2023.10.345

Hazen, R. M., Downs, R. T., Morrison, S. M., Tutolo, B. M., Blake, D. F., Bristow, T. F., Chipera, S. J., McSween, H. Y., Ming, D., Morris, R. V., Rampe, E. B., Thorpe, M. T., Treiman, A. H., Tu, V. M., & Vaniman, D. T. (2023). On the Diversity and Formation Modes of Martian Minerals. *Journal of Geophysical Research: Planets*, *128*(9). https://doi.org/10.1029/2023JE007865

Hazen, R. M., & Morrison, S. M. (2022). On the paragenetic modes of minerals: A mineral evolution perspective. *American Mineralogist*, *107*(7), 1262–1287. https://doi.org/10.2138/am-2022-8099

He, M., Zhao, H., Yang, X., Jia, J., Liu, X., Qu, Z., Zhou, W., Sun, F., & Wang, Z. (2023). Reconsideration about the competitive adsorption of H2O and CO2 on carbon surfaces: The influence of oxygen functional groups. *Journal of Environmental Chemical Engineering*, *11*(6), 111288. https://doi.org/10.1016/j.jece.2023.111288

Hedenquist, J. W., & Arribas, A. (2022). Exploration Implications of Multiple Formation Environments of Advanced Argillic Minerals. *Economic Geology*, *117*(3), 609–643. https://doi.org/10.5382/econgeo.4880

Hou, L., Wu, S., Jing, Z., Jiang, X., Yu, Z., Hua, G., Su, L., Yu, C., Liao, F., & Tian, H. (2022). Effects of types and content of clay minerals on reservoir effectiveness for lacustrine organic matter rich shale. *Fuel*, *327*, 125043. https://doi.org/10.1016/j.fuel.2022.125043

Hu, K., Liu, X., Chen, Z., & Grasby, S. E. (2023). Mineralogical Characterization From Geophysical Well Logs Using a Machine Learning Approach: Case Study for the Horn River Basin, Canada. *Earth and Space Science*, *10*(12). https://doi.org/10.1029/2023EA003084

Hu, Q., & Zhang, Z. (2019). Application of Dubinin–Radushkevich isotherm model at the solid/solution interface: A theoretical analysis. *Journal of Molecular Liquids*, *277*, 646–648. https://doi.org/10.1016/j.molliq.2019.01.005

Hussain, M., Liu, S., Ashraf, U., Ali, M., Hussain, W., Ali, N., & Anees, A. (2022). Application of Machine Learning for Lithofacies Prediction and Cluster Analysis Approach to Identify Rock Type. *Energies*, *15*(12), 4501. https://doi.org/10.3390/en15124501

Hussain, W., Luo, M., Ali, M., Al-Khafaji, H. F., Hussain, I., Hussain, M., Ahmed, S. A. A., & Obaidullah. (2024). A Gamma-ray spectroscopy approach to evaluate clay mineral composition and depositional environment: A case study from the lower Goru Formation, Southern Indus Basin, Pakistan. *Journal of Applied Geophysics*, *226*, 105414. https://doi.org/10.1016/j.jappgeo.2024.105414

Hussein, H. S. (2023). Electrofacies Analysis using a Geostatistical Approach, Northern Iraq Case Study. *Polytechnic Journal*, *13*(2). https://doi.org/10.59341/2707-7799.1723

Iltaf, K. H., Yue, D., Wang, W., Wan, X., Li, S., Wu, S., Liu, R., Weijia, Z., Mehboob, S., Shah, S. A., Awan, R. S., & Tahir, M. (2021). Facies and Petrophysical Modeling of Triassic Chang 6 Tight Sandstone Reservoir, Heshui Oil Field, Ordos Basin, China. *Lithosphere*, *2021*(Special 1), 9230422. https://doi.org/10.2113/2021/9230422

Irannajad, M., Salmani Nuri, O., & Mehdilo, A. (2019). Surface dissolution-assisted mineral flotation: A review. *Journal of Environmental Chemical Engineering*, *7*(3), 103050. https://doi.org/10.1016/j.jece.2019.103050

Isah, A., Tariq, Z., Mustafa, A., Mahmoud, M., & Okoroafor, E. R. (2025). A Review of Data-Driven Machine Learning Applications in Reservoir Petrophysics. *Arabian Journal for Science and Engineering*. https://doi.org/10.1007/s13369-025-10329-0

Jacobs, A. (2021). *Carbon dioxide capture from flue gases using dry sorbents*. North-West University (South Africa).

Jia, J., Song, H., & Jia, P. (2024). Selective adsorption mechanism of CO2/CH4/N2 multi-component gas mixtures by N/S atoms and functional groups in coal. *Process Safety and Environmental Protection*, *182*, 210–221. https://doi.org/10.1016/j.psep.2023.11.079

Jiang, L., Cheng, L., Zhang, Y., Liu, G., & Sun, J. (2023). A Review on CO2 Sequestration via Mineralization of Coal Fly Ash. *Energies*, *16*(17), 6241. https://doi.org/10.3390/en16176241

Jin, B., Fu, D., Xiang, X., Zhao, H., Zhang, H., Mei, D., & Liang, Z. (2024). Integrated metal carbonate thermal decomposition with in-situ CO2 conversion: Review and perspective. *Gas Science and Engineering*, *129*, 205416. https://doi.org/10.1016/j.jgsce.2024.205416

Jin, H., Park, J. Y., Park, S. Y., Son, B.-K., Min, B., & Lee, K. (2024). Effect of preprocessing on performances of machine learning-based mineral composition analysis on gas hydrate sediments, Ulleung Basin, East Sea. *Petroleum Science*. https://doi.org/10.1016/j.petsci.2024.11.012

Kahal, A. Y., Barasain, A. O., & Abdelrahman, K. (2024). Evaluation of Alif Reservoir in Halewah oil field, Marib-Shabwa basin, Yemen, using seismic reflection data and petrophysical analysis. *All Earth*, *36*(1), 1–21. https://doi.org/10.1080/27669645.2024.2418238

Kazemifar, F. (2022). A review of technologies for carbon capture, sequestration, and utilization: Cost, capacity, and technology readiness. *Greenhouse Gases: Science and Technology*, *12*(1), 200–230. https://doi.org/10.1002/ghg.2131

Kearns, D., Liu, H., & Consoli, C. (2021). Technology readiness and costs of CCS. *Global CCS Institute*, *3*.

Khan, M. A., Amjad, M. R., Iltaf, K. H., Ahmed, A., & Awan, R. S. (2024). Structural inheritance through 3D reservoir modeling and ant-tracking attribute implications for structural configuration of Upper Cretaceous Pab Sandstone, Kirthar Fold Belt, Pakistan. *Journal of Natural Gas Geoscience*, *9*(2), 123–137. https://doi.org/10.1016/j.jnggs.2024.01.002

Khashman, M. A., & Shirazi, H. (2023). *3D Geological Modeling with Petrel Software: Estimating Original Oil in Place of Lower Cretaceous Y- Formation: A Case Study in a Selected Oilfield*. https://doi.org/10.21203/rs.3.rs-3345863/v1

Kim, D., Choi, J., Kim, D., & Byun, J. (2020). Predicting mineralogy by integrating core and well log data using a deep neural network. *Journal of Petroleum Science and Engineering*, *195*, 107838. https://doi.org/10.1016/j.petrol.2020.107838

Kim, K., Kim, D., Na, Y., Song, Y., & Wang, J. (2023). A review of carbon mineralization mechanism during geological CO2 storage. *Heliyon*, *9*(12), e23135. https://doi.org/10.1016/j.heliyon.2023.e23135

Kolomytsev, A., & Kalistratov, A. (2017, October 16). Formation Evaluation for Thin Bed Shaly Sand Reservoirs. *SPE Russian Petroleum Technology Conference*. https://doi.org/10.2118/187905-MS

Kumar, K. V., Gadipelli, S., Howard, C. A., Kwapinski, W., & Brett, D. J. L. (2021). Probing adsorbent heterogeneity using Toth isotherms. *Journal of Materials Chemistry A*, *9*(2), 944–962. https://doi.org/10.1039/D0TA08150G

Kumar, T., Seelam, N. K., & Rao, G. S. (2022). Lithology prediction from well log data using machine learning techniques: A case study from Talcher coalfield, Eastern India. *Journal of Applied Geophysics*, *199*, 104605. https://doi.org/10.1016/j.jappgeo.2022.104605

Kumari, P., Yahmadi, R., Mumtaz, F., Vega, L. F., Ceriani, A., Tribuzio, R., Dumée, L. F., & Decarlis, A. (2024). CO2 capture via subsurface mineralization geological settings and engineering perspectives towards long-term storage and decarbonization in the Middle East. *Carbon Capture Science & Technology*, *13*, 100293. https://doi.org/10.1016/j.ccst.2024.100293

Le, V. N., Nguyen, V. C., Nguyen, H. T., Tran, H. D., Tu, T. N., Kim, W.-S., & Kim, J. (2023). Facile synthesis of bimetallic MIL-100(Fe, Al) for enhancing CO2 Adsorption performance. *Microporous and Mesoporous Materials*, *360*, 112716. https://doi.org/10.1016/j.micromeso.2023.112716

Lei, H., Huang, W., Jiang, Q., & Luo, P. (2022). Genesis of clay minerals and its insight for the formation of limestone marl alterations in Middle Permian of the Sichuan Basin. *Journal of Petroleum Science and Engineering*, *218*, 111014. https://doi.org/10.1016/j.petrol.2022.111014

Leng, J., Bump, A., Hosseini, S. A., Meckel, T. A., Wang, Z., & Wang, H. (2024). A comprehensive review of efficient capacity estimation for large-scale CO2 geological storage. *Gas Science and Engineering*, *126*, 205339. https://doi.org/10.1016/j.jgsce.2024.205339

Li, C., Wang, D., & Kong, L. (2021). Application of Machine Learning Techniques in Mineral Classification for Scanning Electron Microscopy - Energy Dispersive X-Ray Spectroscopy (SEM-EDS) Images. *Journal of Petroleum Science and Engineering*, *200*, 108178. https://doi.org/10.1016/j.petrol.2020.108178

Li, H., Chen, S., & Tang, D. (2024). Coal pore size distribution and adsorption capacity controlled by the coalification in China. *International Journal of Hydrogen Energy*, *88*, 594–603. https://doi.org/10.1016/j.ijhydene.2024.09.224

Li, L., Si, J., Li, Z., Cheng, G., & Chen, J. (2023). Experimental Study on Influencing Factors and Thermal Effects of CO $_2$ Adsorption by Coal. *ACS Omega*, *8*(24), 21906–21913. https://doi.org/10.1021/acsomega.3c01693

Li, S., Wang, C., Guo, F., Liu, X., Han, S., & Gao, R. (2022). Effect of Bound Water Content on Secondary Compression of Three Marine Silty Clays. *Journal of Marine Science and Engineering*, *10*(2), 261. https://doi.org/10.3390/jmse10020261

Li, X., Tang, X., Shan, Y., Guo, S., Deng, E., & Lan, C. (2024). *Methane Adsorption Capacity of Complex Shales in the Longtan Formation in the Eastern Sichuan-Northern Guizhou Region, South China*. https://doi.org/10.2139/ssrn.4698482

Liang, L., Xiong, J., Liu, X., & Luo, D. (2016). An investigation into the thermodynamic characteristics of methane adsorption on different clay minerals. *Journal of Natural Gas Science and Engineering*, *33*, 1046–1055. https://doi.org/10.1016/j.jngse.2016.06.024

Lin, X., Liu, C., & Wang, Z. (2023). The influencing factors of gas adsorption behaviors in shale gas reservoirs. *Frontiers in Earth Science*, *10*. https://doi.org/10.3389/feart.2022.1021983

Liu, H., Sang, S., Liu, S., Wu, H., Lan, T., Xu, H., & Ren, B. (2019). Supercritical-CO $_2$ Adsorption Quantification and Modeling for a Deep Coalbed Methane Reservoir in the Southern Qinshui Basin, China. *ACS Omega*, *4*(7), 11685–11700. https://doi.org/10.1021/acsomega.9b00599

Liu, L., Ge, Z., Zhou, Z., Li, Z., & Deng, Q. (2024). Mineral composition, pore structure and mechanical properties of coal measure strata rocks: A case study of Pingdingshan Coalfield. *Science of The Total Environment*, *952*, 175944. https://doi.org/10.1016/j.scitotenv.2024.175944

Liu, P., Zhang, T., & Sun, S. (2019). A tutorial review of reactive transport modeling and risk assessment for geologic CO2 sequestration. *Computers & Geosciences*, *127*, 1–11. https://doi.org/10.1016/j.cageo.2019.02.007

Liu, X., Wang, M., Zhang, J., Wang, Y., Yang, J., & Cheng, J. (2025). Short-wave infrared spectroscopy studies on hydrothermal minerals for exploration of the Jiaoxi W deposit, Tibet, China. *Ore Geology Reviews*, *176*, 106397. https://doi.org/10.1016/j.oregeorev.2024.106397

Liu, Y., & Hou, J. (2020). Selective adsorption of CO2/CH4 mixture on clay-rich shale using molecular simulations. *Journal of CO2 Utilization*, *39*, 101143. https://doi.org/10.1016/j.jcou.2020.02.013

Long, Y., Chen, Y., Xu, C., Li, Z., Liu, Y., & Wang, H. (2023). The role of global installed wind energy in mitigating CO2 emission and temperature rising. *Journal of Cleaner Production*, *423*, 138778. https://doi.org/10.1016/j.jclepro.2023.138778

Luo, A., Li, Y., Chen, X., Zhu, Z., & Peng, Y. (2022). Review of CO2 sequestration mechanism in saline aquifers. *Natural Gas Industry B*, *9*(4), 383–393. https://doi.org/10.1016/j.ngib.2022.07.002

Luo, J., Sun, K., Sun, S., Ma, R., Cui, C., & Cui, H. (2024). Mg and Fe co-loaded biochar prepared by microwave-synergized K2FeO4 of marine biomass for efficient CO2 capture: Performance assessment and mechanism exploration. *Chemical Engineering Journal*, *500*, 157102. https://doi.org/10.1016/j.cej.2024.157102

Lyu, Q., Luo, S., Guan, Y., Fu, J., Niu, X., Xu, L., Feng, S., & Li, S. (2019). A new method of lithologic identification and distribution characteristics of fine - grained sediments: A case study in southwest of Ordos Basin, China. *Open Geosciences*, *11*(1), 17–28. https://doi.org/10.1515/geo-2019-0002

Mabuza, M., Premlall, K., & Daramola, M. O. (2022). Modelling and thermodynamic properties of pure CO2 and flue gas sorption data on South African coals using Langmuir, Freundlich, Temkin, and extended Langmuir isotherm models. *International Journal of Coal Science & Technology*, *9*(1), 45. https://doi.org/10.1007/s40789-022-00515-y

Madani, N., Maleki, M., & Parviainen, A. (2025). Enhancing Multivariate Geostatistical Simulation in Mine Tailings Using the Projection Pursuit Multivariate Transform and Coregionalization Analysis. *Mathematical Geosciences*. https://doi.org/10.1007/s11004-025-10207-3

Maerten, L., Legrand, X., Castagnac, C., Lefranc, M., Joonnekindt, J.-P., & Maerten, F. (2019). Fault-related fracture modeling in the complex tectonic environment of the Malay Basin, offshore Malaysia: An integrated 4D geomechanical approach. *Marine and Petroleum Geology*, *105*, 222–237. https://doi.org/10.1016/j.marpetgeo.2019.04.025

Mahdi, Z., & Farman, G. (2023). 3D Geological Model for Zubair Reservoir in Abu-Amood Oil Field. *Iraqi Geological Journal*, *56*(1B), 40–50. https://doi.org/10.46717/igj.56.1B.4ms-2023-2-12

Mahmud, N. L., & Sautter, B. (2022). Structural and palynomorph evidence for Early <scp>Palaeogene-Neogene</scp> conglomerate series in Peninsular Malaysia: Implication for basin development and tectonic history. *Geological Journal*, *57*(11), 4529–4549. https://doi.org/10.1002/gj.4556

Manshor, N. A., Amir Hassan, M. H., & Madon, M. (2022). Tidally-influenced fluvial channel systems from the Miocene Malay Basin, Malaysia: Evidence from core

facies and seismic geomorphological analyses. *Marine and Petroleum Geology*, *135*, 105384. https://doi.org/10.1016/j.marpetgeo.2021.105384

Mansor, M. Y., Rahman, A. H. A., Menier, D., & Pubellier, M. (2014). Structural evolution of Malay Basin, its link to Sunda Block tectonics. *Marine and Petroleum Geology*, *58*, 736–748. https://doi.org/10.1016/j.marpetgeo.2014.05.003

Mechnou, I., Meskini, S., Elqars, E., Ait El Had, M., & Hlaibi, M. (2024). Efficient CO2 capture using a novel Zn-doped activated carbon developed from agricultural liquid biomass: Adsorption study, mechanism and transition state. *Surfaces and Interfaces*, *52*, 104846. https://doi.org/10.1016/j.surfin.2024.104846

Medina-Rodriguez, B. X., Alvarado, V., Edgin, M., & Kaszuba, J. (2021). Unveiling stimulation fluid-driven alterations in shale pore architecture through combined interpretation of TD-NMR and multi-component gas adsorption. *Fuel*, *297*, 120744. https://doi.org/10.1016/j.fuel.2021.120744

Mohamed, H., Mabrouk, W. M., & Metwally, A. (2024). Delineation of the reservoir petrophysical parameters from well logs validated by the core samples case study Sitra field, Western Desert, Egypt. *Scientific Reports*, *14*(1), 26841. https://doi.org/10.1038/s41598-024-77371-0

Mohammad, N. K., Ghaemi, A., & Tahvildari, K. (2019). Hydroxide modified activated alumina as an adsorbent for CO2 adsorption: Experimental and modeling. *International Journal of Greenhouse Gas Control*, *88*, 24–37. https://doi.org/10.1016/j.ijggc.2019.05.029

Mohammed, A. K. A., & Dhaidan, M. K. (2023). Prediction of Well Logs Data and Estimation of Petrophysical Parameters of Mishrif Formation, Nasiriya Field, South of Iraq Using Artificial Neural Network (ANN). *Iraqi Journal of Science*, 253–268. https://doi.org/10.24996/ijs.2023.64.1.24

Mohammed, I., Yaseri, A., Al Shehri, D., & Mahmoud, M. (2024). Basalt mineral surface charge and the effect of mineralization on its colloidal stability: Implications of subsurface CO2 storage. *Fuel*, *356*, 129569. https://doi.org/10.1016/j.fuel.2023.129569

Morley, R. J., Hasan, S. S., Morley, H. P., Jais, J. H. M., Mansor, A., Aripin, M. R., Nordin, M. H., & Rohaizar, M. H. (2021). Sequence biostratigraphic framework for the Oligocene to Pliocene of Malaysia: High-frequency depositional cycles driven by polar glaciation. *Palaeogeography, Palaeoclimatology, Palaeoecology*, *561*, 110058. https://doi.org/https://doi.org/10.1016/j.palaeo.2020.110058

Mortezaei, K., Amirlatifi, A., Ghazanfari, E., & Vahedifard, F. (2021). Potential CO_2 leakage from geological storage sites: advances and challenges. *Environmental Geotechnics*, *8*(1), 3–27. https://doi.org/10.1680/jenge.18.00041

Mouallem, J., Fathy, A., Arif, M., & Mahmoud, M. (2023, March 7). CO2 Mineral Trapping Potential of Carbonates: A Numerical Investigation. *Middle East Oil, Gas and Geosciences Show*. https://doi.org/10.2118/213517-MS

Mukherjee, A., Okolie, J. A., Abdelrasoul, A., Niu, C., & Dalai, A. K. (2019). Review of post-combustion carbon dioxide capture technologies using activated carbon. *Journal of Environmental Sciences*, *83*, 46–63. https://doi.org/10.1016/j.jes.2019.03.014

Murugesu, M. P., Joewondo, N., & Prasad, M. (2023). Carbon storage capacity of shale formations: Mineral control on CO_2 adsorption. *International Journal of Greenhouse Gas Control*, *124*, 103833. https://doi.org/10.1016/j.ijggc.2023.103833

Nema, A., Kumar, A., & Warudkar, V. (2025). An in-depth critical review of different carbon capture techniques: Assessing their effectiveness and role in reducing climate change emissions. *Energy Conversion and Management*, *323*, 119244. https://doi.org/10.1016/j.enconman.2024.119244

Newell, P., & Ilgen, A. G. (2019). Overview of Geological Carbon Storage (GCS). In *Science of Carbon Storage in Deep Saline Formations* (pp. 1–13). Elsevier. https://doi.org/10.1016/B978-0-12-812752-0.00001-0

Niu, M., Yao, Y., Zi, M., Dong, P., & Chen, D. (2024). Clay mineral mediated dynamics of CO2 hydrate formation and dissociation: Experimental insights for carbon sequestration. *Energy*, *311*, 133375. https://doi.org/10.1016/j.energy.2024.133375

Noorpoor, A. R., & Nazari Kudahi, S. (2016). Analysis and study of CO 2 adsorption on UiO-66/graphene oxide composite using equilibrium modeling and ideal adsorption solution theory (IAST). *Journal of Environmental Chemical Engineering*, *4*(1), 1081–1091. https://doi.org/10.1016/j.jece.2016.01.017

Noreen, K., Azeem, T., Rehman, F., Amin, Y., Ahmad, Q. A., & Hussain, M. (2025). Analyzing the impact of clay minerals on the reservoir quality of the Lower Goru Formation using Unsupervised Machine Learning. *PLOS One*, *20*(5), e0324793. https://doi.org/10.1371/journal.pone.0324793

Nwali, O. I., Oladunjoye, M. A., & Alao, O. A. (2024). A review of atmospheric carbon dioxide sequestration pathways; processes and current status in Nigeria. *Carbon Capture Science & Technology*, *12*, 100208. https://doi.org/10.1016/j.ccst.2024.100208

Ogiesoba, O. C., & Palacios, F. C. (2024). Photoelectric Factor Characterization of a Mixed Carbonate and Siliciclastic System Using Machine-Learning Methods: Pennsylvanian Canyon and Strawn Reef Systems, Midland Basin, West Texas. *Geosciences*, *15*(1), 3. https://doi.org/10.3390/geosciences15010003

Paluszny, A., Graham, C. C., Daniels, K. A., Tsaparli, V., Xenias, D., Salimzadeh, S., Whitmarsh, L., Harrington, J. F., & Zimmerman, R. W. (2020). Caprock integrity and public perception studies of carbon storage in depleted hydrocarbon reservoirs. *International Journal of Greenhouse Gas Control*, *98*, 103057. https://doi.org/10.1016/j.ijggc.2020.103057

Park, S. Y., Son, B.-K., Choi, J., Jin, H., & Lee, K. (2022). Application of machine learning to quantification of mineral composition on gas hydrate-bearing sediments, Ulleung Basin, Korea. *Journal of Petroleum Science and Engineering*, *209*, 109840. https://doi.org/10.1016/j.petrol.2021.109840

Pavkov, T. M., Kabadzhov, V. G., Ivanov, I. K., & Ivanov, S. I. (2023). Local Convergence Analysis of a One Parameter Family of Simultaneous Methods with Applications to Real-World Problems. *Algorithms*, *16*(2), 103. https://doi.org/10.3390/a16020103

Pearce, J., Raza, S., Baublys, K., Hayes, P., Firouzi, M., & Rudolph, V. (2022). Unconventional CO2 Storage: CO2 Mineral Trapping Predicted in Characterized Shales, Sandstones, and Coal Seam Interburden. *SPE Journal*, *27*(05), 3218–3239. https://doi.org/10.2118/209791-PA

Pereira, P., Caeiro, M. H., Lopes, A. M., Santos, M., Silva, D. M. da, Revaux, C., & Carneiro, J. (2023). Learnings from 3D Facies Modelling for CO2 Geological Storage in the Offshore of Lusitanian Basin, Portugal. *Fifth EAGE Conference on Petroleum Geostatistics*, 1–5. https://doi.org/10.3997/2214-4609.202335079

Peretomode, E., Oluyemi, G., & Faisal, N. H. (2022). Oilfield chemical-formation interaction and the effects on petrophysical properties: a review. *Arabian Journal of Geosciences*, *15*(13), 1223. https://doi.org/10.1007/s12517-022-10469-9

Piccin, J. S., Cadaval, T. R. S., de Pinto, L. A. A., & Dotto, G. L. (2017). Adsorption Isotherms in Liquid Phase: Experimental, Modeling, and Interpretations. In *Adsorption Processes for Water Treatment and Purification* (pp. 19–51). Springer International Publishing. https://doi.org/10.1007/978-3-319-58136-1_2

Poonoosamy, J., Wanner, C., Alt Epping, P., Águila, J. F., Samper, J., Montenegro, L., Xie, M., Su, D., Mayer, K. U., Mäder, U., Van Loon, L. R., & Kosakowski, G. (2021). Benchmarking of reactive transport codes for 2D simulations with mineral dissolution–precipitation reactions and feedback on transport parameters. *Computational Geosciences*, *25*(4), 1337–1358. https://doi.org/10.1007/s10596-018-9793-x

Postma, T. J. W., Bandilla, K. W., Peters, C. A., & Celia, M. A. (2022). Field-Scale Modeling of CO_2 Mineral Trapping in Reactive Rocks: A Vertically Integrated Approach. *Water Resources Research*, *58*(1). https://doi.org/10.1029/2021WR030626

Pothana, P., Ifrene, G., & Ling, K. (2024). Integrated Petrophysical Evaluation and Rock Physics Modeling of Broom Creek Deep Saline Aquifer for Geological CO2 Storage. *Fuels*, *5*(1), 53–74. https://doi.org/10.3390/fuels5010004

Proietti, G., Cvetković, M., Saftić, B., Conti, A., Romano, V., & Bigi, S. (2022). 3D modelling and capacity estimation of potential targets for CO $_2$ storage in the Adriatic Sea, Italy. *Petroleum Geoscience*, *28*(1). https://doi.org/10.1144/petgeo2020-117

Punnam, P. R., Krishnamurthy, B., & Surasani, V. K. (2022). Investigation of solubility trapping mechanism during geologic CO2 sequestration in Deccan Volcanic Provinces, Saurashtra, Gujarat, India. *International Journal of Greenhouse Gas Control*, *120*, 103769. https://doi.org/10.1016/j.ijggc.2022.103769

Qiao, L., & Fu, D. (2025). N-doped carbon sphere-SiO2 composite structure materials with high adsorption rate and low regeneration energy consumption for CO2 capture from flue gas. *Journal of Environmental Chemical Engineering*, *13*(1), 115218. https://doi.org/10.1016/j.jece.2024.115218

Radulescu, M., Dalal, S., Lilhore, U. K., & Saimiya, S. (2024). Optimizing mineral identification for sustainable resource extraction through hybrid deep learning enabled FinTech model. *Resources Policy*, *89*, 104692. https://doi.org/10.1016/j.resourpol.2024.104692

Ragadhita, R., & Nandiyanto, A. B. D. (2021). How to Calculate Adsorption Isotherms of Particles Using Two-Parameter Monolayer Adsorption Models and Equations. *Indonesian Journal of Science and Technology*, *6*(1), 205–234. https://doi.org/10.17509/ijost.v6i1.32354

Rahimi, M., & Riahi, M. A. (2020). Static reservoir modeling using geostatistics method: a case study of the Sarvak Formation in an offshore oilfield. *Carbonates and Evaporites*, *35*(2), 62. https://doi.org/10.1007/s13146-020-00598-1

Rangel Gavidia, J. C., Furlan Chinelatto, G., Basso, M., da Ponte Souza, J. P., Soltanmohammadi, R., Campane Vidal, A., Goldstein, R. H., & Mohammadizadeh, S. (2023). Utilizing integrated artificial intelligence for characterizing mineralogy and facies in a pre-salt carbonate reservoir, Santos Basin, Brazil, using cores, wireline logs, and multi-mineral petrophysical evaluation. *Geoenergy Science and Engineering*, *231*, 212303. https://doi.org/10.1016/j.geoen.2023.212303

Rani, S., Prusty, B. K., Padmanabhan, E., & Pal, S. K. (2019). Applicability of various adsorption isotherm models on adsorption of methane and CO $_2$ on Indian shales. *Environmental Progress & Sustainable Energy*, *38*(6). https://doi.org/10.1002/ep.13222

Raza, A., Gholami, R., Rezaee, R., Bing, C. H., Nagarajan, R., & Hamid, M. A. (2017). Well selection in depleted oil and gas fields for a safe CO2 storage practice: A case

study from Malaysia. *Petroleum*, *3*(1), 167–177. https://doi.org/10.1016/j.petlm.2016.10.003

Ricci, S., Elgendy, A. M. S., Geloni, C., Ortenzi, A., Previde Massara, E., Consonni, A., Atena, R., Facchi, G. L. D., Idiomi, M., & Casali, P. (2021). Carbon Capture & Storage: Rock Experimental Characterization & Modelling Prospective. *SSRN Electronic Journal*. https://doi.org/10.2139/ssrn.3820928

Rider, M. H., & Kennedy, M. E. (2011). *The Geological Interpretation of Well Logs* (3rd ed.). Rider-French Consulting Ltd.

Romaine, G. (2020). *Rocks, Gems, and Minerals of the Rocky Mountains*. Rowman & Littlefield.

Saxena, A., Prakash Gupta, J., Tiwary, J. K., Kumar, A., Sharma, S., Pandey, G., Biswas, S., & Raghav Chaturvedi, K. (2024). Innovative Pathways in Carbon Capture: Advancements and Strategic Approaches for Effective Carbon Capture, Utilization, and Storage. *Sustainability*, *16*(22), 10132. https://doi.org/10.3390/su162210132

Schlumberger. (1989). *Log Interpretation Principles/Applications* (1989th ed.). Schlumberger Educational Services.

Schlumberger. (2009). *Log Interpretation Charts* (2009th ed.). Schlumberger.

Sen, S., Abioui, M., Ganguli, S. S., Elsheikh, A., Debnath, A., Benssaou, M., & Abdelhady, A. A. (2021). Petrophysical heterogeneity of the early Cretaceous Alamein dolomite reservoir from North Razzak oil field, Egypt integrating well logs, core measurements, and machine learning approach. *Fuel*, *306*, 121698. https://doi.org/10.1016/j.fuel.2021.121698

Serafin, J., & Dziejarski, B. (2023). Application of isotherms models and error functions in activated carbon CO2 sorption processes. *Microporous and Mesoporous Materials*, *354*, 112513. https://doi.org/10.1016/j.micromeso.2023.112513

Shahbazi, K., Zarei, A. H., Shahbazi, A., & Ayatizadeh Tanha, A. (2020). Investigation of production depletion rate effect on the near-wellbore stresses in the two Iranian southwest oilfields. *Petroleum Research*, *5*(4), 347–361. https://doi.org/10.1016/j.ptlrs.2020.07.002

Shams, M., Kausar, N., Araci, S., & Oros, G. I. (2024). Artificial hybrid neural network-based simultaneous scheme for solving nonlinear equations: Applications in engineering. *Alexandria Engineering Journal*, *108*, 292–305. https://doi.org/10.1016/j.aej.2024.07.078

Shen, W., Li, X., Ma, T., Cai, J., Lu, X., & Zhou, S. (2021). High-pressure methane adsorption behavior on deep shales: Experiments and modeling. *Physics of Fluids*, *33*(6). https://doi.org/10.1063/5.0054486

Shi, H., Li, J., Shen, H., Li, X., Wei, N., Wang, Y., Wang, Y., & Pan, H. (2024). Quantitative analysis of the numerical simulation uncertainties from geological models in CO2 geological storage: A case study of Shenhua CCS project. *International Journal of Greenhouse Gas Control*, *135*, 104142. https://doi.org/10.1016/j.ijggc.2024.104142

Shuvo, Md. A. I., & Joy, S. M. H. (2024). A data driven approach to assess the petrophysical parametric sensitivity for lithology identification based on ensemble learning. *Journal of Applied Geophysics*, *222*, 105330. https://doi.org/10.1016/j.jappgeo.2024.105330

Singh, N. B. (2022). Clays and Clay Minerals in the Construction Industry. *Minerals*, *12*(3), 301. https://doi.org/10.3390/min12030301

Sips, R. (1948). On the Structure of a Catalyst Surface. *The Journal of Chemical Physics*, *16*(5), 490–495. https://doi.org/10.1063/1.1746922

Song, X., Lü, X., Shen, Y., Guo, S., & Guan, Y. (2018). A modified supercritical Dubinin–Radushkevich model for the accurate estimation of high pressure methane adsorption on shales. *International Journal of Coal Geology*, *193*, 1–15. https://doi.org/10.1016/j.coal.2018.04.008

Song, Z., Yang, L., Jiang, F., Zhu, W., Li, X., Qi, Z., & Yin, Z. (2024). The mechanism of clay mineral transformation in CO2 geological storage and its impact on long-term storage potential. *Geoenergy Science and Engineering*, *242*, 213192. https://doi.org/10.1016/j.geoen.2024.213192

Sordi, R., Hartley, A., Saltapidas, S., & Watson, D. (2025). The Triassic Rift Event in the Northern North Sea, a New Tectonic Model for the Utsira High Area. *Basin Research*, *37*(4). https://doi.org/10.1111/bre.70055

Sordi, R., Saltapidas, S., Hartley, A., & Cooper, M. (2026). A quantitative assessment of tectonic stretching in the northern North Sea, the Triassic of the Utsira High and greater Tampen Spur area. *Journal of Structural Geology*, *202*, 105583. https://doi.org/10.1016/j.jsg.2025.105583

Stadtműller, M., & Jarzyna, J. A. (2023). Estimation of Petrophysical Parameters of Carbonates Based on Well Logs and Laboratory Measurements, a Review. *Energies*, *16*(10), 4215. https://doi.org/10.3390/en16104215

Sun, L., Liu, Y., Cheng, Z., Jiang, L., Lv, P., & Song, Y. (2023). Review on Multiscale CO $_2$ Mineralization and Geological Storage: Mechanisms, Characterization, Modeling, Applications and Perspectives. *Energy & Fuels*, *37*(19), 14512–14537. https://doi.org/10.1021/acs.energyfuels.3c01830

Sun, R., Xu, W., Wang, X., Wei, R., Long, H., & Lei, J. (2025). Experimental study and mechanism analysis on enhancing CO2 sequestration in steel slag by activating

silicate components with potassium modification. *Fuel*, *381*, 133534. https://doi.org/10.1016/j.fuel.2024.133534

Sun, Y., Li, S., Sun, R., Yang, S., & Liu, X. (2020). Modified Dubinin–Astakhov Model for the Accurate Estimation of Supercritical Methane Sorption on Shales. *ACS Omega*, *5*(26), 16189–16199. https://doi.org/10.1021/acsomega.0c01675

Sun, Z., Wu, G., Huang, B., Cheng, L., Luan, J., Zhang, R., Chen, Z., & Zeng, C. (2023). Surface-Molecule Interaction Strength on CO_2 Adsorption Capacity in Nanopores: Implications to Advance CO_2 Sequestration Performance. *Industrial & Engineering Chemistry Research*, *62*(46), 19995–20005. https://doi.org/10.1021/acs.iecr.3c03037

Tao, L., Huang, J., Dastan, D., Wang, T., Li, J., Yin, X., & Wang, Q. (2021). New insight into absorption characteristics of CO2 on the surface of calcite, dolomite, and magnesite. *Applied Surface Science*, *540*, 148320. https://doi.org/10.1016/j.apsusc.2020.148320

Teletzke, G. F., & Lu, P. (2013). Guidelines for Reservoir Modeling of Geologic CO2 Storage. *Energy Procedia*, *37*, 3936–3944. https://doi.org/10.1016/j.egypro.2013.06.292

Tian, H., Li, T., Zhang, T., & Xiao, X. (2016). Characterization of methane adsorption on overmature Lower Silurian–Upper Ordovician shales in Sichuan Basin, southwest China: Experimental results and geological implications. *International Journal of Coal Geology*, *156*, 36–49. https://doi.org/10.1016/j.coal.2016.01.013

Tibane, L. V., Pöllmann, H., Ndongani, F. L., Landman, B., & Altermann, W. (2021). Evaluation of the lithofacies, petrography, mineralogy, and geochemistry of the onshore Cretaceous Zululand Basin in South Africa for geological CO2 storage. *International Journal of Greenhouse Gas Control*, *109*, 103364. https://doi.org/10.1016/j.ijggc.2021.103364

Tjia, H. D. (2010). Growing evidence of active deformation in the Malay basin region. *Bulletin of the Geological Society of Malaysia*, *56*, 35–40. https://doi.org/10.7186/bgsm56201005

Underhill, J. R., & Richardson, N. (2022). Geological controls on petroleum plays and future opportunities in the North Sea Rift Super Basin. *AAPG Bulletin*, *106*(3), 573–631. https://doi.org/10.1306/07132120084

UZUN, F., AYSAL, N., GUILLONG, M., & ALLAZ, J. M. (2024). Mineral chemistry and geothermobarometry of metasedimentary rocks of Central Menderes Massif, Western Türkiye: Metamorphic evolution and source of metapelitic rocks. *Geochemistry*, *84*(4), 126199. https://doi.org/10.1016/j.chemer.2024.126199

Vitek, R., & Masini, J. C. (2023). Nonlinear regression for treating adsorption isotherm data to characterize new sorbents: Advantages over linearization demonstrated

with simulated and experimental data. *Heliyon*, *9*(4), e15128. https://doi.org/10.1016/j.heliyon.2023.e15128

Vo Thanh, H., Sugai, Y., Nguele, R., & Sasaki, K. (2019). Integrated workflow in 3D geological model construction for evaluation of CO2 storage capacity of a fractured basement reservoir in Cuu Long Basin, Vietnam. *International Journal of Greenhouse Gas Control*, *90*, 102826. https://doi.org/10.1016/j.ijggc.2019.102826

Vo Thanh, H., Sugai, Y., & Sasaki, K. (2020). Application of artificial neural network for predicting the performance of CO2 enhanced oil recovery and storage in residual oil zones. *Scientific Reports*, *10*(1), 18204. https://doi.org/10.1038/s41598-020-73931-2

Wang, H., Williams-Stroud, S., Crandall, D., & Chen, C. (2024). Machine learning and deep learning for mineralogy interpretation and CO2 saturation estimation in geological carbon Storage: A case study in the Illinois Basin. *Fuel*, *361*, 130586. https://doi.org/10.1016/j.fuel.2023.130586

Wang, J., Chen, Y., Yao, H., Li, H., & Wang, C. (2025). Study on directed modification mechanism of surface functional groups of anthracite by supercritical CO2 for improved adsorption. *Fuel*, *386*, 134196. https://doi.org/10.1016/j.fuel.2024.134196

Wang, J., Samara, H., & Jaeger, P. (2025). Impact of Adsorption on Geological Storage of CO2. *SSRN Electronic Journal*. https://doi.org/10.2139/ssrn.5069153

Wang, T., Tian, F., Deng, Z., & Hu, H. (2023). The Characteristic Development of Micropores in Deep Coal and Its Relationship with Adsorption Capacity on the Eastern Margin of the Ordos Basin, China. *Minerals*, *13*(3), 302. https://doi.org/10.3390/min13030302

Wang, Y., Vuik, C., & Hajibeygi, H. (2022). CO2 Storage in deep saline aquifers: impacts of fractures on hydrodynamic trapping. *International Journal of Greenhouse Gas Control*, *113*, 103552. https://doi.org/10.1016/j.ijggc.2021.103552

Wang, Z., Tang, X., Jing, T., Du, K., Zhao, W., Shan, Y., Guan, Z., & Li, Z. (2024). Comparison of mineral transformation in CO2 geological storage under CO2–water–sandstone and mudstone reactions. *Geoenergy Science and Engineering*, *242*, 213215. https://doi.org/10.1016/j.geoen.2024.213215

Warren, B. E. (2012). *X-Ray Diffraction*. Dover Publications. https://books.google.com.my/books?id=cA_EAgAAQBAJ

Wedler, C., & Span, R. (2021). Micropore Analysis of Biomass Chars by CO_2 Adsorption: Comparison of Different Analysis Methods. *Energy & Fuels*, *35*(10), 8799–8806. https://doi.org/10.1021/acs.energyfuels.1c00280

Weger, R. J., Baechle, G. T., Shen, S., & Eberli, G. P. (2024). Significance of Sonic Velocities in Limestones and Dolostones: A Comprehensive Study Revealing Limited Impact of Mineralogy. *Minerals*, *14*(5), 509. https://doi.org/10.3390/min14050509

Woelk, M., Nam, M., Häckel, B., & Spörrle, M. (2025). From Questionnaires to Heatmaps: Visual Classification and Interpretation of Quantitative Response Data Using Convolutional Neural Networks. *Applied Sciences*, *15*(19), 10642. https://doi.org/10.3390/app151910642

Woo, J., Lee, H. S., Ozyer, C., & Rhee, C. W. (2021). Effect of Lamination on Shale Reservoir Properties: Case Study of the Montney Formation, Canada. *Geofluids*, *2021*, 1–14. https://doi.org/10.1155/2021/8853639

Xie, W., Wang, M., & Wang, H. (2021). Adsorption Characteristics of CH_4 and CO_2 in Shale at High Pressure and Temperature. *ACS Omega*, *6*(28), 18527–18536. https://doi.org/10.1021/acsomega.1c02921

Xu, Y., Zhu, H., Mo, S., Mao, Y., Zhong, C., Huang, Y., Yuan, R., Zheng, M., Zhou, M., & Chang, G. (2024). Adsorption of 2,4,6-trinitrotoluene by indole-based porous organic polymer with suitable three-dimensional space size via physisorption and chemisorption. *Polymer*, *300*, 126993. https://doi.org/10.1016/j.polymer.2024.126993

Yahia, M., Szabó, I., Badawi, M., Radwan, A. A., Kiss, K., Leila, M., & Szabó, N. P. (2025). Integrated petrophysical and seal characterization of the heterogeneous jurassic plover formation for CO2 storage assessment in Northwest Australia. *Scientific Reports*, *15*(1), 35416. https://doi.org/10.1038/s41598-025-17135-6

Yan, P., Yue, X., Kou, X., Hu, G., Yin, Q., Chang, J., & Lai, F. (2021). Application of LithoScanner Logging Technology in CO_2 Geological Storage Injection Well. *IOP Conference Series: Earth and Environmental Science*, *781*(2), 022095. https://doi.org/10.1088/1755-1315/781/2/022095

Yang, K., Zhou, J., Xian, X., Zhang, C., Tian, S., Dong, Z., Fan, M., & Cai, J. (2021). Adsorption Characteristics and Thermodynamic Analysis of CH4 and CO2 on Continental and Marine Shale. *Transport in Porous Media*, *140*(3), 763–788. https://doi.org/10.1007/s11242-021-01599-x

Yang, X., Yin, H., Yang, L., Xu, L., Chen, J., Liu, D., Jiang, C., & Jiang, Z. (2024). Evolution of black shale sedimentary environment and its impact on organic matter content and mineral composition: a case study from Wufeng-Longmaxi Formation in Southern and Eastern Sichuan Basin. *Frontiers in Environmental Science*, *12*. https://doi.org/10.3389/fenvs.2024.1391445

Yang, X., Zhou, Y., Hu, J., Zheng, Q., Zhao, Y., Lv, G., & Liao, L. (2024). Clay minerals and clay-based materials for heavy metals pollution control. *Science of The Total Environment*, *954*, 176193. https://doi.org/10.1016/j.scitotenv.2024.176193

Yin, Y., Dong, X., Dai, L., Zhang, E., & Liu, Y. (2025). Hydroxyl and amino co-modified imidazole based ionic liquid functionalized TS-1 molecular sieve for efficient CO2 capture. *Separation and Purification Technology*, *358*, 130393. https://doi.org/10.1016/j.seppur.2024.130393

Yin, Y., Zhang, L., Cao, X., Li, Q., Gan, M., & Wang, Y. (2025). Progress, challenges, and prospects of CO2 mineral sequestration in basalt: A critical review. *Applied Energy*, *381*, 125127. https://doi.org/10.1016/j.apenergy.2024.125127

Zapata, Y., Kristensen, M. R., Huerta, N., Brown, C., Kabir, C. S., & Reza, Z. (2020). CO2 geological storage: Critical insights on plume dynamics and storage efficiency during long-term injection and post-injection periods. *Journal of Natural Gas Science and Engineering*, *83*, 103542. https://doi.org/10.1016/j.jngse.2020.103542

Zardari, Z. H., & Mohshim, D. F. (2025). Temperature Dependence Evaluation of CO2 Adsorption on Eagle Ford Shale using Isothermal Models: A Comparative Study. *Engineering, Technology & Applied Science Research*, *15*(1), 19959–19965. https://doi.org/https://doi.org/10.48084/etasr.9094

Zhang, P., Jia, Y., & Shang, Y. (2022). Research and application of XGBoost in imbalanced data. *International Journal of Distributed Sensor Networks*, *18*(6), 155013292211069. https://doi.org/10.1177/15501329221106935

Zhang, Q., Masoudi, M., Sun, L., Zhang, L., Yang, L., Song, Y., & Hassanpouryouzband, A. (2024). Hydrogen and Cushion Gas Adsorption–Desorption Dynamics on Clay Minerals. *ACS Applied Materials & Interfaces*, *16*(40), 53994–54006. https://doi.org/10.1021/acsami.4c12931

Zhang, Y., Li, D., Xin, G., Jiu, H., & Ren, S. (2024). Molecular Insights into CO_2 -Rich Industrial Waste Gas Enhanced Shale Gas Recovery and Sequestration in Real Shale Gas Reservoirs. *Energy & Fuels*, *38*(1), 285–313. https://doi.org/10.1021/acs.energyfuels.3c03821

Zhang, Y., Qu, X., Yuan, Y., Zhang, Y., & Li, Q. (2024). Mineral trapping of carbon dioxide: Rapid hydrothermal synthesis experiments and carbon sequestration potential of dawsonite. *Science of The Total Environment*, *946*, 174220. https://doi.org/10.1016/j.scitotenv.2024.174220

Zhang, Y., Zhu, X., Wang, J., Zhong, L., M.Othman, R., Lithoxoos, G. P., Shakhs, A. N., Almansour, F., Zeng, X., Sun, X., & Pan, W.-P. (2025). High-temperature ammonia treatment of zeolite-template carbon for enhanced CO2 adsorption: A study on diffusion behaviors and adsorption mechanisms. *Chemical Engineering Journal*, *505*, 159168. https://doi.org/10.1016/j.cej.2024.159168

Zhao, L., Mao, W., & Li, X. (2026). Depth-domain inversion with angle-domain PSF for quantitative reservoir characterization: A case study from the Northern Viking

Graben, North Sea. *Petroleum Science*. https://doi.org/10.1016/j.petsci.2026.03.038

Zhao, P., Wang, H., Wang, L., Xu, D., Ma, H., & Guo, H. (2022). Prediction of methane adsorption capacity in different rank coal at low temperature by the Polanyi-based isotherm model. *Energy Science & Engineering*, *10*(4), 1384–1397. https://doi.org/10.1002/ese3.1108

Zhong, Z., & Carr, T. R. (2019). Geostatistical 3D geological model construction to estimate the capacity of commercial scale injection and storage of CO2 in Jacksonburg-Stringtown oil field, West Virginia, USA. *International Journal of Greenhouse Gas Control*, *80*, 61–75. https://doi.org/10.1016/j.ijggc.2018.10.011

Zhou, J., Liu, M., Xian, X., Jiang, Y., Liu, Q., & Wang, X. (2019). Measurements and modelling of CH4 and CO2 adsorption behaviors on shales: Implication for CO2 enhanced shale gas recovery. *Fuel*, *251*, 293–306. https://doi.org/10.1016/j.fuel.2019.04.041

Zhou, S., Zhang, D., Wang, H., & Li, X. (2019). A modified BET equation to investigate supercritical methane adsorption mechanisms in shale. *Marine and Petroleum Geology*, *105*, 284–292. https://doi.org/10.1016/j.marpetgeo.2019.04.036

Zhu, L.-Q., Sun, J., Zhou, X.-Q., Li, Q.-P., Fan, Q., Wu, S.-L., & Wu, S.-G. (2023). Well logging evaluation of fine-grained hydrate-bearing sediment reservoirs: Considering the effect of clay content. *Petroleum Science*, *20*(2), 879–892. https://doi.org/10.1016/j.petsci.2022.09.018

APPENDICES

APPENDIX A

Algorithm Design for Machine Learning Development

Mineral Composition Estimation

```
1  import pandas as pd
2  import numpy as np
3  from scipy.optimize import minimize
4
5  def objective_function(x, rhob, nphi, dtc):
6      calculated_rhob = (1 - nphi)*(2.65 * x[0] + 2.71 * x[1] + 2.85 * x[2] + 2.41 * x[3] + 2.12 * x[4] + 2.52 * x[5] + 2.76 * x[6]) + 1 * nphi
7      calculated_nphi = (1 - nphi)*(-0.02 * x[0] - 0.01 * x[1] + 0.01 * x[2] + 0.37 * x[3] + 0.6 * x[4] + 0.3 * x[5] + 0.52 * x[6]) + 1 * nphi
8      calculated_dtc = (1 - nphi)*(56 * x[0] + 49 * x[1] + 44 * x[2] + 80 * x[3] + 120 * x[4] + 90 * x[5] + 80 * x[6]) + 189 * nphi
9      1 == x[0] + x[1] + x[2] + x[3] + x[4] + x[5] + x[6]
10     return (rhob - calculated_rhob)**2 + (nphi - calculated_nphi)**2 + (dtc - calculated_dtc)**2
11
12 def mineral_solver(rhob, nphi, dtc):
13     x0 = np.array([0.1, 0.1, 0.1, 0.1, 0.1, 0.1, 0.1])
14     constraints = (
15         {'type': 'eq', 'fun': lambda x: x[0] + x[1] + x[2] + x[3] + x[4] + x[5] + x[6] - 1},
16         {'type': 'ineq', 'fun': lambda x: x}
17     )
18     result = minimize(objective_function, x0, args=(rhob, nphi, dtc), constraints=constraints, bounds=[(0, 1)] * 7)
19     mineral_fractions = result.x
20     return mineral_fractions
21
22 # --- Main execution ---
23 file_path = r'C:\Users\muqri\Documents\Justi\Muqri Research\Python Project\Data\Asgard Well.xlsx'
24 df = pd.read_excel(file_path)
25
26 for index, row in df.iterrows():
27     rhob_value = row['RHOB']
28     nphi_value = row['NPHI']
29     dtc_value = row['DTC']
30
31     mineral_fractions = mineral_solver(rhob_value, nphi_value, dtc_value)
32
33     df.loc[index, ['Quartz_Calculated', 'Calcite_Calculated', 'Dolomite_Calculated', 'Kaolinite_Calculated', 'Montmorillonite_Calculated', 'Illite_Calculated', 'Chlorite_Calculated']] = mineral_fractions[:7]
34
35 # Calculate error
```

```
        calculated_rhob = (1 - nphi_value)*(2.65 * mineral_fractions[0] + 2.71 * mineral_fractions[1] + 2.85 * mineral_fractions[2] + 2.41 * mineral_fractions[3] + 2.12 * mineral_fractions[4] + 2.52 * mineral_fractions[5] + 2.76 * mineral_fractions[6]) + 1 * nphi_value
        calculated_nphi = (1 - nphi_value)*(-0.02 * mineral_fractions[0] - 0.01 * mineral_fractions[1] + 0.01 * mineral_fractions[2] + 0.37 * mineral_fractions[3] + 0.6 * mineral_fractions[4] + 0.3 * mineral_fractions[5] + 0.52 * mineral_fractions[6]) + 1 * nphi_value
        calculated_dtc = (1 - nphi_value)*(56 * mineral_fractions[0] + 49 * mineral_fractions[1] + 44 * mineral_fractions[2] + 80 * mineral_fractions[3] + 120 * mineral_fractions[4] + 90 * mineral_fractions[5] + 80 * mineral_fractions[6]) + 189 * nphi_value

        df.loc[index, 'RHOB Error (%)'] = abs((calculated_rhob - df.loc[index, 'RHOB']) / (df.loc[index, 'RHOB'] if df.loc[index, 'RHOB'] != 0 else 1) * 100)
        df.loc[index, 'NPHI Error (%)'] = abs((calculated_nphi - df.loc[index, 'NPHI']) / (df.loc[index, 'NPHI'] if df.loc[index, 'NPHI'] != 0 else 1) * 100)
        df.loc[index, 'DTC Error (%)'] = abs((calculated_dtc - df.loc[index, 'DTC']) / (df.loc[index, 'DTC'] if df.loc[index, 'DTC'] != 0 else 1) * 100)

output_dir = r'C:\Users\muqri\Documents\Justi\Muqri Research\Python Project\Results\Asgard Well Mineral Composition Result.xlsx'
df.to_excel(output_dir, index=False)
print(f"Results saved to: {output_dir}")
```

XGBoost Model Development

```
import pandas as pd
from sklearn.model_selection import train_test_split, GridSearchCV
from xgboost import XGBRegressor
from sklearn.multioutput import MultiOutputRegressor
from sklearn.metrics import mean_absolute_error, mean_squared_error, r2_score
import matplotlib.pyplot as plt
import numpy as np
import joblib
import os
import warnings
warnings.filterwarnings('ignore')

# Set output directory
output_dir = r'C:\Users\muqri\Documents\Justi\Muqri Research\Python Project\Results'
os.makedirs(output_dir, exist_ok=True)

# Load the dataset
file_path = r'C:\Users\muqri\Documents\Justi\Muqri Research\Python Project\Data\Train new Mineral Composition Result.xlsx'
df = pd.read_excel(file_path, engine='openpyxl')

# Select input features (X) and output targets (y)
X = df[['RHOB', 'NPHI', 'DTC']]
y = df[['Quartz', 'Calcite', 'Dolomite', 'Kaolinite', 'Montmorillonite', 'Illite', 'Chlorite']]

# Split data into training and testing sets
```

```
X_train, X_test, y_train, y_test = train_test_split(X, y, test_size=0.05, random_state=42)

# Initialize XGBRegressor with initial parameters (these will be tuned by GridSearchCV)
xgb_model = XGBRegressor(objective='reg:squarederror')

# Use MultiOutputRegressor to handle multiple target variables
multi_target_model = MultiOutputRegressor(xgb_model)

# Define the parameter grid for GridSearchCV
param_grid = {
    'estimator__n_estimators': [50, 100, 150],
    'estimator__learning_rate': [0.05, 0.1, 0.15],
    'estimator__max_depth': [3, 4, 5, 6]
}

# Initialize GridSearchCV
grid_search = GridSearchCV(
    estimator=multi_target_model,
    param_grid=param_grid,
    scoring='neg_mean_squared_error',
    cv=5,
    verbose=2
)

# Train the model using GridSearchCV
grid_search.fit(X_train, y_train)

# Get the best model and its hyperparameters
best_model = grid_search.best_estimator_
best_params = grid_search.best_params_
print(f"Best Hyperparameters: {best_params}")

# Make predictions using the best model
y_pred = best_model.predict(X_test)
y_pred_train = best_model.predict(X_train)

# Evaluate the model
target_variables = y.columns

# Store metrics for summary
metrics_summary = []

# Evaluate training set
print("\n--- Training Set Evaluation ---")
for target in target_variables:
    y_true_train = y_train[target]
    y_pred_mineral_train = y_pred_train[:, target_variables.get_loc(target)]
    mae_train = mean_absolute_error(y_true_train, y_pred_mineral_train)
```

```
    rmse_train = np.sqrt(mean_squared_error(y_true_train, y_pred_mineral_train))
    r2_train = r2_score(y_true_train, y_pred_mineral_train)

    metrics_summary.append({
        'Mineral': target,
        'Dataset': 'Training',
        'MAE': mae_train,
        'RMSE': rmse_train,
        'R2_Score': r2_train
    })
    print(f"{target}: MAE={mae_train:.4f}, RMSE={rmse_train:.4f}, R²={r2_train:.4f}")

# Evaluate testing set
print("\n--- Testing Set Evaluation ---")
for target in target_variables:
    y_true_test = y_test[target]
    y_pred_mineral_test = y_pred[:, target_variables.get_loc(target)]
    mae_test = mean_absolute_error(y_true_test, y_pred_mineral_test)
    rmse_test = np.sqrt(mean_squared_error(y_true_test, y_pred_mineral_test))
    r2_test = r2_score(y_true_test, y_pred_mineral_test)

    metrics_summary.append({
        'Mineral': target,
        'Dataset': 'Testing',
        'MAE': mae_test,
        'RMSE': rmse_test,
        'R2_Score': r2_test
    })
    print(f"{target}: MAE={mae_test:.4f}, RMSE={rmse_test:.4f}, R²={r2_test:.4f}")

# Create cross-plots for Training Set
print("\n--- Generating Cross-plots for Training Set ---")
for i, target in enumerate(target_variables):
    plt.figure(figsize=(8, 6))
    plt.scatter(y_train.iloc[:, i], y_pred_train[:, i], alpha=0.5, s=50, label='Predicted vs Actual')
    plt.plot(
        [y_train.iloc[:, i].min(), y_train.iloc[:, i].max()],
        [y_train.iloc[:, i].min(), y_train.iloc[:, i].max()],
        'r--', linewidth=2, label='Ideal'
    )

    r2_value_train = r2_score(y_train.iloc[:, i], y_pred_train[:, i])
    plt.text(0.05, 0.95, f"R² = {r2_value_train:.3f}", transform=plt.gca().transAxes,
fontsize=12, verticalalignment='top')

    plt.xlabel("Actual Values", fontsize=14)
    plt.ylabel("Predicted Values", fontsize=14)
    plt.tick_params(axis='both', which='major', labelsize=12)
```

```
    plt.title(f"{target} (Training Set)", fontsize=14, fontweight='bold')
    plt.legend(fontsize=10)
    plt.grid(True, alpha=0.3)
    plt.tight_layout()

    plot_path = os.path.join(output_dir, f'{target}_Training_Cross-plot.png')
    plt.savefig(plot_path, dpi=300, bbox_inches='tight')
    plt.close()
    print(f"✓ Saved: {target}_Training_Cross-plot.png")

# Create cross-plots for Testing Set
print("\n--- Generating Cross-plots for Testing Set ---")
for i, target in enumerate(target_variables):
    plt.figure(figsize=(8, 6))
    plt.scatter(y_test.iloc[:, i], y_pred[:, i], alpha=0.5, s=50, label='Predicted vs Actual')
    plt.plot(
        [y_test.iloc[:, i].min(), y_test.iloc[:, i].max()],
        [y_test.iloc[:, i].min(), y_test.iloc[:, i].max()],
        'r--', linewidth=2, label='Ideal'
    )

    r2_value_test = r2_score(y_test.iloc[:, i], y_pred[:, i])
    plt.text(0.05, 0.95, f"R² = {r2_value_test:.3f}", transform=plt.gca().transAxes, fontsize=12,
verticalalignment='top')

    plt.xlabel("Actual Values", fontsize=14)
    plt.ylabel("Predicted Values", fontsize=14)
    plt.tick_params(axis='both', which='major', labelsize=12)
    plt.title(f"{target} (Testing Set)", fontsize=14, fontweight='bold')
    plt.legend(fontsize=10)
    plt.grid(True, alpha=0.3)
    plt.tight_layout()

    plot_path = os.path.join(output_dir, f'{target}_Testing_Cross-plot.png')
    plt.savefig(plot_path, dpi=300, bbox_inches='tight')
    plt.close()
    print(f"✓ Saved: {target}_Testing_Cross-plot.png")

# Save prediction results
print("\n--- Saving Results ---")
results_df = X_test.reset_index(drop=True).copy()
results_df[[mineral + '_Actual' for mineral in target_variables]] =
y_test.reset_index(drop=True)
results_df[[mineral + '_Predicted' for mineral in target_variables]] = y_pred

# Normalize predicted values to sum to 100
predicted_cols = [mineral + '_Predicted' for mineral in target_variables]
results_df[predicted_cols] = results_df[predicted_cols].div(
    results_df[predicted_cols].sum(axis=1).replace(0, np.nan), axis=0
```

```
) * 100

output_predictions_path = os.path.join(output_dir, 'Prediction_Results.xlsx')
results_df.to_excel(output_predictions_path, index=False)
print(f"✓ Saved: Prediction_Results.xlsx")

# Save metrics summary
metrics_df = pd.DataFrame(metrics_summary)
output_metrics_path = os.path.join(output_dir, 'Metrics_Summary.xlsx')
metrics_df.to_excel(output_metrics_path, index=False)
print(f"✓ Saved: Metrics_Summary.xlsx")

print("\n" + "="*60)
print("METRICS SUMMARY")
print("="*60)
print(metrics_df.to_string(index=False))
print("="*60)

# Save the trained model
model_path = os.path.join(output_dir, 'xgb_multioutput_model.pkl')
joblib.dump(best_model, model_path)
print(f"\n✓ Model saved: xgb_multioutput_model.pkl")

print(f"\n{'='*60}")
print(f"✓ All results saved to: {output_dir}")
print(f"{'='*60}")
```

Blind Test and Interpretation

```
import os
import pandas as pd
import numpy as np
import matplotlib.pyplot as plt
import joblib
from sklearn.metrics import mean_squared_error, mean_absolute_error, r2_score


# --- Setup paths and output directory ---
output_dir = r'C:\Users\muqri\Documents\Justi\Muqri Research\Python Project\Results'
os.makedirs(output_dir, exist_ok=True)

model_path = os.path.join(output_dir, 'xgb_multioutput_model.pkl')
new_data_path = r'C:\Users\muqri\Documents\Justi\Muqri Research\Python Project\Data\X-1_X1 Mineral Composition Result.xlsx'
prediction_output_path = os.path.join(output_dir, 'X-1_X1_Prediction.xlsx')


# --- 1. Load trained model ---
```

```
best_model = joblib.load(model_path)

# --- 1.5 Set default font sizes for plots ---
plt.rcParams.update({
    'font.size': 12,
    'axes.titlesize': 16,
    'axes.labelsize': 14,
    'xtick.labelsize': 12,
    'ytick.labelsize': 12,
    'legend.fontsize': 12
})


# --- 2. Load new dataset ---
new_data = pd.read_excel(new_data_path, engine='openpyxl')

# Check required input columns
required_features = ['RHOB', 'NPHI', 'DTC']
for feat in required_features:
    if feat not in new_data.columns:
        raise ValueError(f"Required feature '{feat}' not found in new data.")


# --- 3. Predict ---
X_new = new_data[required_features]
predictions = best_model.predict(X_new)

mineral_names = ['Quartz', 'Calcite', 'Dolomite', 'Kaolinite', 'Montmorillonite', 'Illite', 'Chlorite']
pred_cols = [m + '_Predicted' for m in mineral_names]
pred_df = pd.DataFrame(predictions, columns=pred_cols)


# --- 4. Clean & normalize predictions to sum to 1 ---
# Set negatives to zero, then normalize each row so sums to 1. If sum==0 keep zeros.
pred_df = pred_df.clip(lower=0)
row_sums = pred_df.sum(axis=1)
zero_sum_mask = row_sums == 0
# divide to 1 (fractions)
pred_df.loc[~zero_sum_mask, :] = pred_df.loc[~zero_sum_mask, :].div(row_sums[~zero_sum_mask], axis=0)

# If due to numerical rounding the rows don't sum exactly to 1, distribute the small residual to the max mineral
residual = 1.0 - pred_df.sum(axis=1)
max_idx = pred_df.idxmax(axis=1)
for i, r in residual.items():
    if abs(r) > 1e-12:
        pred_df.at[i, max_idx[i]] += r
```

```
65
66
67  # --- 5. Concatenate and save predictions ---
68  results_df = pd.concat([new_data.reset_index(drop=True), pred_df.reset_index(drop=True)], axis=1)
69  results_df.to_excel(prediction_output_path, index=False, engine='openpyxl')
70  print(f"✓ Saved predictions: {prediction_output_path}")
71
72
73  # --- 6. Evaluate against calculated values if available ---
74  calc_cols = [m + '_Calculated' for m in mineral_names]
75  if not set(calc_cols).issubset(results_df.columns):
76      print("Calculated mineral columns not found in results; skipping metric calculations and plots.")
77  else:
78      metrics = []
79      # Compute metrics per mineral
80      for m in mineral_names:
81          y_true = results_df[m + '_Calculated']
82          y_pred = results_df[m + '_Predicted']
83
84          mse = mean_squared_error(y_true, y_pred)
85          rmse = np.sqrt(mse)
86          mae = mean_absolute_error(y_true, y_pred)
87          r2 = r2_score(y_true, y_pred)
88
89          metrics.append({'Mineral': m, 'Dataset': 'Blind Test', 'MAE': mae, 'RMSE': rmse, 'R2_Score': r2})
90          print(f"{m}: MAE={mae:.4f}, RMSE={rmse:.4f}, R²={r2:.4f}")
91
92      # Save metrics summary
93      metrics_df = pd.DataFrame(metrics)
94      metrics_path = os.path.join(output_dir, 'BlindTest_Metrics_Summary.xlsx')
95      metrics_df.to_excel(metrics_path, index=False)
96      print(f"✓ Saved metrics: {metrics_path}")
97
98      # Create and save cross-plots
99      for i, m in enumerate(mineral_names):
100         plt.figure(figsize=(6, 4))
101         plt.scatter(results_df[m + '_Calculated'], results_df[m + '_Predicted'], alpha=0.5, s=40)
102         mn = results_df[m + '_Calculated'].min()
103         mx = results_df[m + '_Calculated'].max()
104         plt.plot([mn, mx], [mn, mx], 'r--', linewidth=1.5)
105         r2v = r2_score(results_df[m + '_Calculated'], results_df[m + '_Predicted'])
106         plt.text(0.05, 0.95, f"R² = {r2v:.3f}", transform=plt.gca().transAxes, fontsize=14, verticalalignment='top')
107         plt.xlabel('Calculated Values', fontsize=14)
108         plt.ylabel('Predicted Values', fontsize=14)
109         plt.title(f'{m} (Blind Test)', fontsize=16)
110         plt.tick_params(axis='both', which='major', labelsize=12)
```

```
111         plt.grid(True, alpha=0.3)
112         plt.tight_layout()
113
114         plot_path = os.path.join(output_dir, f'{m}_BlindTest_Cross-plot.png')
115         plt.savefig(plot_path, dpi=300, bbox_inches='tight')
116         plt.close()
117         print(f"✓ Saved: {os.path.basename(plot_path)}")
118
119     print("\nAll blind-test results saved to:", output_dir)
```

AUTHOR'S PROFILE

Muqri Syahmi Anas received his Bachelor of Engineering (Hons.) in Oil and Gas Engineering from Universiti Teknologi MARA (UiTM), Shah Alam, Malaysia, in 2023. He subsequently pursued a Master of Science in Chemical Engineering, commencing in early 2024, at the same university. His research focuses on the application of machine learning techniques for mineral classification in geological formations and reservoir modelling. Currently, he is involved in several research projects, including the development and application of seismic inversion methods for reservoir characterization.

LIST OF PUBLICATIONS

Anas, M. S., Bakar, W. Z. W., Azizi, A., Sauki, A., Japperi, N. S., & Amir, Z. (2026). CO_2 Adsorption of Geological Formation Mineral: A Review. *Jurnal Kejuruteraan*, *38*(3), 1437–1448.